SCHOOL OF MECHANICAL,
INDUSTRIAL & AERONAUTICAL
ENGINEERING

Design of an Adaptive Dynamic Inversion-Based Neurocontroller for a Tandem-Controlled Agile Surface-to-Air Missile

MECN 8000A - MSc Dissertation

K.J. Phahlamohlaka
Student No: 550708

Supervisor: Prof. J.O. Pedro

A dissertation submitted to the Faculty of Engineering and the Built Environment, University of the Witwatersrand, Johannesburg, in fulfilment of the requirements for the degree of Master of Science in Engineering .

Johannesburg, April 2019

Declaration

I declare that this dissertation is my own, unaided work, except where otherwise acknowledged. It is being submitted for the degree of Master of Science in Engineering in the University of the Witwatersrand, Johannesburg. It has not been submitted before for any degree or examination at any other university.

Signed this 15th day of April 2019

Go seenywa sa mahlo aka Oratile Phahlamohlaka.

(To the apple of my eye Oratile Phahlamohlaka.)

Acknowledgements

I am grateful to my eternal cheerleader, my fiancée Ms. Zanele Khumalo for her continued support and patience during tough times and lonely hours she had to endure as I wrestled to complete my research. I would also like to express my greatest gratitude to my mentor and supervisor Prof. J.O. Pedro for providing me with the guidance and the necessary resources to make this research a success. To my manger and mentor Mr. Paulin Kantue, I would like to express my deepest thanks for giving me the time and support to complete my dissertation. My greatest thanks goes to my lifetime teacher and coach Mr. Robert Sepeke Tshukudi for his my lessons and guidance that cultivated in me a curious mind that has lead me to this path.

Ke rata go leboga Modimo Ramasedi-a-poloko, Mohlola legodimo le lefase. Ga e kaba ese yena tŝhohle ke lefela. Sa ma felelo ke leboga batswadi baka ba ba bilego lebone le mohlahli wa maoto aka go fihle ke eba monna.

Thanks for all your encouragement!

Abstract

Conventional plant-model dependent controller design approaches such as gain scheduling work well for simple flight envelope and airframe geometry. For complex flight envelope and airframe the approach results in a costly exercise to obtain a high-fidelity plant model. In this study an adaptive controller design approach is taken for an agile dual aerodynamically-controlled (DAC) missile autopilot. Adaptive controller approach does not require an exhaustive plant model and has the capability of accommodating plant uncertainty and unmodelled dynamics online. A direct model reference adaptive control (MRAC) is investigated with different adaptive rules for the DAC missile. A two time-scale separation dynamic inversion controller with proportional-integral controller was used as the baseline controller of the proposed MRAC controller. The two time-scale separation controller was benchmarked with a gain-scheduled three-loop autopilot. A radial basis function neural network (RBFNN) is used to approximate the unmatched uncertainty of the missile dynamics. Adaption of the uncertainties is done on the fast dynamics controller to ensure fast recovery. The uncertainty of the slow dynamics is handled with a proportional-integral (PI) controller. The following adaptive rules were used with the RBFNN: adaptive loop recovery (ALR), $\sigma-$ modification, $\epsilon-$ modification and optimal control modification (OCM). All the adaptive controllers exhibited better performance over the baseline controller, however the ALR and OCM stood-out in terms of transient performance and actuator deflection demands. A novel normalised optimal control modification rule with co-variance adjustment was also investigated. Normalisation eliminates effect of basis-function amplitudes on the adaption rate and co-variance adjustment eliminates the possibility of persistent learning by adjusting initial set high adaption gains to a lower value with time. The results indicated that normalisation and co-variance adjustment had no detrimental effect on the overall performance of the adaptive controller. It was further observed that the estimated uncertainty by RBFNN did not match the known unmodelled dynamics due to the fact that adaptive controller aims to minimise the tracking error between the reference model and plant irrespective of uncertainty estimation convergence. A homing loop was closed around the adaptive autopilot with a nine-state Kalman filter for target tracking and state estimation; and an augmented proportional navigation rule for collision course trajectory control. Performance envelope of the DAC missile with adaptive autopilot was investigated against a constant speed target, a weaving and constant manoeuvre target. The DAC missile controlled by the normalised OCM update rule with co-variance adjustment autopilot illustrated better performance over the baseline controller and a tail-fin controlled missile for all target engagement scenarios.

Submitted Papers

K.J. Phahlamohlaka and J.O Pedro. Application of Two Time-Scale Separation NDI Controller to a Dual Aerodynamically-Controlled Missile. *Submitted to the 12th IFAC Symposium on Dynamics and Control of Process Systems, including Bio-systems, (DYCOPS 2019)*

K.J Phahlamohlaka and J.O. Pedro. Normalised Optimal Control Modification with Co-variance Adjustment for Robust Adaptive Control of a DAC Missile. *Submitted to ISA Transactions (Ms. Ref. No.: ISATRANS-D-18-01092)*

Contents

List of Figures

List of Tables

List of Latin Symbols

The units of quantities defined by a symbol are indicated in square brackets following the description of the symbol. Quantities with no indicated units may be assumed to be dimensionless.

$\mathcal{L}_1-$ $1-$Norm [-].

$\mathcal{L}_2-$ $2-$Norm [-].

$\mathcal{L}$ Lagrangian [J].

$\mathcal{T}$ Kinetic energy [J].

$\mathcal{U}$ Potential energy [J].

$\vec{q}$ Generalised co-ordinates [-].

$\vec{\mathcal{Q}}$ Generalised forces [-].

A Axial force [N].

N Normal force [N].

S Side force [N].

L Rolling moment [Nm].

M Pitching moment [Nm].

n Yawing moment [Nm].

m Missile mass [kg].

$\vec{v}$ Velocity vector [m/s].

$\vec{G}$ Gravitational acceleration vector [m/s^2].

$\vec{R}_b$ Missile position vector in earth fixed frame [m].

u Body axial velocity [m/s].

v Body sway velocity [m/s].

w Body heave velocity [m/s].

p Body roll rate [rad/s].

q Body pitch rate [rad/s].

r Body yaw rate [rad/s].

$\bar{q}$ Dynamic pressure [pa].

I_{xx} Principle moment of inertia in the x-axis [kgm^2].

I_{yy} Principle moment of inertia in the y-axis [kgm^2].

I_{zz} Principle moment of inertia in the z-axis [kgm^2].

S_{ref} Cross-sectional area of the missile [m^2].

n_{struc} Maximum structural limit [g].

h Altitude [ft].

M Mach number [-].

V_m Air-speed [m/s].

d Missile diameter [m].

k_{p_z} Normal proportional gain [rad/(m/s^2)].

k_{p_y} Lateral proportional gain [rad/(m/s^2)].

k_{i_z} Lateral integral gain [rad/(m/s^2)].

k_{i_y} Lateral integral gain [rad/(m/s^2)].

B Control matrix [-].

A State matrix [-].

e_a Control tracking error vector [-].

e Reference model tracking error vector [-].

A_m Reference model state matrix [-].

W_0 Hidden layer bias weights [-].

W_x Hidden layer weights [-].

V_0 Output layer bias weight [-].

V Output layer weights [-].

W^* Ideal hidden layer weights [-].

W Estimated hidden layer weights [-].

P Positively defined symmetric matrix cost-to-go matrix [-].

Q Positively defined symmetric weighting matrix [-].

Γ_W Learning rate for hidden layer weights [-].

Γ_Θ Learning rate for output layer weights [-].

ν Optimal modification learning damping ratio [-].

R Normalisation weight matrix [-].

$\mathcal{V}$ Lyapunov candidate function [J].

$\vec{n}_{Mc}$ Proportional navigation missile acceleration command [m/s^2].

$\mathcal{N}$ Proportional navigation guidance gain [-].

$\vec{R}_{TM}$ Relative distance vector between the missile and the target [m].

$\vec{V}_{TM}$ Relative velocity between missile and target [m/s].

$\vec{n}_T$ Target acceleration [m/s^2].

$\boldsymbol{\hat{x}_f}$ Kalman filter estimated state vector [-].

$\boldsymbol{z_f^*}$ Kalman filter measurement vector [-].

$\boldsymbol{u_f}$ Kalman filter input vector [-].

A_f Kalman filter state matrix [-].

B_f Kalman filter control input matrix [-].

H_f Kalman filter measurement matrix [-].

$\boldsymbol{\mathcal{V}}$ Measurement noise vector [-].

$\boldsymbol{\mathcal{W}}$ White noise process vector [-].

$\boldsymbol{K_{fk}}$ Kalman filter gains [-].

$\boldsymbol{P}_{fk}$ Kalman filter co-variance matrix [-].

$\boldsymbol{R}_{fk}$ Kalman filter measurement noise matrix [-].

$\boldsymbol{Q}_{fk}$ Kalman filter discrete process noise matrix [-].

List of Greek Symbols

ϕ Body frame Euler yaw angle [rad].

θ Body frame Euler pitch angle [rad].

ψ Body frame Euler roll angle [rad].

$\bar{\omega}_b$ Body rate vector [rad/s].

α_{max} Maximum angle-of-attack [rad].

β_{max} Maximum angle-of-sideslip [rad].

α Angle-of-attack [rad].

β Angle-of-side slip [rad].

δ_q^c Canard pitch deflection [rad].

δ_q^t Tial-fin pitch deflection [rad].

δ_r^c Canard yaw deflection [rad].

δ_r^t Tail-fin yaw deflection [rad].

ζ_m Missile damping ratio [-].

τ_m Missile time constant [s].

ω_{cr} Open-loop crossover frequency [rad/s].

ω_q Pitch rate controller bandwidths [rad/s].

ω_r Yaw rate controller bandwidths [rad/s].

ω_p Roll rate controller bandwidths [rad/s].

ρ Air density [kg/m^3].

χ_d^t Desired attitude vector for tail-fin controller [rad/s].

χ_d^c Desired attitude vector for canard controller [rad/s].

ζ_d^t Desired wind angle vector for tail-fin controller [rad].

ζ_d^c Desired wind angle vector for canard controller [rad].

Φ Basis function of the neural network [-].

Θ^* Ideal output layer weights [-].

Θ Estimated output layer weights [-].

σ_W $\sigma-$mod learning damping ratio [-].

η Co-variance adjustment parameter.

List of Aerodynamic Coefficients

C_A Axial force coefficient [-].

C_S Side force coefficient [-].

C_N Normal force coefficient [-].

C_l Rolling moment aerodynamic coefficient [-].

C_m Pitching moment aerodynamic coefficient [-].

C_n Yawing moment aerodynamic coefficient [-].

C_{N_α} Normal-force first derivative in angle-of-attack [-].

$C_{N_{\alpha|\alpha|}}$ Normal-force second derivative in angle-of-attack [-].

$C_{N_{\alpha^3}}$ Normal-force third derivative [-].

$C_{N_{\alpha\beta^2}}$ Incremental normal force due to sideslip [-].

$C_{N_{\delta_q^c}}$ Canard lift effectiveness in pitch at constant angle of attack [-].

$C_{N_{\alpha\delta_q^c}}$ Variation of canard normal force effectiveness with angle of attack [-].

$C_{N_{\beta^2\delta_q^c}}$ Variation of canard normal force effectiveness with sideslip [-].

$C_{N_{\delta_q^t}}$ Loss of normal force due to canard and tail combined control action [-].

$C_{N_{\beta^2\delta_q^t}}$ Variation of tail lift effectiveness with sideslip [-].

$C_{N_{\delta_q^t\delta_q^c}}$ Incremental pitching moment,canard and tail combined action [-].

C_{N_q} Normal force due pitch dynamics [-].

$C_{N_{\dot\alpha}}$ Normal force variation with rate of change in angle-of-attack [-].

$C_{m_{\delta_q^t}}$ Pitching moment due to canard effect [-].

$C_{m_{\delta_q^t}}$ Pitching moment due to tail effect [-].

$C_{m_{\alpha}}$ Pitching moment coefficient first derivative [-].

$C_{m_{\alpha|\alpha|}}$ Pitching moment coefficient second derivative [-].

$C_{m_{\alpha^3}}$ Pitching moment coefficient third derivative [-].

$C_{m_{\alpha\beta^2}}$ Incremental pitching moment due to sideslip [-].

$C_{m_{\beta^2\delta_q^c}}$ Variation of canard pitch effectiveness with sideslip [-].

$C_{m_{\beta^2\delta_q^t}}$ Variation of tail pitch effectiveness with sideslip [-].

$C_{m_{\delta_q^c\delta_q^t}}$ Incremental pitching moment,canard and tail combined action [-].

C_{m_q} Pitching moment damping coefficient [-].

$C_{m_{\dot{\alpha}}}$ Pitching moment with rate of change in angle of attack [-].

C_{l_i} Induced rolling moment due to wind angles [-].

$C_{l_{\alpha\delta_r^c}}$ Induced rolling moment due to canard yaw [-].

$C_{l_{\alpha\delta_q^c}}$ Induced rolling moment due to canard pitch [-].

$C_{l_{\beta\delta_p}}$ Rolling moment due to roll deflection [-].

C_{l_p} Rolling moment damping effect [-].

C_{A_0} Form axial force coefficient of the missile [-].

$C_{A_{\alpha}}$ Axial force coefficient first derivative in angle-of-attack [-].

$C_{A_{\beta}}$ Increamental drag due to sideslip [].

$C_{A_{\alpha^2}}$ Axial force coefficient second derivative in angle-of-attack [-].

$C_{A_{\alpha^3}}$ Axial force coefficient third derivative in angle-of-attack [-].

$C_{A_{\delta_q^c}}$ Increamental axial force due to pitch canard deflection [-].

$C_{A_{\delta_r^c}}$ Increamental axial force due to yaw canard deflection [-].

$C_{A_{\delta_p}}$ Increamental axial force due to roll deflection [-].

$C_{A_{\delta_q^t}}$ Increamental axial force due to tail pitch deflection [-].

$C_{A_{\delta_r^t}}$ Increamental axial force due to tail yaw deflection [-].

List of Acronyms

6-DoF 6 degrees-of-freedom.

ALR Adaptive loop recovery.

cg Centre-of-gravity.

DAC Dual aerodynamically-controlled.

DF-MRAC Derivative free model reference adaptive control.

DI Dynamic inversion.

FOM Figure-of-merit.

IMU Inertial measurement unit.

LTI Linear-time-invariant.

MRAC Model reference adaptive control.

NASA National Aeronautics and Space Administration.

NDI Nolinear dynamic inversion.

NTCM NASA tandem-controlled missile.

OCM Optimal control modification.

PI Proportional-integral.

PN Propotional navigation.

SDRE State dependent Riccati equation.

STT Skid-to-turn.

UUB Uniformly ultimately bounded.

Chapter 1

Introduction

1.1 Background and Motivation

The requirement for an agile and super-manoeuvrable missile in the defence industry has been on the rise over the past three decades (Palumbo et al., 2010). Firstly, modern targets have grown significantly in terms of manoeuvrability, evasive tactics and countermeasures. Adding to these dynamic factors is the low visibility and high speeds associated with the targets (McFarland and Calise, 1997). These factors combined limit threat-detection, decision-making and action-taking period to an unworkable value.

Owing to these factors a need for a superior agile and super-manoeuvrable missile has been proven to exist. The need for high agility and manoeuvre superiority arises from proportional navigation rule that says the manoeuvrability of a missile should at least be three times that of the target it is intended to counter (Zarchan, 2012, Fleeman, 2006), for instance, for a missile to counter a threat that has 20g acceleration capability efficiently, the missile should have an acceleration capability of at least 60g to maintain a high kill rate. This requirement imposes extreme constraints on the airframe structural, aerodynamic and flight control design.

High agility and manoeuvrability ensure high missile kill rate, and to achieve a prescribed kill rate the flight control must ensure a short response time, the aerodynamics must ensure sufficient forces and moments to track the desired dynamics and the structure should be of high integrity to withstand the high manoeuvres and in overall guaranteeing short final miss distances. Short miss distances are highly favourable as they allow the warhead to be smaller hence reducing the overall weight of the missile and the fuel necessary to drive the missile to the specified Mach number (Fleeman, 2006). To achieve these tight specifications, revolutionary advancements in missile aerodynamics, control and guidance technology are necessary.

One improvement is to implement a dual-controlled missile to boost missile responsiveness. Two kinds of dual control implementation exist in the literature: use of side thrusters and tail-fins to enhance the missile responsiveness (Ridgely et al., 2006) and the use of tandem-control to augment the responsiveness of the missile (Ibarrondo and Sanz-Aránguez, 2016). Tandem-controlled missile has movable tail-fins and canards. In case of the side thrusters and tail-fins architecture; if the side thrusters are located after the centre-of-gravity (cg) towards the missile nose, the side thrusters cause a moment about the cg and if they are located before the cg they translate the missile cg in a heaving or swaying fashion (Kim et al., 2016). The side thrusters have a simple architecture and they are cheaper to install on a tail-fin controlled missile with relatively minimum effort and changes. However, they have a disadvantage that they provide actuation force once they are burnt out. Tandem control on the other hand has an additional complexity in that, extra mass is added with the canards and servos, however the control surfaces are usable through out the whole missile flight profile (Ibarrondo, 2015).

The improvements implemented on guidance and control to achieve radical advancements are to use nonlinear control, intelligent adaptive controller and integrated guidance and control schemes (Balakrishnan et al., 2012). Nonlinear control allows the designer to account for coupling between pitch-yaw and roll dynamics and in some cases, they provide a closed solution of the controller. Adaption is used to account for unmodelled/unknown dynamics of the missile such as the ones at high angles-of-attack which are difficult to obtain using experimental or computational techniques (McFarland and Calise, 1997). Integrated guidance and control on the other hand combines the design of the autopilot with that of the guidance algorithm (Menon and Ohlmeyer, 2001). By combining the two, some feedback loops are eliminated and thus reducing the response time of the missile (Cimen, 2008). Intelligent controllers offer a different approach to the control design in that they rely less on plant modelling and more on learning the dynamics of the plaint either online or offline (Balakrishnan et al., 2012). A common technique in the literature is to include some form of adaptive element in the control loop that produces an additional signal to a baseline controller to ensure that the plant follows desired dynamics in real time (Nguyen, 2018). In most intelligent adaptive controllers neural networks are the approximation technique of choice mainly because of their capability to approximate any function (Rajagopal et al., 2009).

To truly affirm that the proposed technology provides significant advantage in terms of time-delay, robustness, aerodynamic uncertainty compensation and guidance law robustness to ensure a small miss distance – it is necessary to combine existing technologies to leverage the advantages of each advancement in one system to obtain an augmented design. The current study aims to apply adaptive controller to a tandem-controlled missile which combines both the advantages of a tail-fin and canard-controlled missile.

1.2 Problem Statement

Agile missiles are required to perform complex manoeuvres quickly and precisely. An ability to achieve complex manoeuvres is fundamental to fast responding missile and ensures small turning radii. At this condition, however the aerodynamics are difficult to model, and any experimental data obtained at this flight condition poorly represents (and costs a fortune) the actual dynamics, hence real-time compensation by using intelligent adaptive control technique is necessary.

This study aims to answer the question: what is the best way to implement an adaptive control on a tandem-controlled missile to guarantee agility without the need for an exhaustive aerodynamic model. Furthermore, it aims to address some of the robustness challenges associated with adaptive control of agile systems. The combination of adaptive control and tandem-controlled missile further aims to address actuator insufficiency problem associated with either canard or tail-fin missile at certain flight conditions and missile attitudes.

1.3 Literature Review

1.3.1 Missile Aerodynamic Control

Traditionally, missile control involves use of four aerodynamic control surfaces, either movable canards or tail-fins. In most of the tail-fin controlled missile, it is a common practice to not have fixed canards in contrast to canard-controlled missiles that always have fixed tail-fins. Fixed tail-fins on a canard-controlled missile are required to provide lift and roll stability (Fleeman, 2006). Both tail-fin and canard-controlled architecture generate a moment about the missile cg causing a pitch or a yaw angular acceleration that result in a change in the angle-of-attack and angle-of-sideslip. However, tail-fin and canard-controlled missile differ on how the normal or lateral accelerations are induced. In the case of canard-control, deflections generate a lift force in the same direction as the main body lift (Ibarrondo, 2015). Consequently, canard-controlled airframes have a quick response time. Packaging of canard actuator is relatively easy unlike that of the tail-fin where there is a rocket motor to deal with (Gutman, 2003). Canards are capable of augmenting body lift at low angle-of-attack, but they are prone to stalling at high incidence angles; furthermore they tend to overshoot the guidance commands and the ramifications are degradation in settling time such that it negates the advantage of having canard control in the first place (Fleeman, 2006, Zarchan, 2012).

Tail-fins generate a lift force opposing the main body lift, thus initially creating an inverse response that amounts to a delay in the desired response. The inverse response of the tail-fin is characterised by an undershoot in body acceleration response (Snyder, 2009). As a consequence of the inverse response a tail-fin-controlled missile is characterised by a non-minimum phase acceleration response (Balakrishnan et al., 2012). Although the tail-fin requires complex package due to the presence of a rocket motor, the actuators required are small because of the low hinge moments induced on the fins (Fleeman, 2006). The non-minimum phase behaviour poses a serious challenge for tail-fin-controlled missile due to the inherent latency that is aggravated with altitude. Furthermore, the tail-fin is less effective at low angle-of-attack due to body downwash, and more effective at high angle-of-attack, where small deflections are required to achieve commanded state (Ibarrondo, 2015).

Canard and tail-fin control appear complementary in performance and optimal use of either is a function of flight condition. As such tandem-controlled missile combines tail-fin and canard control with the aim of exploiting the best features of each configuration at the suitable flight conditions. Mracek and Ridgely (2006) studied a DAC missile with an autopilot design using state dependent Riccati equation (SDRE) method and their results illustrated that tandem control eliminates the undershoot associated with tail-fin control, the overshoot inherent to canard control and also provided a faster response.

Figure 1.1 illustrates the tandem controlled missile at two actuation modes: dual-control and diverted mode (Mracek and Ridgely, 2005). The dual-control mode induces a yaw or pitch moment first to cause a heaving or swaying acceleration. This mode eliminates the undershoot associated with tail-fin control, the overshoot associated with canard control and has a fast response (Ibarrondo, 2015). Diverted mode induce pure heaving or swaying acceleration. A capability that both canard and tail-fin control lack. The diverted mode is necessary for head on intercept where slight quick correction are needed to reduce final miss distance.

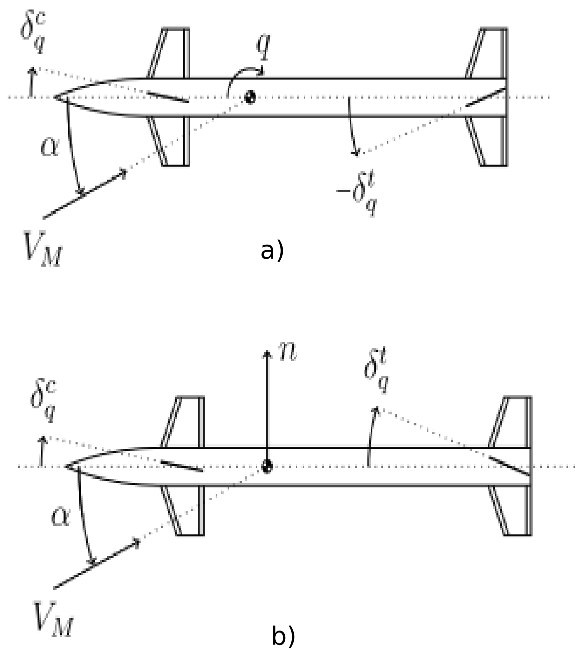

Figure 1.1: a) Dual actuation of canard and fins to induce a moment about the cg. b) Diverted mode of tandem-controlled missile to induce a translation force on the missile cg (Ibarrondo, 2015).

1.3.2 Linear Controller Design

Missile autopilot is traditionally designed based on linear techniques (Blakelock, 1991). The missile dynamics are linearised about an aerodynamic trim point to obtain a linear time invariant plant. To begin the autopilot design, coupling amongst the yaw, roll and pitch axis is neglected. Following from this assumption, controllers are designed separately for the yaw, pitch and roll axes (Fleeman, 2006). The decoupling approach limits the angle-of-attack to ensure that the response remains linear with minimum coupling effects. In the skid-to-turn (STT) configuration missile lateral, normal and roll commands to the autopilot are received from the guidance law to force the missile to track a desired trajectory (Balakrishnan et al., 2012). The controller gains are chosen using missile specifications and linear stability analysis (Kantue, 2017). Final controller parameters are tuned and selected based on the performance of the full nonlinear missile model. Aerodynamic behaviour of the missile varies with dynamic pressure, and to maintain performance and robustness throughout the entire flight envelope the linear control parameters are scheduled according to the trim-point they were designed at (Jackson, 2010). Controller parameters are scheduled with slow varying parameters such as altitude, dynamic pressure and Mach number (Balakrishnan et al., 2012).

Alternatives to the traditional approach is to use optimal control theory, H_∞ and other robust linear control techniques (Williams et al., 1987, Apkarian et al., 1995). The Laplace domain and robust linear approach are applied with gain scheduling and have proven their capability in countless applications on tail-controlled and canard-controlled missiles. A tandem-controlled missile however has two actuators that result in non-unique trim solution and a high number of trim points. Application of gain scheduling is possible but results in highly conservative controller that restrict the performance of the missile (Ibarrondo, 2015).

1.3.3 Nonlinear Controller Design

At close to intercept, traditional linear spectral separation might not be valid because of rapid changes in the relative geometry between the target and the missile (Levy et al., 2013). Several nonlinear-based alternatives to linear gain-scheduled controller have been researched extensively in the literature (Khalil, 1996, Vepa, 2016). Nonlinear controller design allows the designer to analytically develop a controller for a larger flight envelope without restoring to gain scheduling. Furthermore, the nonlinear design explicitly takes into account the nonlinear inherent to the missile mathematical model (Marquez, 2003). Nonlinear control design techniques can be grouped as follows: stability method controller (sliding mode controller (SMC)), linear-like methods (nonlinear dynamic inversion) and optimal techniques (SDRE) (ÇImen and Banks, 2004).

Ibarrondo (2015) studied application of SDRE controller to a tandem controlled missiles. SDRE controller showed promising results and was shown to be robust against extraneous effects such as seeker noise. The downside of SDRE controllers are that they are computational resource intensive (Balakrishnan et al., 2012, Cimen, 2012).

A method related to SDRE with a closed solution is $\theta-$D synthesis (Xin et al., 2004). $\theta-$D synthesis approach is formulated to find an approximate solution to Hamilton-Jacobi-Bellman (HJB) equation. There is no need to solve the online algebraic Riccati equation for $\theta-$D synthesis. The approximation is done by introducing an intermediate variable θ and co-states λ that can be expanded as powers of θ, thus reducing the HJB equation to a recursive algebraic equation (Balakrishnan et al., 2012).

Nonlinear dynamic inversion (NDI) cancels out the nonlinearities in the controlled plant using negative feedback and replaces them with the desired system dynamics (Balakrishnan et al., 2012). The desired system dynamics are defined with a reference model and only one such model is required for full flight envelope operation (Snell et al., 1992). One downside is that the performance of the NDI controller is dependent on the accuracy of the reference model. Furthermore, this technique is not directly applicable to non-minimum phase system. To get around this limitation in case of the tail-fin-controlled missile the pitch and yaw acceleration are used as commands instead of z-axis and y-axis acceleration commands (Balakrishnan et al., 2012). One major disadvantage is that dynamic inversion does not provide any theoretic guarantee of robustness for missiles (Jackson, 2010).

Sliding mode controller is a type of nonlinear robust controller that aims to maintain robustness of a controller in the presence of modelling errors for given uncertainty bounds (Huang et al., 2008). The controller offers closed-loop robustness and finite time controller convergence. Sliding mode control is done around a sliding surface denoted by $\sigma = 0$, where the sliding variable σ is a function of system tracking error (Azar and Serrano, 2015). SMC has an implicit plant inversion method and has difficulties with non-minimum phase plant such as tail-fin-controlled missile and it is addressed by introducing a dynamic sliding manifolds (Plestan et al., 2010). Sliding mode controller are currently the focus of both nonlinear and adaptive controller in missile guidance and control literature (Mobayen, 2015, Liu et al., 2014). The standard nonlinear techniques rely to some degree on plant model hence their performance in application is determined by the accuracy of the plant model (Balakrishnan et al., 2012).

1.3.4 Intelligent Controller Design

Intelligent control technique strives to be model independent by introducing intelligence in the control loop such that it is capable of re-configuring the controller to account for uncertainty in real-time (Yucelen and Haddad, 2013, Nguyen, 2018). Intelligent control achieves automation via emulation of biological intelligence (Li et al., 2016). The controllers borrow from how biological systems solve problems and apply them to control problems. In this survey, the review of intelligent controllers is limited to fuzzy logic, artificial neural networks and adaptive controllers.

1.3.4.1 Fuzzy Logic-Based Controller Design

Fuzzy logic control aims to implement intelligence of an operator and take advantage of knowledge base of how the system operates (Sampath et al., 2014). It is a heuristic approach that was historically developed to be model independent (Hunt et al., 1992). A general structure of a fuzzy logic controller consists of a fuzzification, an interface, knowledge base and defuzzification elements (Liu et al., 2016). Fuzzification transforms inputs to a form that can be interfaced with knowledge base. The interface is a reasoning machine which performs interface between the fuzzification and the knowledge base. Defuzzification converts conclusions of the interface mechanism into numerical control inputs to the plant (Lee, 1990).

Several augmented fuzzy controllers have been developed to overcome the deficiency of standard fuzzy logic controller such as fuzzy proportional-integral-derivative, fuzzy sliding mode controller, adaptive fuzzy controller and model-based fuzzy controller (Feng, 2006). Fuzzy logic controller requires extensive understanding of the control problem and plant dynamics (Liu et al., 2016). Furthermore the complexity of the controller grows exponentially with the number of inputs. In most aerospace applications, hybrid fuzzy controller is usually selected.

1.3.4.2 Neural Network-Based Controller Design

Artificial neural network-based (ANN) controllers are one of common intelligent control approaches found in flight control literature. Artificial neural network are inspired by the learning capability of the human brain (Feng, 2006). The difference between ANN and fuzzy logic is that ANN are able to learn from the model while fuzzy logic requires a knowledge base to be implementable (Hunt et al., 1992). The most common artificial neural network architecture is a feed-forward neural network. In most controllers, the ANN are used to perform model identification or model inversion (Kim and Calise, 1997). ANN inversion has an advantage over tradition NDI because of the learning, generalisation and nonlinear capability.

Early work by Slotine and Li (1987) demonstrated implementation of an ANN-based direct adaptive tracking control architecture. An inversion network was trained offline to encapsulate the nonlinearities of the known plant dynamics and an online learning architecture was developed to account for inversion errors. McFarland and Calise (2000) implemented a single hidden layer NN based augmented NDI controller for an anti-air missile.

Pedro et al. (2013) used an ANN-based NDI controller to maintain desired state of an unmanned aircraft during aerial refuelling. The RBFNN-based NDI was trained off-line and it demonstrated better performance over standard model inversion controller.

1.3.4.3 Hybrid Neuro-Fuzzy Controller Design.

Hybrid neuro-fuzzy controller aims to combine the advantages of both neural network and fuzzy logic based controllers (Li and Tong, 2003). The combination allows the controller to use both the heuristic knowledge and also learn from the plant during operation. Astrov et al. (2004) implemented a two-rate adaptive hybrid neuro-fuzzy controller for a missile autopilot. The controller topology consisted of a single layer ANN and two fuzzy logic controller for the inner and outer loops. Elhalwagy and Tarbouchi (2004) combined fuzzy logic and sliding mode controller for trajectory control of a guidance systems. The proposed hybrid controller alleviated chattering and the controller is independent of the number of system states.

1.3.5 Adaptive Controller Design

1.3.5.1 Robust Model Reference Adaptive Control

MRAC is a control technique that aims to drive the plant to follow known desired dynamics instead of requiring a nearly exhaustive model of the plant (Ioannou and Kokotovic, 1984). Unlike robust control that aims to tolerate plant uncertainty, adaptive control provides uncertainty accommodation through an adaptive feedback loop (Nguyen, 2018). Indirect and direct adaption are the two types of adaptive techniques common in MRAC control application (Calise and Rysdyk, 1998). Indirect adaption estimates control parameters and the estimates are used in the controller Barkana (2014). Direct adaption tunes the control signal to ensure adequate tracking of the reference model without estimating the control parameter (Sundararajan et al., 2003). Direct adaptive will be the focus of the current study. MRAC objective is to follow the desired dynamics in the presence of unknown nonlinearities, while maintaining the plant stability, performance and fast upset recovery (Calise and Rysdyk, 1998, Nguyen, 2018). Figure 1.2 illustrates the MRAC control block diagram. MRAC controller consists of a reference model, adaptive element, baseline controller and the uncertain plant. Reference model defines the desired dynamics to be followed by the plant. Baseline controller is designed using a low fidelity model of the uncertain plant. The adaptive element is the most critical component and it consists of the approximation algorithm and an update rule to estimate the weights of the approximation algorithm.

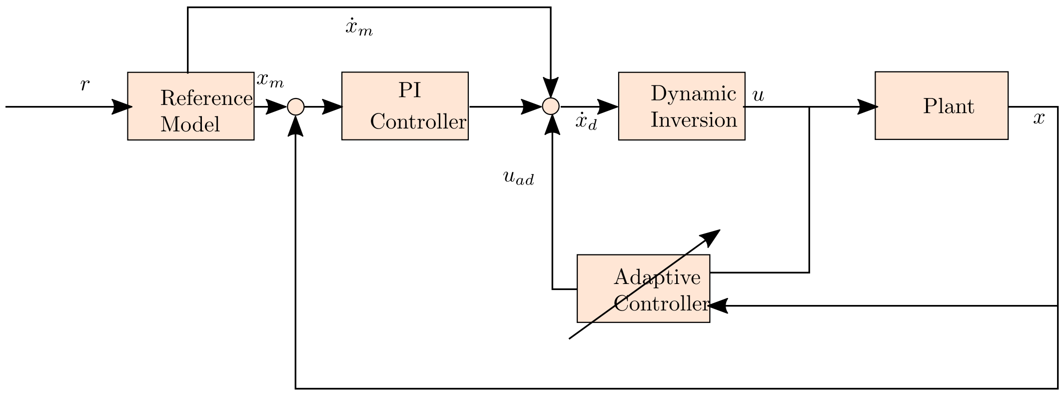

Figure 1.2: Typical architecture of MRAC controller scheme (Nguyen, 2009).

The update rule of the adaptive controller determines the stability and tracking performance of the system and most of the effort in the existing literature has focused on the robustness performance of the different update law. Recent prominent update rules are based on what is called the standard-MRAC update rule. Standard-MRAC update rule is derived using Lyapunov theory and guarantees asymptotic stability of the tracking error but has unbounded basis-function weights (Rajagopal et al., 2009). The major challenge concerning standard-MRAC is robustness in agile missile application. The agility requirement in the case of an adaptive controller translates to fast adaption of plant uncertainties to ensure desired tracking performance at all times (Padhi et al., 2007, Nguyen, 2012). However, the performance of standard MRAC degenerates with increasing adaption rates due to the unbounded weights. Overall as the adaption rates increase the tracking performance of standard MRAC improves but at the same time robustness against time delay and unmodelled dynamics suffers (Nguyen, 2012). Several techniques have been developed to address the unbounded weights issue at the expense of asymptotic stability of the tracking error in favour of uniformly ultimately bounded (UUB) tracking error and weights (Nguyen, 2018).

A technique that has been researched substantially is to introduce a learning damping ratio by adding a modification term to the MRAC update rule to guarantee UUB of tracking error and basis-function weights (Nguyen et al., 2008). Other successful technique such as the $\mathcal{L}_1-$adaptive controller introduce a filter on the adaptive signal (Hovakimyan and Cao, 2010). σ and $\epsilon-$modifications are two common and earlier robust adaptive rules in the literature that introduce a learning damper (Nguyen et al., 2011). $\sigma-$modification introduces a fixed damping ratio to the learning rate (Ioannou and Kokotovic, 1984) while $\epsilon-$modification introduces a tracking-error dependent learning damping ratio (Narendra and Annaswamy, 1987, Rohrs et al., 1985). Both σ and $\epsilon-$modifications ensure that the tracking error and the weights are bounded. $\epsilon-$modification further aims to recover the asymptotic stability property of MRAC at close to zero tracking error (Nguyen, 2018). Several recent robust update rules with modification terms are: optimal control modification (OCM) (Nguyen et al., 2008), adaptive loop recovery (ALR) (Calise et al., 2009), Q-modification and K-modification (Kim et al., 2010).

Optimal control modification was introduced in (Nguyen et al., 2008). The approach achieves robust adaption with large gains without incurring high-frequency adaptive signal by minimising $\mathcal{L}_2-$norm of the tracking error. Overall effect of OCM controller design technique is to introduce a damping factor to the weight update rule to reduce high-frequency oscillations (Nguyen, 2012, Nguyen et al., 2008). OCM minimises the $\mathcal{L}_2-$norm tracking error bound and imposes a limit on the modification damping term within which the system is guaranteed to remain bounded (Nguyen et al., 2008). The damping value is dependent on the persistent excitation condition, as such the weights are exponentially stable and bounded (Nguyen, 2009). The effectiveness of OCM adaptive controller was demonstrated by National Aeronautics and Space Administration (NASA) flight test program on a NASA F-18 aircraft between November 2010 and January 2011 Nguyen et al. (2017). ALR aims to recover the asymptotic tracking error property of standard MRAC while preserving the stability margins of the reference model (Calise and Yucelen, 2012). Preservation of the reference model margins in ALR is achieved by minimising nonlinearities in the closed-loop dynamics (Calise et al., 2009).

$\kappa-$ modification is a type of composite adaptive technique that adds learning stiffness to the update rule (Kim et al., 2010). When combined with $\sigma-$ or $\epsilon-$ modification update law, an update law with prescribed natural frequency and damping ratio in the error transient dynamics can be achieved. The modification term in the update rule filter out the high-frequency content while preserving the asymptotic stability of error dynamics (Nguyen, 2018).

$\mathcal{L}_1-$adaptive controller is robust adaptive controller proposed by (Cao and Hovakimyan, 2006). $\mathcal{L}_1-$adaption guarantees stability margin, robustness and tracking performance bounds in both transient and steady state (Cao and Hovakimyan, 2007b,a). The controller introduces a low pass filter to eliminate the high-frequency oscillation at fast adaption inherent to standard MRAC by introducing a low-pass filter. The bandwidth of the filter defines the trade-off between robustness and performance of the controller (Nguyen, 2018). High bandwidth increases tracking performance of the reference model but reduces the time delay margin (Hovakimyan and Cao, 2010).

Derivative free model reference adaptive control (DF-MRAC) is based on the premise of relaxing the assumption of existence of constant ideal weights that describe the system uncertainty (Yucelen, 2012). By relaxing the traditional assumption in MRAC, DF-MRAC can handle system with varying ideal weight. DF-MRAC improves adaption gain without the need for a modification term which is common to derivative-based MRAC. The relaxation of tradition assumption allows the update law to handle time varying weights and allow for possibility of discontinuous weights. Yucelen and Calise (2014) demonstrated that DF-MRAC robustness against unmodelled dynamics improves with increasing adaption gain by including a bias term in the adaption base function.

The effect of unbounded weights has been the focus when it comes to phenomenon that result in instability during high adaptive gains. Although explicit account to avoid unbounded weights effect is common in MRAC application, it is not the only source of instability that may result. High basis-function amplitudes can cause unstable high adaptive rates if not accounted for (Nguyen et al., 2011). Other effect is what is called persistent learning that results from maintaining high adaption gains even though the desired tracking performances have been achieved (Nguyen et al., 2017). Persistent learning at worse reduce the controller robustness. High basis-function amplitude are accounted for by normalising the update rule with the basis function and co-variance adjustment technique is used to prevent persistent learning by allowing large initial adaptive gains that are adjusted towards a lower value to improve robustness, retain desired tracking performance and robustness (Nguyen, 2018)

1.4 Identified Gaps in Literature

The following gaps were identified in the existing literature:

- Although multiple studies on applications of nonlinear control and adaptive control for agile missile exist, in most cases the missile considered is a generic tail-fin-controlled missile with little attention given to tandem-controlled missile or canard-controlled.
- Most of the studies focus on the robustness and performance of the technique on the longitudinal dynamics of the missile with little attention given to the whole 6 degrees-of-freedom (6-DoF) model.
- Little focus is given also on the combined behaviour of adaptive autopilot and guidance law.

- An overview system orientated study on how the adaptive autopilot behaves when countering highly manoeuvrable target that might stretch the dynamics of the missile out of the envelope are scarce.

1.5 Research Question

The main research question of the current study is: what is the best way to implement an MRAC controller to eliminate the high frequency oscillations associated with high adaption rates while maintaining specified robustness and performance, when applied to a tandem-controlled missile?

1.5.1 Research Objectives

Objectives of the current research are as follows:

- To develop a full nonlinear mathematical model for tandem-controlled missile.
- To design a nonlinear dynamic inversion controller for tandem-controlled missile to be used as reference model.
- To design an MRAC controller using OCM, adaptive loop recovery, $\sigma-$ modification update rule and compare the performance with baseline controller and standard MRAC.
- To evaluate the impact of normalisation and co-variance adjustment on update rule performance.
- To study the performance of the controller and guidance under engagement simulation and compare their performance.

1.6 Research Methodology, Scope and Limitation

1.6.1 Research Scope

The scope of of the current study is defined in Figure 1.3. The focus of the research entails unmodelled dynamics and missile uncertainty for different adaptive controller architectures.

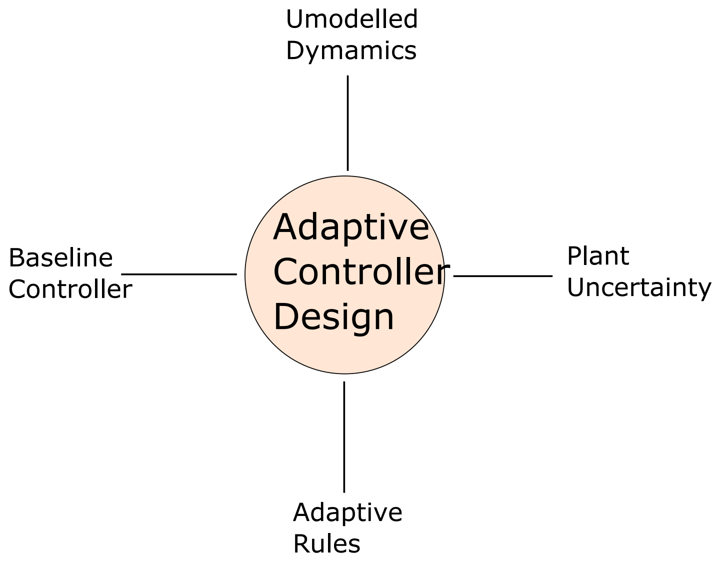

Figure 1.3: Scope of study.

1.6.2 Research Methodology

A simulation approach has been taken in the current study to evaluated the presented research question. Figure 1.4 illustrates the sequential task that define the methodology carried out in the current study to meet the defined objectives.

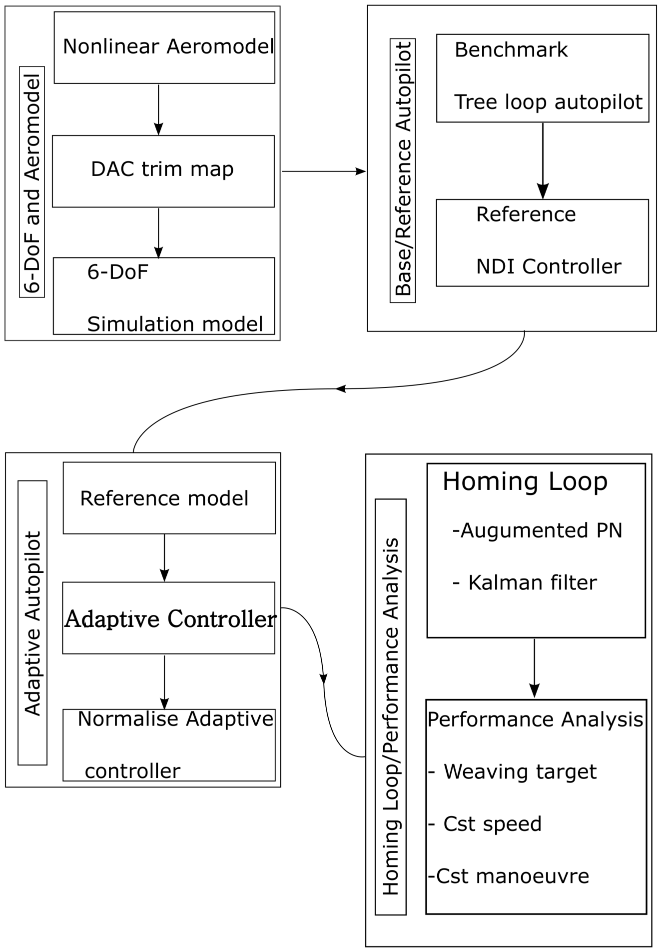

Figure 1.4: Methodology followed in the current study.

1.6.3 Limitations of the Study

The following assumptions were made on the aerodynamics, guidance and control; target dynamics and seeker performance:

- The aerodynamic model used in this study is restricted to supersonic flight and small sideslip angles of below 9 degrees.
- Full-state feedback is assumed throughout for all missile states.
- The tail-fin are assumed to always have enough deflection magnitude for roll, yaw and pitch controls.
- An infinite bandwidth was assumed for both tail-fin and canard actuators.

- The seeker is assumed to have a wide field of view and the up-link from the tracking-radar to the missile has no latency.
- The target is assumed to be a point mass with 100% radar reflectively.

1.7 Contributions to Knowledge

The major contributions of this dissertation are:

- A two time-scale separation nonlinear dynamic inversion controller is presented in the current study for a dual aerodynamically-controlled missile. The NDI controller is bench-marked with a gain-scheduled three-loop autopilot.
- A model reference adaptive controller architecture is presented for the DAC missile. A comparative study of the following adaptive controller is presented for canard, tail-fin and DAC missile: adaptive loop recovery, optimal control modification, $\sigma-$modification and $\epsilon-$modification. A RBFNN was used to account for modelling uncertainties.
- A novel normalised optimal control modification adaptive rule with co-variance adjustment is proposed. A Lyapunov proof is presented detailing the uniformly ultimately bounded stability condition of the adaptive controller.
- Homing loop of the missile with augmented proportional navigation is presented. A time varying Kalman filter is used to estimate the target kinematics. Comparison of engagement performance against a weaving, constant speed and constant manoeuvre target is detailed for both baseline controller and adaptive controller missiles.

1.8 Dissertation Outline

- **Chapter** 2 details the missile rigid-body dynamics, aerodynamics model, structural and geometrical properties. It further details the high-level assumption that are made in the whole dissertation. A detailed aerodynamic model of the DAC missile is presented. A trim map of the DAC missile is discussed together with the open-loop responses of the longitudinal dynamics for different actuation modes.
- **Chapter** 3 presents a gain-scheduled three-loop autopilot as a benchmark controller for the NDI controller which serves as the foundation for the baseline controller presented in chapter 4. A two time-scale separation NDI controller is designed for the

DAC missile. The two time-scale separation controller is compared with the three-loop autopilot to establish if it is sufficient to meet the desired performance.

- **Chapter** 4 presents the design of the MRAC controller for a DAC missile. A baseline controller based on the work from chapter 3 is used for all adaptive controllers presented. A comparison study of the following adaptive controller is conducted in this chapter: $\sigma-$ modification, $\epsilon-$ modification, ALR and OCM. An addition adaptive rule is proposed which combined normalised OCM and co-variance adjustment with an aim of eliminating effect of large basis-function amplitudes on the adaption rate and to prevent the possibility of persistent learning. A stability proof based on Lyapunov theory is presented for the normalised OCM with co-variance adjustment to prove that the UUB condition is met.

- **Chapter** 5 details the homing loop of the missile. A guidance loop is integrated with the autopilot to evaluate the performance of the missile against a weaving and a manoeuvring target. Augmented propotional navigation (PN) with a guidance gain $\mathcal{N} = 4$ is used throughout. Noise is introduced in the model through an active radar seeker. A linear Kalman filter is used to filter the target measurement noise and to estimate the target kinematic states. A target engagement comparison study of missile with adaptive autopilot and baseline is conducted.

- **Chapter** 6 presents the kinematic performance of the DAC missile against a manoeuvring, weaving and a constant speed target. Cruise performance envelope of a DAC and tail-fin missile are presented for different controller configuration: An adaptive (normalised OCM with co-variance adjustment) and baseline two time-scale separation.

- **Chapter** 7 presents the concluding remarks of the current study. Future work recommendations are detailed in this chapter.

Chapter 2

Missile Modelling and Dynamics

In this chapter, the aerodynamic model of a DAC missile and the nonlinear missile dynamic model are presented to lay foundation for flight controller modelling. The aerodynamic model is presented as proposed by (Ibarrondo, 2015). DAC missile used here is based on a scaled NASA tandem-controlled missile (NTCM). The following points define the high-level missile configuration used in this study:

- The missile has a cruciform configuration with both movable canards and tail-fins.
- The study considers only cruise (burned-out) supersonic guided flight between Mach 1.5 and 3.0.
- A rigid missile is assumed with ideal cruciform symmetry for both geometrical and inertial properties.
- During flight the missile is roll stabilised about the ″+″ configuration. This follows from the observation that ″X″ configuration results in severe canard tail-fin interference (Ibarrondo, 2015).
- A north, east, down co-ordinates system convention is used throughout.

2.1 Rigid Body Dynamic Equations of Motion

The dynamics of an aerospace vehicle are typically represented and modelled using rigid-body equations of motion. The rigid-body assumption is not far-fetched since the vibration dynamics have minimal effect on the overall design of flight control. In this section, the derivation of rigid-body dynamics is presented from first principles using Lagrangian approach. To simplify the derivation, translation and attitude dynamics are derived separately. Equation (2.1) is Lagrange's equation in vector form (Goldstein et al., 2001):

$$\frac{d}{dt}\left(\frac{\partial \mathcal{L}}{\partial \dot{\vec{q}}}\right) - \frac{\partial \mathcal{L}}{\partial \vec{q}} = \vec{\mathcal{Q}} \tag{2.1}$$

where $\mathcal{L}$ is the Lagrangian, defined as the difference between kinetic $\mathcal{T}$ and potential $\mathcal{U}$ energies of the system,

$$\mathcal{L} = \mathcal{T} - \mathcal{U}$$

$\vec{q}$ represents generalised co-ordinates and $\vec{\mathcal{Q}}$ represents the generalised forces respectively. In current case the generalised forces represent extraneous load due to aerodynamic loads : axial A, normal (N) and side (S) forces; and rolling (L), pitching (M) and yawing (n) moments.

2.1.1 Translation Dynamics

The derivation of missile translation dynamics from first principle using Lagrange's generalised equation of motion is detailed in this section.

Equation (2.2) defines the translation Lagrangian:

$$\mathcal{L}_{trans} = \frac{1}{2} m\vec{v} \cdot \vec{v} - m\vec{G} \cdot \vec{R}_b \tag{2.2}$$

where m is the missile mass, $\vec{v}$ is the velocity vector, $\vec{G}$ is the gravitational acceleration vector and $\vec{R}_b$ is the position vector in the body-fixed frame. The generalised co-ordinates are chosen to be the Earth-fixed reference co-ordinate system:

$$\vec{q}_{trans} = \begin{bmatrix} x_e & y_e & z_e \end{bmatrix}^T$$

Equation (2.3) defines a position vector of a body-fixed reference with respect to an Earth-fixed frame:

$$\vec{R}_b = \begin{bmatrix} \cos\theta\cos\psi & \cos\psi\sin\phi\sin\theta - \sin\psi\cos\phi & \cos\psi\cos\phi\sin\theta + \sin\phi\sin\psi \\ \cos\theta\sin\psi & \sin\psi\sin\phi\sin\theta - \cos\phi\cos\psi & \sin\psi\cos\phi\sin\theta - \sin\phi\cos\psi \\ -\sin\theta & \sin\phi\cos\theta & \cos\phi\cos\theta \end{bmatrix}^T \vec{R}_e \tag{2.3}$$

where $\vec{R}_e$ is the missile position vector in the Earth-fixed frame, angles ϕ (yaw), θ (pitch) and ψ (roll) represent the Euler angles between the body-fixed and Earth-fixed frames.

The velocity vector $\vec{v}$ is defined as follows in the body-fixed frame:

$$\vec{v} = \begin{bmatrix} u & v & w \end{bmatrix}^T \tag{2.4}$$

where u is the body axial velocity, v is the body sway velocity and w is the body heave velocity. The vector $\vec{G}$ is the gravitational acceleration vector which is always pointing down:

$$\vec{G} = \begin{bmatrix} 0 & 0 & g \end{bmatrix}^T \tag{2.5}$$

Substituting the translation Lagrangian (Eq. (2.2)) into the generalised equation of motion (Eq. (2.1)) and taking the derivative yields the first term of equation (2.1) for translation Lagrangian (Eq. (2.2)) as follows :

$$\frac{d}{dt}\left(\frac{\partial \mathcal{L}_{trans}}{\partial \vec{v}}\right) = m\left(\begin{bmatrix} \dot{u} \\ \dot{v} \\ \dot{w} \end{bmatrix} + \vec{\omega}_b \times \vec{v}\right) \tag{2.6}$$

where $\vec{\omega}_b$ is the angular body rate vector about body axis:

$$\bar{\omega}_b = \begin{bmatrix} p \\ q \\ r \end{bmatrix}$$

where p is the body roll rate, q is the body pitch rate and r is the body yaw rate defined with respect to the body axis.

The second term in the velocity derivative expression follows from vector calculus: given a vector $\vec{R}$ the time derivative is given by (Goldstein et al., 2001):

$$\frac{d}{dt}\begin{bmatrix} r_1(t) & r_2(t) & r_3(t) \end{bmatrix}^T = \begin{bmatrix} \dot{r}_1(t) & \dot{r}_2(t) & \dot{r}_3(t) \end{bmatrix}^T + \vec{\omega} \times \vec{r} \tag{2.7}$$

The second term of equation (2.1) for translation Lagrangian (Eq. (2.2)) is given by:

$$\frac{\partial \mathcal{L}}{\partial \vec{R}_e} = mg \begin{bmatrix} -\sin\theta \\ \sin\phi\cos\theta \\ \cos\phi\cos\theta \end{bmatrix} \tag{2.8}$$

The simplified translation equations of motion are given as follows:

$$m(\dot{u} + qw - rv) + mg\sin\theta = A \tag{2.9a}$$

$$m(\dot{v} + ru - pw) - mg\sin\phi\cos\theta = S \tag{2.9b}$$

$$m(\dot{w} + pv - qu) - mg\cos\phi\cos\theta = Z \tag{2.9c}$$

where A is the axial force, S is the side force and Z is the normal force. The external force due to aerodynamics are presented as functions of dynamic pressure $\bar{q}$; and aerodynamics axial force C_A , side force C_S and normal force C_N coefficients (see section 2.2 for more details).

$$\begin{bmatrix} A \\ S \\ Z \end{bmatrix} = \bar{q}S_{ref} \begin{bmatrix} C_A \\ C_S \\ C_N \end{bmatrix}$$

The thrust force is zero throughout the study because only the burned-out phase of the terminal phase is considered in this study.

2.1.2 Attitude Dynamics

This section presents the derivation of attitude dynamics for a missile using Lagrangian approach with the moment-of-inertia along the principal body axis system. Equation (2.10) depicts the Lagrangian for a rotating rigid body:

$$\mathcal{L}_{rot} = \frac{1}{2}\vec{\omega}_b{}^T \bar{I}_b \vec{\omega}_b - m\vec{G} \cdot \vec{R}_b \tag{2.10}$$

$\bar{I}_b$ is the moment-of-inertia tensor about the missile body axis. Entries $I_{xy} = I_{xz} = I_{yz} = 0$ about the principal axis for a missile with cruciform symmetry.

$$\bar{I}_b = \begin{bmatrix} I_{xx} & I_{xy} & I_{xz} \\ I_{xy} & I_{yy} & I_{yz} \\ I_{xz} & I_{yz} & I_{zz} \end{bmatrix} \tag{2.11}$$

where I_{xx}, I_{yy} and I_{zz} are the principal moment of inertia in the x, y and z-axes. The generalised rotational co-ordinates are defined by Euler angles:

$$\vec{q} = \begin{bmatrix} \phi & \theta & \psi \end{bmatrix}^T \tag{2.12}$$

where ϕ is the roll angle, θ is the pitch angle and ψ is the yaw angle.

Equation (2.13) defines the body rates in terms of Euler angle rates. The definition complements the initial choice of calculating moment-of-inertia about principal body axis.

$$\bar{\omega_b} = \begin{bmatrix} p \\ q \\ r \end{bmatrix} = \begin{bmatrix} 0 \\ 0 \\ 1 \end{bmatrix} \dot{\psi} + \begin{bmatrix} \cos\psi \\ -\sin\psi \\ 0 \end{bmatrix} \dot{\theta} + \begin{bmatrix} \sin\theta\sin\psi \\ \sin\theta\cos\psi \\ \cos\theta \end{bmatrix} \dot{\phi} \tag{2.13}$$

where $\bar{\omega_b}$ is the body rate vector.

The nature of Euler angle transformation allows for only one of the associated rotation axis to lie along one of the body axis, hence only one rotational equation of motion can be determined and the remaining two rotational equation of motion along the body axis must be obtained using cyclic permutation of the body axis (Goldstein et al., 2001). Cyclic permutation is a permutation which shifts all elements of a set by a fixed offset, with the elements shifted off the end inserted back at the beginning (Vialar, 2015) For the current derivation as presented ψ rotation is along the $z-$body axis, hence substituting the Lagrangian of the attitude motion (Eq. (2.10)) into the generalised equation of motion (Eq. (2.1)) yields the first term as:

$$\frac{d}{dt}\left(\frac{\partial \mathcal{L}_{rot}}{\partial \dot{\psi}}\right) = I_{zz}\dot{r} \tag{2.14}$$

The second term of the generalised attitude equation of motion with respect to ψ is given by:

$$\frac{\partial \mathcal{L}}{\partial \psi} = I_{xx}pq - I_{yy}qp \tag{2.15}$$

It can be easily shown that the partial derivative of the angular rate vector with respect to ψ is given by:

$$\frac{d\vec{\omega}_b}{d\psi} = \begin{bmatrix} q & -p & 0 \end{bmatrix}^T \tag{2.16}$$

Invoking cyclic permutation on the set $\{\phi, \theta, \psi\}$ yields the following attitude equations:

$$I_{zz}\dot{r} - (I_{xx} - I_{yy})pq = n \tag{2.17a}$$

$$I_{yy}\dot{q} - (I_{zz} - I_{xx})pr = M \tag{2.17b}$$

$$I_{xx}\dot{p} - (I_{yy} - I_{zz})qr = L \tag{2.17c}$$

The generalised torques about each body axis are defined by the following vector. L is the rolling moment, M is the pitching moment and n is the yawing moment. The aerodynamic moments are presented as a function of dynamic pressure and aerodynamic coefficient (see section 2.2 for details).

$$\begin{bmatrix} L \\ M \\ n \end{bmatrix} = \bar{q} S_{ref} d \begin{bmatrix} C_l \\ C_m + \bar{s} C_N \\ C_n - \bar{s} C_S \end{bmatrix} \tag{2.18}$$

where C_l is the rolling moment coefficient, C_m is the pitching moment coefficient, C_n is the yawing moment coefficient and $\bar{q}$ is the dynamic pressure, d is the missile diameter and S_{ref} is the cross-sectional area of the missile.

2.2 Airframe and Aerodynamic Model

This section details the DAC missile aerodynamic model and the mechanical properties of the missile. The aerodynamic model is presented in correlation form in the wind axis.

2.2.1 Airframe Mechanical Properties

Table 2.1 illustrates high-level geometrical, inertial and mechanical properties of the DAC missile. Only the necessary properties for the current study are presented in Table 2.1. A detailed presentation of the missile properties is given in (Ibarrondo, 2015).

The missile is considered to have a structural limit of 60g, a direct consequence of the requirement that the missile should be able to pull 60g in either lateral or longitudinal direction during the terminal phase. Both canards and tail-fins have a deflection limit of 30 deg.

Each of the tail-fins can be actuated independently of the other three. Canards on the other hand are mechanically linked in both yaw and pitch, hence they are actuated in pairs. In this DAC missile configuration only the tail-fins are used for roll stabilisation.

Table 2.1: Missile geometric and inertial properties.

Parameter	Symbol	Value	Unit
Missile Length	L	2.972	m
Missile Diameter	D	0.1981	m
Body Frontal Area	S_{ref}	0.030828	m^2
Moment Reference Center (from nose)		1.4562	m
Mass Center, Burnout (f. nose)		1.2877	m
Yaw and Pitch Moment of Inertia	I_{yy}	32	kgm^2
Roll Moment of Inertia, burn out	I_{xx}	0.320	kgm^2
Missile Mass	m_{bo}	87.27	kg
Fin Sweep Angle	δ_{max}	30	deg
Maximum Structural Limit	n_{struc}	60	g

2.2.2 Missile Aerodynamic Coefficients

This section details the aerodynamic model coefficients for DAC missile. The model consists of six coefficients: C_A axial, C_S side and C_N normal force coefficients respectively and C_l rolling, C_m pitching and C_n yawing moment coefficients. The correlation presented were determined using least squares standard regression. The model is presented in wind axis and the coefficients depend on fin deflections, body angular rates and the rates of change in wind angle (Ibarrondo, 2015). Details on the coefficient are presented in appendix A. Table 2.2 illustrates the flight envelope considered in this study. The angle-of-sideslip is restricted to a narrow range to minimise aerodynamic coupling (Ibarrondo and Sanz-Aránguez, 2016).

Table 2.2: Missile flight envelope considered in this study.

Parameter	symbol	Value	Units
Altitude	h	6096-12192/(20000-40000)	m/(ft)
Maximum angle-of-attack	α_{max}	30	deg
Operation Mach	M	1.5 -3.0	
Maximum angle-of-sideslip	β_{max}	10	deg

Equations (2.19) and (2.20) present the normal force and the pitching moment coefficients (see table A.1 and A.2 for details). The static components of the coefficients are approximated by a third-order polynomial in angle-of-attack. Deflections effects are represented by first-order terms in deflection with a coupling effect between the tail-fins and canards.

Dynamic terms are presented as linear function of pitch and angle-of-attack rate. Following from the cruciform symmetry, the side force C_S and yawing moment C_n have the same correlation structure as equation (2.19) and (2.20) with α replaced with β, β replaced with α and the pitch rate replaced with yaw rate. Figures 2.1 and 2.2 illustrate the normal force and pitching moment coefficients plots with respect to angle-of-attack at zero pitch rate and zero angle-of-sideslip.

$$\begin{aligned} C_N = {} & C_{N\alpha}\alpha + C_{N\alpha^2}\alpha|\alpha| + C_{N\alpha^3}\alpha^3 + C_{N\beta^2\alpha}\beta^2\alpha + (C_{N\delta_q^c} + C_{N\alpha\delta_q^c}\alpha + C_{N\beta^2\delta_q^c}\beta^2)\delta_q^c \\ & + (C_{N\delta_q^t} + C_{N\alpha\delta_q^t}\alpha + C_{N\beta^2\delta_q^t}\beta^2)\delta_q^t + (C_{N\delta_q^c\delta_q^t} + C_{N\alpha\delta_q^c\delta_q^t})\delta_q^c\delta_q^t + (C_{Nq}q + C_{N\dot{\alpha}}\dot{\alpha})\frac{d}{2V_m} \end{aligned} \tag{2.19}$$

where δ_q^c is the canard pitch deflection, δ_q^t tial-fin pitch deflection, V_m is the air speed and d is the missile diameter.

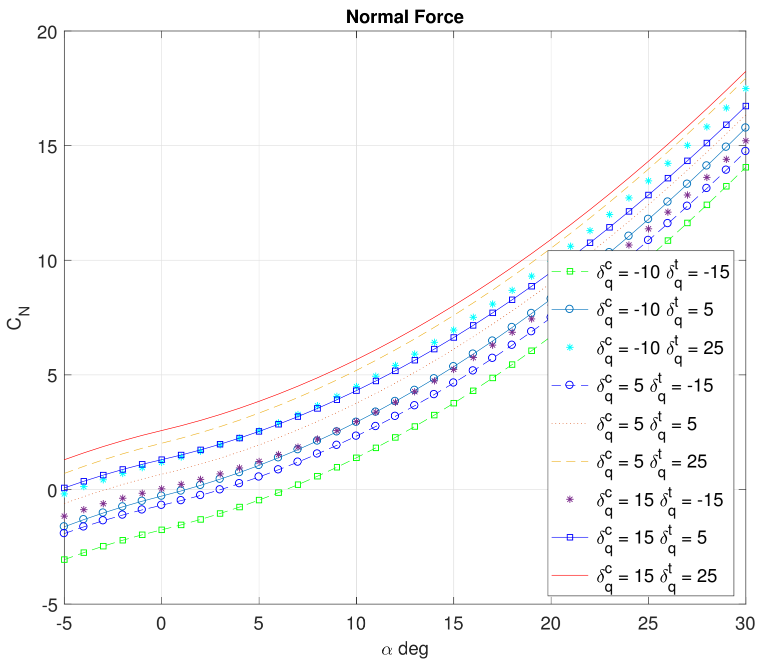

Figure 2.1: Normal force coefficient plots with respect to angle-of-attack at zero angle-of-sideslip angle for different canard and tail-fin deflections. The plot is determined at zero pitch rate at Mach 2.5

$$\begin{aligned} C_m = {} & C_{m\alpha}\alpha + C_{m\alpha^2}\alpha|\alpha| + C_{m\alpha^3}\alpha^3 + C_{m\beta^2\alpha}\beta^2\alpha + (C_{m\delta_q^c} + C_{m\alpha\delta_q^c}\alpha + C_{m\beta^2\delta_q^c}\beta^2)\delta_q^c \\ & + (C_{m\delta_q^t} + C_{m\alpha\delta_q^t}\alpha + C_{m\beta^2\delta_q^t}\beta^2)\delta_q^t + (C_{m\delta_q^c\delta_q^t} + C_{m\alpha\delta_q^c\delta_q^t})\delta_q^c\delta_q^t + (C_{mq}q + C_{m\dot{\alpha}}\dot{\alpha})\frac{d}{2V_m} \end{aligned} \tag{2.20}$$

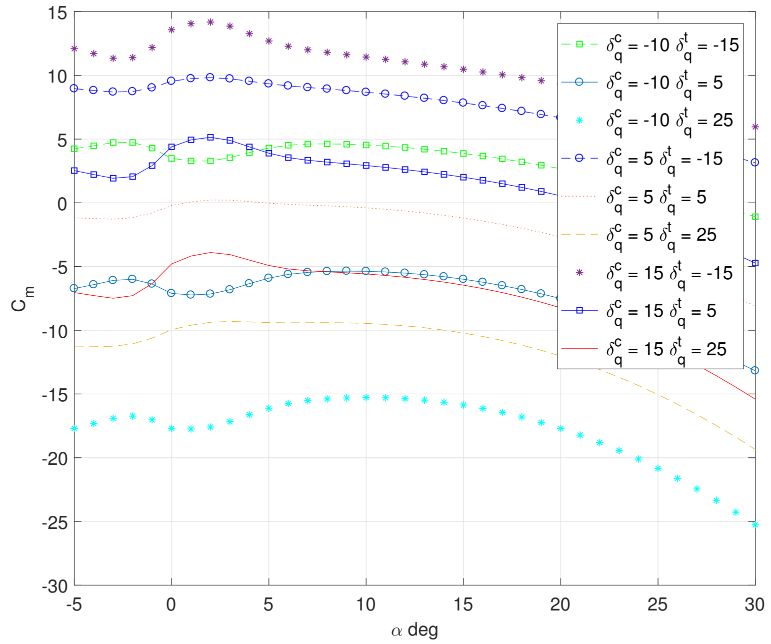

Figure 2.2: Pitching moment coefficient plots with respect to angle-of-attack at zero angle-of-sideslip for different canard and tail-fin deflections. The plot is determined at zero pitch rate and Mach 2.5

The axial force and rolling moment coefficients are given by equation (2.21) and (2.22) respectively. The values for axial force coefficient are presented in table A.4 and the values for rolling moment coefficient are presented in Table A.3.

$$\begin{aligned}C_A = {} & C_{A0} + C_{A\alpha}|\alpha| + C_{A\beta}|\beta| + C_{A\alpha^2}\alpha^2 + C_{A\alpha^3}|\alpha|^3 + \Delta C_{Ab} + (C_{A\delta_q^c} sgn(\delta_q^c) + C_{A\alpha\delta_q^c}\alpha + C_{A\beta\delta_q^c}\beta)\delta_q^c \\ & + (C_{A\delta_r^c} sgn(\delta_r^c) + C_{A\alpha\delta_r^c}\alpha C_{A\beta\delta_r^c}\beta)\delta_r^c + C_{A\delta_p}|\delta_p + (C_{A\delta_q^t} sgn(\delta_q^t) + C_{A\alpha\delta_q^t}\alpha + C_{A\alpha^2\delta_q^t}\alpha^2 + C_{A\beta\delta_q^t}\beta)\delta_q^t \\ & + (C_{A\delta_r^t} sgn(\delta_r^t) + C_{A\alpha\delta_r^t}\alpha + C_{A\alpha^2\delta_r^t}\alpha^2 + C_{A\beta\delta_r^t}\beta^3)\delta_r^t + (C_{A\delta_q^c\delta_q^t} + C_{A\alpha\delta_q^c\delta_q^t} + C_{A_{\delta_q^c{}^2\delta_q^t}}\delta_q^c + C_{A_{\delta_q^c\delta_q^t{}^2}}\delta_q^t)\delta_q^c\delta_q^t \\ & + (C_{A\delta_r^c\delta_r^t} + C_{A\alpha\delta_r^c\delta_r^t} + C_{A_{\delta_r^c{}^2\delta_r^t}}\delta_r^c + C_{A_{\delta_r^c\delta_r^t{}^2}}\delta_r^t)\delta_r^c\delta_r^t\end{aligned} \tag{2.21}$$

where δ_r^c is the canard yaw deflection and δ_r^t is the tail-fin yaw deflection.

$$C_l = C_{li}(\alpha,\beta) + C_{l\alpha\delta_q^c}\delta_q^c + C_{l\beta}\delta_q^c + C_{l\delta_p}(\alpha,\beta)\delta_p + C_{lp}g_6(\alpha,\beta)p\frac{d}{2V_m} \tag{2.22}$$

where δ_p is the roll deflection of the tail-fins.

2.3 Trim Performance

Missile pitch manoeuvre performance at trim is of particular interest in missile design. Firstly because guidance law based on proportional navigation outputs the lateral and normal acceleration necessary to intercept a target; secondly a solid rocket propelled missile has no way of controlling the thrust once the motor is ignited. This section presents pitch manoeuvre capability of the DAC missile which also translates to yaw capability following from cruciform symmetry. To assess the manoeuvre performance at trim condition, the sum of the pitching moment must add up to zero and the pitch rate must be at steady state. Equations (2.23) and (2.24) are used to define the pitch trim condition (Blakelock, 1991):

$$C_{mtrim}(\alpha_{trim}, \delta^c_{qtrim}, \delta^t_{qtrim}) = (C_m + \bar{s}C_N)_{trim} \tag{2.23}$$

$$n_{trim} = \frac{\bar{q}S_{ref}}{m} C_{N_{trim}} \tag{2.24}$$

Table 2.3: Flight envelope variables.

Variable	symbol	min value	max value	Units
Angle-of-attack	α	-30	30	deg
Load factor	n_{trim}	-60	60	g
Canard deflection	δ^c_{qtrim}	-30	30	deg
Tail-fin deflection	δ^t_{qtrim}	-30	30	deg

The trim condition has two equations and four unknowns ($\alpha_{trim}, \delta^c_{qtrim}, \delta^t_{qtrim}$ and n_{trim}) hence it has no unique solution. To determine the trim condition an angle-of-attack and load factor within the acceptable range as defined in Table 2.3 were selected and used with Eqs. (2.23) and (2.24) to solve for the canard and tail-fin deflections. The solution was accepted only if the deflections lie within the mechanical limits of the servos. Figure 2.3 illustrates the trim map at different angles-of-attack for different load factors. The map is split into two regions (the stable and the unstable trim regions) by a neutrally stable tail-fin-controlled configuration. The static stability of each trim point was determined by evaluating $\frac{\partial C_m}{\partial \alpha}$ at each trim point evaluated.

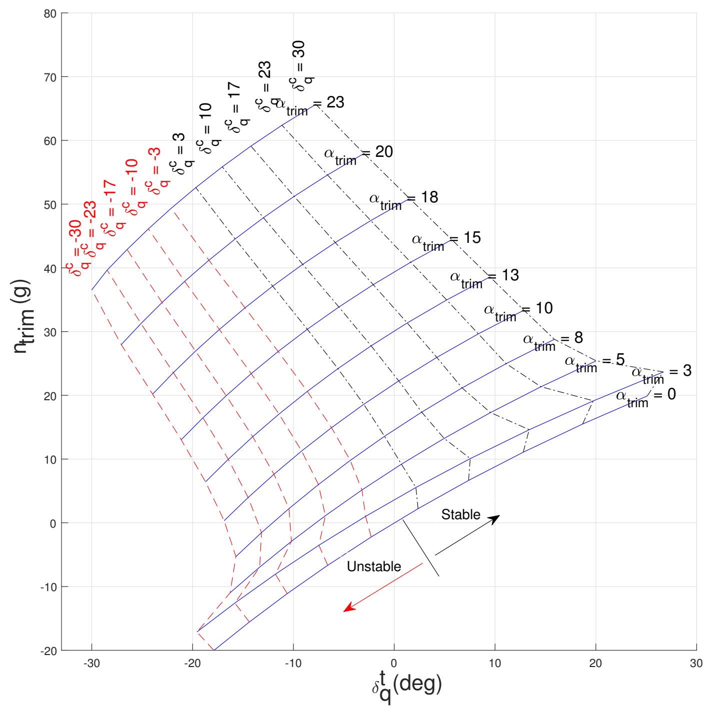

Figure 2.3: Pitch trim map for DAC missile at 6096 m (20000ft) altitude at Mach 2.5. The map presented corresponds to burned out flight condition.

2.4 Open-Loop Response

This section presents the nonlinear open-loop response of the missile model at trim conditions for different control modes. Figures 2.4, 2.5 and 2.6 illustrate the angle-of-attack, normal load factor and pitch rate response to canard and tail-fin inputs that correspond to 15g of normal acceleration at different control modes. The diverted mode results in a low angle-of-attack demand for the same load factor while the tail-only mode results in a high angle-of-attack requirement for the same load factor. The diverted mode has most of the lift forces carried by the control surface hence a large net lift at low angle-of-attack, whereas tail-fin mode has the tail-fin lift opposing the body lift force, hence a high angle-of-attack is needed to compensate for the opposing tail-fin lift. The overall observation from the open-loop responses of all the modes is that the missile is highly under-damped.

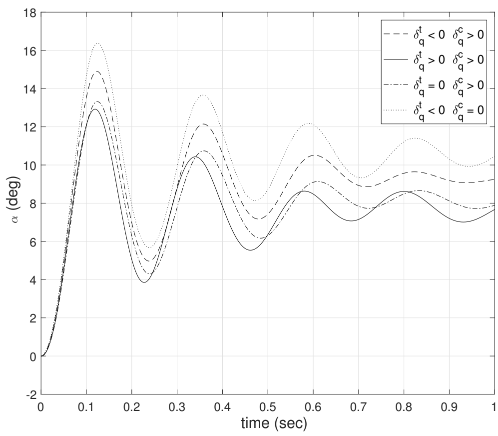

Figure 2.4: Nonlinear AoA response for different DAC missile control modes to an input step command of 15g normal load factor.

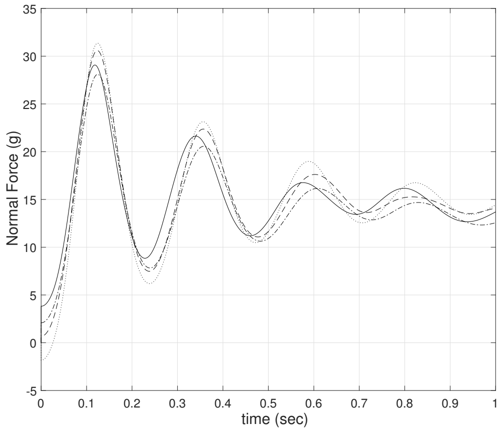

Figure 2.5: Nonlinear normal load factor response for different DAC missile control modes to an input step command of 15g normal load factor.

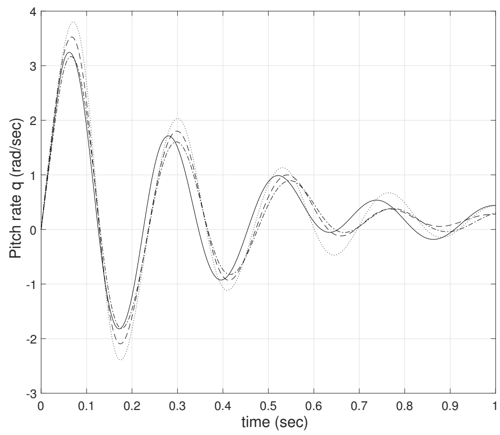

Figure 2.6: Nonlinear pitch rate response for different DAC missile control modes to an input step command of 15g normal load factor.

Chapter 3

DAC Missile Reference Control Model

This chapter details the design of an NDI controller for a DAC missile. The NDI controller response is compared with a benchmark gain-scheduled controller to assess relative performance. Inclusion of gain scheduling was necessary because it is the predominant controller design in missile autopilot applications. Furthermore, a poorly designed reference model will result in poor adaptive controller performance.

The NDI controller presented here lays the foundation for the controller used in Chapter 4 on the MRAC, MRAC controller is an adaptive controller that consists of a reference model, baseline controller design with the known missile dynamics, adaptive element and the uncertain plant to be controlled. The reference model, baseline controller and the adaptive element work together to accommodate the plant uncertainty and ensure that the plant tracks the reference model to acceptable margins. The adaptive element consists of the approximation function and an adaptive rule to perform online compensation for uncertainty due to unmodelled dynamics (Nguyen, 2018).

3.1 Gain-Scheduled Autopilot

Gain scheduling is a traditional philosophy used to control nonlinear plants by redefining the plant as a family of linear-time-invariant (LTI) model about selected equilibrium points (Balakrishnan et al., 2012). The concept of gain scheduling is applicable with most linear controller design techniques. Gain-scheduled controllers are common in flight control applications because of their high reliability and easy to implement nature. The gain-scheduled controller detailed in this chapter will serve as a benchmark model for the NDI controller implemented in this study.

3.1.1 Missile Dynamics Linearization

Linearisation requires missile dynamics to be decoupled into three control channels: pitch, yaw and roll to simplify the controller design process. Decoupling of the dynamics is made possible by relatively weak coupling dynamics between the lateral, longitudinal and roll dynamics at the vicinity of each linearisation points (especially at low angles-of-attack). The simplification allows the engineer to design an initial iteration controller gains for each channel separately. The missile dynamics in the lateral and longitudinal planes can be further separated into two modes: short-period mode and phugoid mode. Phugoid mode is a low-frequency dynamics that are a consequence of energy exchange between kinetic and potential energy in the gravitational field. The short-period dynamics are high-frequency damped dynamics (Blakelock, 1991). Short-period dynamics result in very little trajectory changes over the time it takes to be damped-out. The short-period dynamics are of interest when designing an acceleration-based autopilot since the forces are primarily determined by wind attitudes. The following derivation details the missile translation dynamics and the linearised longitudinal short-period dynamics in the missile wind axes (Zipfel, 2007).

The body velocity vector in wind axes is defined as follows:

$$\begin{bmatrix} u \\ v \\ w \end{bmatrix} = \begin{bmatrix} V_m \cos\alpha \cos\beta \\ V_m \sin\beta \\ V_m \sin\alpha \cos\beta \end{bmatrix} \tag{3.1}$$

Taking the time derivative of Eqs. (3.1) yields the body acceleration vector in wind axis as follows:

$$\begin{bmatrix} \dot{V}_m \\ V_m\dot{\alpha} \\ V_m\dot{\beta} \end{bmatrix} = \mathcal{G} \begin{bmatrix} \dot{u} \\ \dot{v} \\ \dot{w} \end{bmatrix} \tag{3.2}$$

$\mathcal{G}$ is a transformation matrix between body and wind axes that depends on wind angles :

$$\mathcal{G} = \frac{-1}{\cos\beta} \begin{bmatrix} -\cos\alpha\cos^2\beta & -\sin\beta\cos\beta & -\sin\alpha\cos^2\beta \\ \sin\alpha & 0 & -\cos\alpha \\ \sin\beta\cos\beta\cos\beta & -\cos^2\beta & \sin\alpha\sin\beta\cos\beta \end{bmatrix}$$

Substituting Eq. (3.2) into Eq. (2.9) yields the following translation equation in wind axis (Zipfel, 2007):

$$\begin{bmatrix} \dot{V}_m \\ V_m\dot{\alpha} \\ V_m\dot{\beta} \end{bmatrix} = \mathcal{G} \begin{bmatrix} V_m(r\sin\beta - q\sin\alpha\cos\beta) \\ V_m(p\sin\alpha - r\cos\alpha\cos\beta) \\ V_,(q\cos\alpha\cos\beta - p\sin\beta) \end{bmatrix} + \mathcal{G}g \begin{bmatrix} -\sin\theta \\ \sin\phi\cos\theta \\ \cos\phi\cos\theta \end{bmatrix} + \mathcal{G}\frac{1}{m}\begin{bmatrix} A \\ S \\ N \end{bmatrix} \tag{3.3}$$

$$\begin{aligned} \dot{V}_m = &-\cos\alpha\cos\beta\left(\frac{A}{m} - g\sin\theta\right) - \sin\beta\left(\frac{S}{m} + g\sin\phi\sin\theta\right) \\ &- \sin\alpha\cos\beta\left(\frac{N}{m} + g\cos\phi\cos\theta\right) \end{aligned} \tag{3.4a}$$

$$\begin{aligned} \dot{\alpha} = &\frac{1}{V_m\cos\beta}\left[\left(\frac{A}{m} - g\sin\theta\right)\sin\alpha - \left(\frac{N}{m} + g\cos\phi\cos\theta\right)\cos\alpha\right] \\ &+ q - \tan\beta(p\cos\alpha - r\sin\alpha) \end{aligned} \tag{3.4b}$$

$$\begin{aligned} \dot{\beta} = &\frac{1}{V_m}\left[\left(\frac{A}{m} - g\sin\theta\right)\cos\alpha - \left(\frac{S}{m} + g\cos\phi\cos\theta\right)\right]\cos\beta \\ &+ \frac{1}{V_m}\left(\frac{N}{m} + g\cos\phi\cos\theta\right)\sin\alpha\sin\beta + p\sin\alpha - r\cos\alpha \end{aligned} \tag{3.4c}$$

The following assumptions were made when defining the longitudinal short-period dynamics:

- V_m is varying slowly and the effect on the short-period dynamics is negligible.
- The cross-coupling dynamics between pitch-yaw and roll-pitch are negligible ($\beta = p = r = 0$).
- The gravitational acceleration has little effect on the short-period dynamics.

Following the above assumptions, the reduced nonlinear longitudinal short-period dynamics are given by:

$$\dot{\alpha} = \frac{1}{V_m}\left(\frac{A}{m}\sin\alpha - \frac{N}{m}\cos\alpha\right) + q \tag{3.5a}$$

$$I_{yy}\dot{q} = M \tag{3.5b}$$

The nonlinearities in the reduced Eq. (3.5) are due to the aerodynamic loads and the trigonometric function. Trigonometric functions are linearised around trim point using

Taylor series expansion. The reduced normal force (Z), axial force (A) and pitching moment (M) are functions of angle-of-attack and control surface deflections in the longitudinal dynamics at steady state.

$$Z = \bar{q} S_{ref} C_N(\alpha, \delta_q^c, \delta_q^t) \tag{3.6a}$$

$$A = \bar{q} S_{ref} C_A(\alpha, \delta_q^c, \delta_q^t) \tag{3.6b}$$

$$M = \bar{q} S_{ref} d C_m(\alpha, \delta_q^c, \delta_q^t) \tag{3.6c}$$

where S_{ref} is the cross-sectional area of the missile.

Linearising the aerodynamic coefficients using Taylor series expansion about a point $(\alpha_0, \delta_{q0}^t \delta_{q0}^c)$ yields the following first-order coefficients. The function $\mathcal{O}$ represents the uncertainty due to the neglected high-order terms.

$$C_A = \bar{C}_{A_0} + \mathcal{O}_A(\Delta\alpha, \Delta\delta_q{}^c, \Delta\delta_q{}^t) \tag{3.7a}$$

$$C_N = \bar{C}_{N_\alpha}\Delta\alpha + \bar{C}_{N_{\delta_q^t}}\Delta\delta_q^t + +\bar{C}_{N_{\delta_q^t}}\Delta\delta_q^c + \mathcal{O}_N(\Delta\alpha^2, \Delta\delta^c{}_q{}^2, \Delta\delta_q^{t\,2}) \tag{3.7b}$$

$$C_m = \bar{C}_{m_\alpha}\Delta\alpha + \bar{C}_{m_{\delta_q^t}}\Delta\delta_q^t + +\bar{C}_{m_{\delta_q^t}}\Delta\delta_q^c + \mathcal{O}_m(\Delta\alpha^2, \Delta\delta^c{}_q{}^2, \Delta\delta_q^{t\,2}) \tag{3.7c}$$

Following from the linearisation of the aerodynamic coefficients the short period dynamics of the DAC missile are defined by Eq. (3.8a). The state matrix remains in the format similar to that of canard-only or tail-fin-controlled missile as expected since the state matrix is independent of the control inputs. The resulting control matrix is a 2×2 matrix as a result of the two control inputs.

$$\begin{bmatrix} \dot{\alpha} \\ \dot{q} \end{bmatrix} = \frac{\bar{q} S_{ref} d}{V_m} \begin{bmatrix} \dfrac{\bar{C}_{A_0} - \bar{C}_{N_\alpha}}{md} & 1 \\ \dfrac{\bar{C}_{m_\alpha} + \bar{s}\bar{C}_{N_\alpha}}{I_{yy}} & 0 \end{bmatrix} \begin{bmatrix} \alpha \\ q \end{bmatrix} + \frac{\bar{q} S_{ref} d}{V_m} \begin{bmatrix} \dfrac{\bar{C}_{N_{\delta_q^t}}}{md} & \dfrac{\bar{C}_{N_{\delta_q^c}}}{md} \\ \dfrac{\bar{C}_{m_{\delta^t{}_q}} + \bar{C}_{N_{\delta^t{}_q}}}{I_{yy}} & \dfrac{\bar{C}_{m_{\delta^c{}_q}} + \bar{C}_{N_{\delta_q^c}}}{I_{yy}} \end{bmatrix} \begin{bmatrix} \delta_q^t \\ \delta_q^c \end{bmatrix} \tag{3.8a}$$

$$\begin{bmatrix} a_z \\ q \end{bmatrix} = \bar{q} S_{ref} \begin{bmatrix} \dfrac{\bar{C}_{N_\alpha}}{m} & 0 \\ 0 & 1 \end{bmatrix} \begin{bmatrix} \alpha \\ q \end{bmatrix} + \bar{q} S_{ref} \begin{bmatrix} \dfrac{\bar{C}_{N_{\delta_q^t}}}{m} & \dfrac{\bar{C}_{N_{\delta_q^c}}}{m} \\ 0 & 0 \end{bmatrix} \begin{bmatrix} \delta_q^t \\ \delta_q^c \end{bmatrix} \tag{3.8b}$$

The linearised short-period dynamics will be used in the next section to design a gain-scheduled three-loop autopilot. Due to the cruciform symmetry the same linearised equations apply in the lateral dynamics with α replaced with β, a_z by a_y and the pitch deflection with yaw deflections. The trim map demonstrated in section 2.3 was used to obtain the LTI models necessary to design a gain-scheduled controller. Due to the nature of dual control having two inputs, this results in an indeterminate trim problem with one equation and three unknowns. Hence, two variables must be fixed to determine a closed solution in contrast to tail-fin or canard-controlled missile where the trim angle-of-attack is sufficient to determine a unique trim solution at a given airspeed (Blakelock, 1991). In the current study, the trim angle-of-attack and canard deflection were fixed and the tail deflection unconstrained to achieve a unique trim point. As a result of having a non-unique solution at each trim angle-of-attack, the gain-scheduler has three scheduling parameters dynamic pressure, angle-of-attack and the canard deflection to ensure unique trim point (Mracek and Ridgely, 2006).

3.1.2 Control Architecture

The common three-loop autopilot topology (often dubbed the " Raytheon autopilot " (Mracek and Ridgely, 2006) or "Nesline autopilot" (Kantue, 2017)) will be used as the gain-scheduled controller. Three-loop autopilot has a fixed control structure that uses accelerations and body rates measured by an inertial measurement unit (IMU) to generate fin deflections (Jackson, 2010). A missile controlled using this topology is usually roll stabilised in the cross or plus configuration. In the current study the missile is roll-stabilised in the plus because of the resulting low cross coupling between canards and tail-fins at this configuration (Ibarrondo, 2015). Vast literature exists on the design and flight testing of the three-loop-autopilot hence it is a suitable benchmark controller for the proposed NDI controller (Lee et al., 2016, Mracek, 2015). Three-loop autopilot aims to control system damping and the system time to ensure desired robustness and performance (Kantue, 2017). Figure 3.1 depicts the three-loop autopilot used on longitudinal dynamics of the DAC missile in the current study.

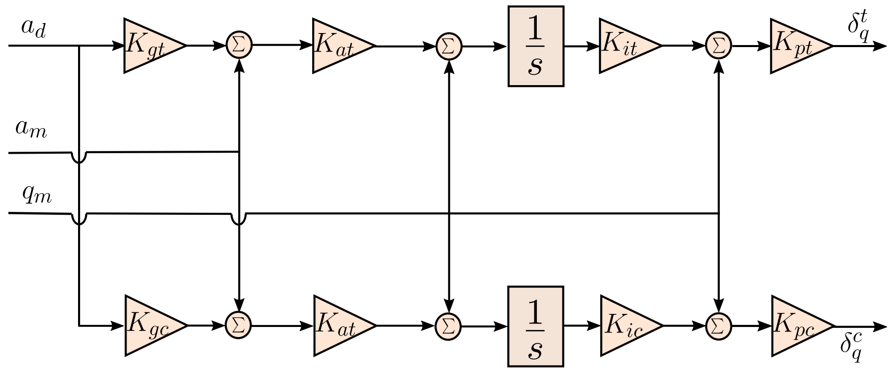

Figure 3.1: Three-loop autopilot topology for a DAC missile (Mracek and Ridgely, 2006).

The controller is made up of two three-loop autopilots, one to generate canard and the other for tail-fins command deflections. Typical closed-loop specifications when designing a three-loop autopilot are: acceleration damping ratio ζ_m, time constant τ_m and open-loop crossover frequency ω_{cr} (Jackson, 2010) . The crossover frequency is independent of the time constant and ensures robustness against unmodelled high-frequency dynamics (Zarchan, 2012). Normal practice is to set the crossover frequency to be about one third of the actuator bandwidth while keeping it clear of the airframe natural frequency (ω_{AF}). ζ_m is selected to ensure sufficient disturbance rejection while the selection of τ_m is driven by the desired tracking performance. The figure-of-merit (FOM) were used to design the longitudinal autopilot (Jackson, 2010):

- Performance FOM:
  - Time constant τ_m: 0.125 sec
  - Overshoot δ : 30 %
  - Steady-state error : 5.0%
  - Settling time τ_f : 0.25 sec
  - Closed-loop damping ratio ζ_m: 0.8
  - Cross-over frequency ω_{cr}: 50 rad
- Robustness FOM at actuator input:
  - Gain Margin 6 dB
  - Phase Margin 30 deg

The gain-scheduled controller was designed using Matlab *control design* and *control system* toolbox for the above FOMs. The trim points necessary to generate a family of LTI were obtained using Matlab routine *"findop"* for different dynamic pressures, angle-of-attack and canard deflections at an unknown steady pitch rate. Canard deflection constraint is necessary to guarantee unique trim solutions. Gain-scheduled three-loop-autopilot for the LTI family were tuned with Matlab *"systune"* using above FOM. Table 3.1 illustrates the discrete parameters used to design the scheduled gains and the corresponding parameter ranges.

Table 3.1: Parameter envelope used to design and schedule the three-loop autopilot gains.

	symbol	No. GS Points	Min value	Max value	Units
Angle-of-attack	α	5	0	30	deg
Airspeed	V_m	3	500	1200	m/s
Canard deflection	δ_q^c	10	-30	30	deg
Altitude	h	3	20000/(6096)	40000/(ft)	

Figures 3.2 and 3.3 illustrate the tuned three loop autopilot gains for different angles-of-attack and canard deflections at an airspeed of 700 m/s and an altitude of 9144 m (30000 ft).

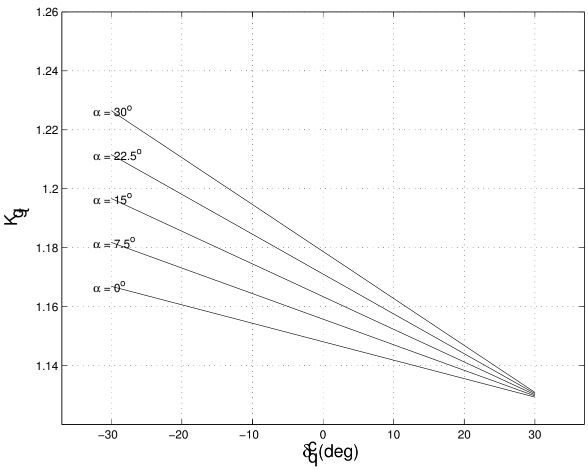

(a) Kg tail-fin gain

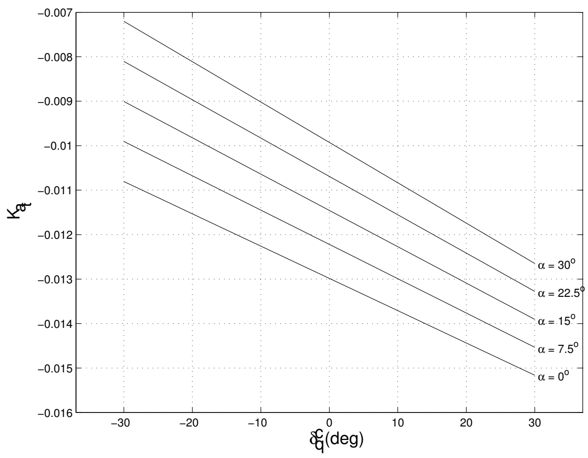

(b) Ka tail-fin gain

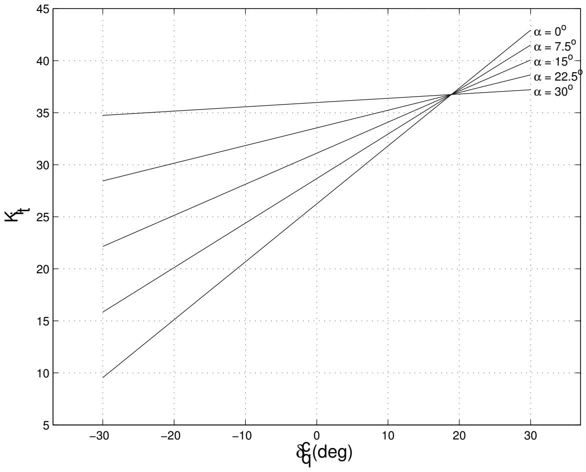

(c) Ki tail-fin gain

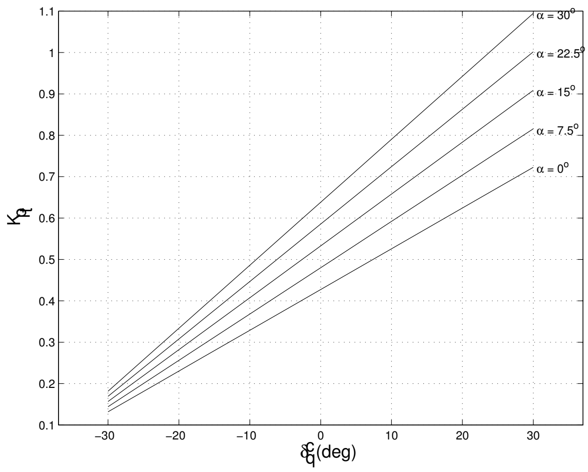

(d) Kp tail-fin gain

Figure 3.2: Tail-fin-control three-loop-autopilot gains for different canard deflection and angles-of-attack at an airspeed of 700 m/s and an altitude of 9144 m (30000 ft)

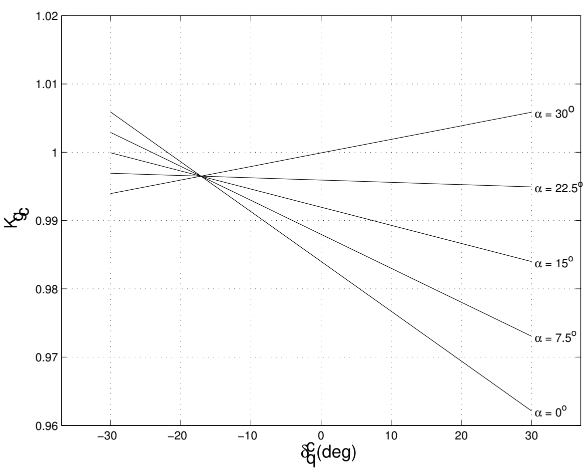

(a) Kg canard gain

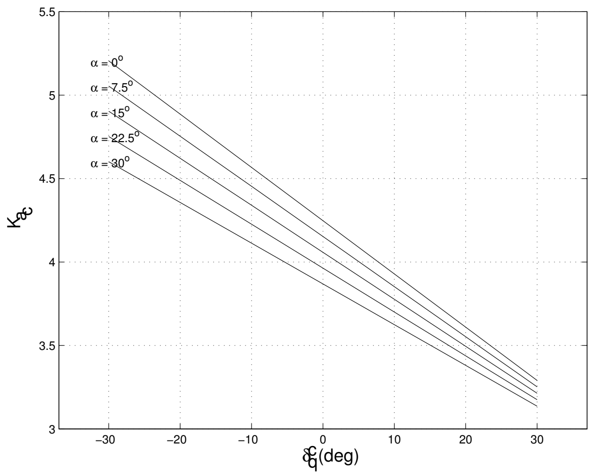

(b) Ka canard gain

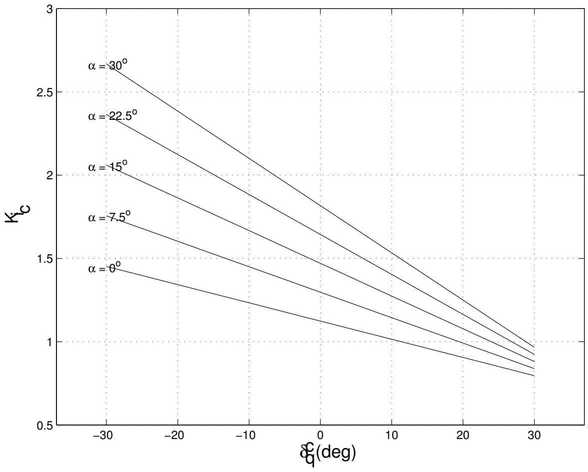

(c) Ki canard gain

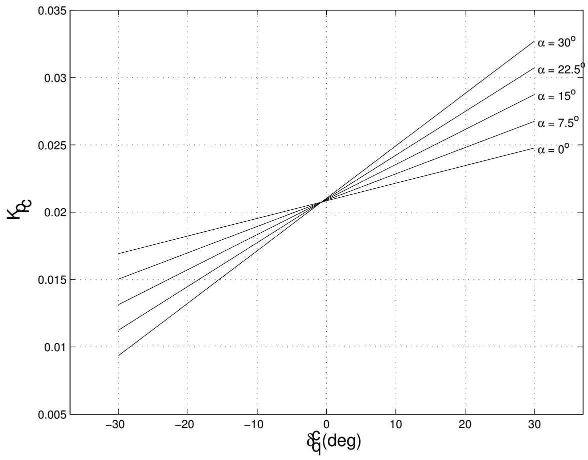

(d) Kp canard gain

Figure 3.3: Canard-control three-loop-autopilot gains for different canard deflections and angles-of-attack at an airspeed of 700 m/s and an altitude of 9144m (30000 ft)

3.2 Results: Gain-Scheduled Autopilot.

Figures 3.4 to 3.8 compare longitudinal response of gain-scheduled three-loop autopilot controlled DAC missile with canards and tail-fin controlled missile. The normal acceleration (see Fig. 3.4) response of the tail-fin exhibits undershoot dynamics that are attributed to the non-minimum phase behaviour. The canard-controlled missile has significantly large overshoot and oscillations. Response of the DAC missile eliminates both the tail-fin undershoot and the canard overshoot resulting in quicker smooth acceleration response. Overall the dual controller configuration has the quickest response out of the three configurations.

Both the canard-only and tail-fin-only show significant changes in angle-of-attack for each acceleration command step change (see Fig.3.5). Tail-fin-only missile has the highest angle-of-attack response at all times. This phenomenon is attributed to the fact that extra body lift is needed to overcome the opposing induced by the tail-fins to produce the desired pitching moment. Angle-of-attack response of the canard-only (see Fig.3.5) is less significant when compared to tail-fin-only because both canard and body lift are in the same direction. Dual-controlled missile angle-of-attack response follows a different trajectory when compared to the canard-only and tail-fin-only responses. The discrepancy is attributed to the fact that for the given initial condition and commands the missile diverted mode is sufficient to achieve acceleration commands. It is worth noting that the desired pitch rate and angle-of-attack are driven by acceleration error and follow different dynamics for each configuration.

Due to the diverted mode control, the pitch rate of the DAC missile configuration results in a small variation (see Fig. 3.6) at each acceleration command change because of the small body lift contribution in tracking the command. The diverted mode is evident from the fact that the angle-of-attack is sluggish in response, indicating a strong heaving motion. Furthermore, both the tail-fin and canard commands (see Figs.3.7 and 3.8) of the dual controller are of the same polarity. In addition, the magnitude of the deflection of the tail-fin and canard are significantly larger for dual controller because most of the lift force necessary to achieve the desired accelerations is carried by the control surfaces.

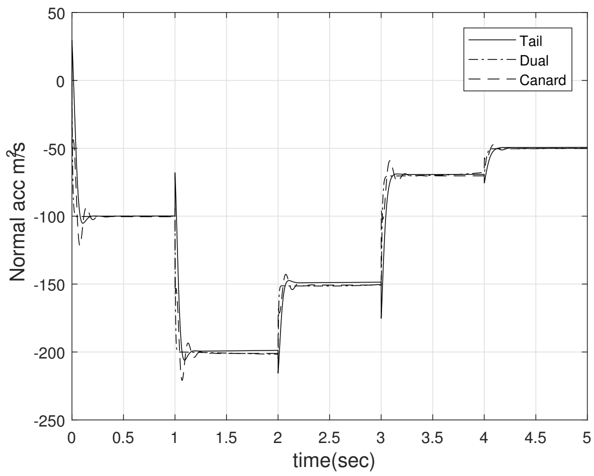

Figure 3.4: Normal load factor response of three different missile control surface configuration (tail-fin, DAC and canard) controlled using gain-scheduled acceleration based three-loop autopilot.

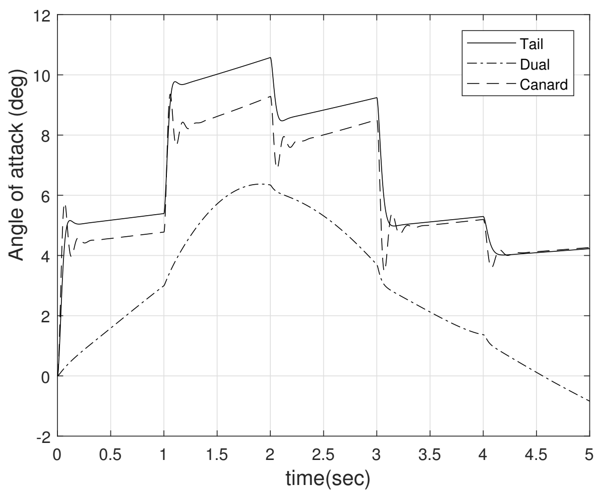

Figure 3.5: Angle-of-attack response of three different missile control surface configuration (tail-fin, DAC and canard) controlled using gain-scheduled acceleration-based three-loop autopilot.

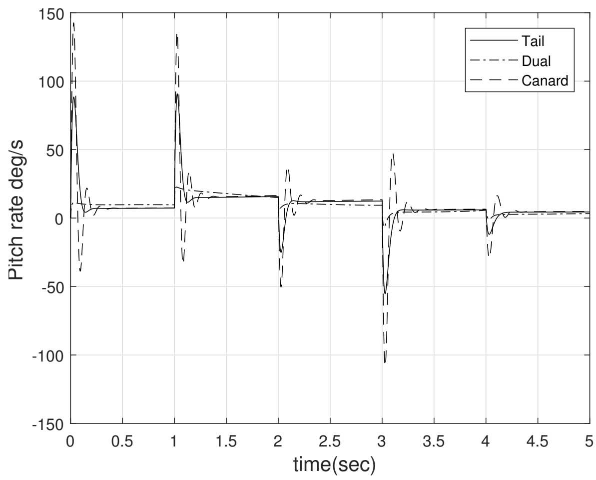

Figure 3.6: Pitch rate response of three different missile control surface configurations (tail-fin, DAC and canard) controlled using gain-scheduled acceleration-based three-loop autopilot.

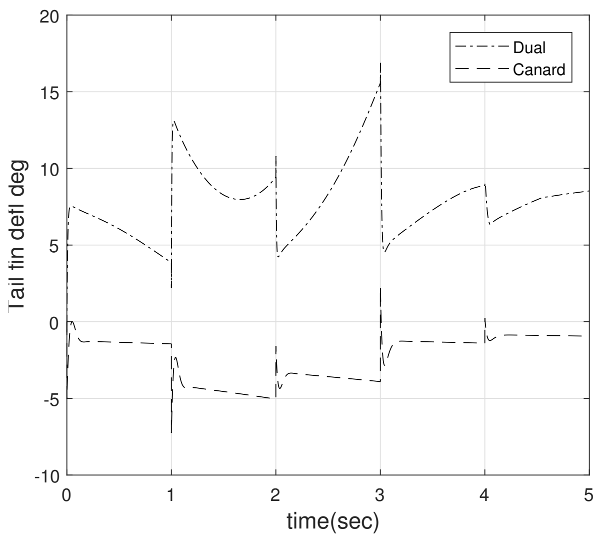

Figure 3.7: Tail-fin deflection commands for two different missile control surface configurations (tail-fin and DAC) controlled using gain-scheduled acceleration-based three-loop autopilot.

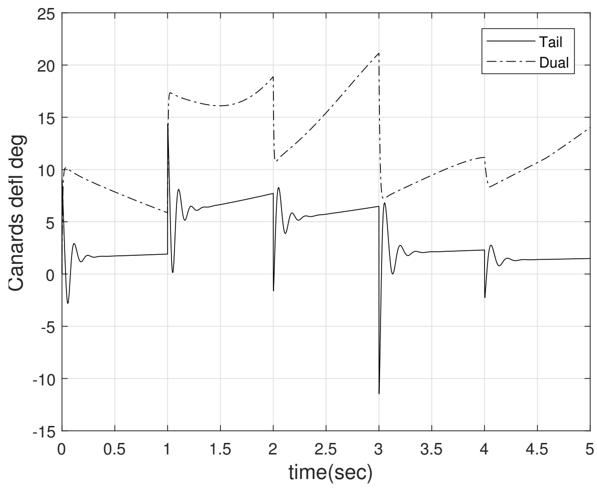

Figure 3.8: Canard deflection commands for two different missile control surface configurations (canard and DAC) controlled using gain-scheduled acceleration-based three-loop autopilot.

3.3 Nonlinear Dynamic Inversion.

A plethora of literature exists on NDI application to aerospace vehicles (Calise et al., 2000, Padhi et al., 2007). Two commonly used NDI topologies in missile control are the two time-scale separation and output redefinition approach (Balakrishnan et al., 2012, Ryu et al., 1997). The two techniques are able to account for non-minimum phase associated with acceleration autopilot on tail-fin missile. Two time-scale separation splits the dynamics of the missile into fast and slow dynamics; output parameter redefinition is achieved by defining new parameter dynamics that eliminates the restricting non-minimum phase property in the feedback. The redefined output in the literature is usually a combination of angle-of-attack and the pitch rate dynamics for longitudinal autopilot. For the current study only the two time-scale separation technique will be considered.

3.3.1 Two Time-Scale Separation NDI Autopilot

Two time-scale separation approach eliminates the non-minimum phase limitation that affects NDI autopilot for tail-fin-controlled missile with acceleration autopilot. Figure 3.9 illustrates the NDI controller architecture for DAC missile,the architecture is a parallel implementation of NDI-controllers for tail-fin and canard to simplify the controller design. Each NDI controller independently determines the desired dynamics based on the feedback accelerations, wind angles and body rates. The illustrated topology also holds for the lateral dynamics following from the airframe symmetry. The fast dynamics are defined by the angular dynamics and the slow dynamics by the wind angles dynamics. Inversion of the fast dynamics forms the inner loop controller used to determine the desired tail-fin and canard deflections necessary to track the commanded accelerations. The input to the fast dynamic inversion controller is pitching acceleration. Slow dynamic inversion forms the second inner loop that determines the pitch commands to be tracked by the inner-inner loop. The outer-most loop is closed with a PI controller of the load factor command which generates the desired wind angle commands for the slow dynamic inversion. The PI is necessary to ensure robustness against plant inversion uncertainties.

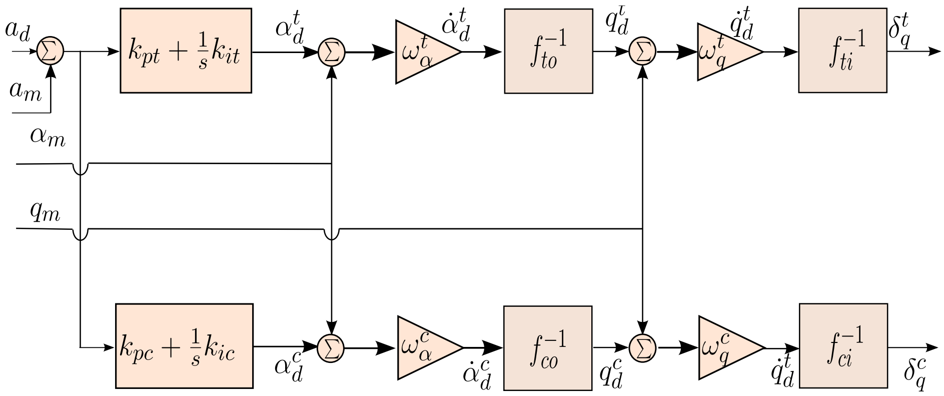

Figure 3.9: Two time separation NDI autopilot topology for a DAC missile

3.3.2 Slow Dynamics NDI

The slow missile dynamics are defined to be the wind angle dynamics due to their sluggish response when compared to missile attitude dynamics. The inversion of the slow dynamics is used to determine the desired pitch and yaw acceleration from desired wind angle rates. Equation (3.9) defines the inversion of the slow dynamics to determine the desired pitch and yaw rates:

$$\begin{bmatrix} q_d \\ r_d \end{bmatrix} = \begin{bmatrix} \dot{\alpha}_d - \dfrac{1}{V_m \cos\beta}\left(\dfrac{A_o}{m}\sin\alpha - \dfrac{Z_o}{m}\cos\alpha\right) + (p\cos\alpha - r\sin\alpha)\tan\beta \\ \dfrac{1}{\cos\alpha}\left(-\dot{\beta}_d + \dfrac{1}{V_m}\left(\dfrac{X_o}{m}\cos\alpha\cos\beta - \dfrac{S_o}{m}\cos\beta + \dfrac{Z_o}{m}\sin\alpha\sin\beta\right) + p\sin\alpha\right) \end{bmatrix} \tag{3.9}$$

Desired wind angle rates were selected to be first-order system defined as follows:

$$\begin{bmatrix} \dot{\alpha}_d \\ \dot{\beta}_d \end{bmatrix} = \begin{bmatrix} \omega_\alpha & 0 \\ 0 & \omega_\beta \end{bmatrix} \begin{bmatrix} \alpha_d - \alpha_m \\ \beta_d - \alpha_m \end{bmatrix} \tag{3.10}$$

where ω_α and ω_β are the wind-angles bandwidth; α_d and β_d are the desired wind angles; β_m and α_m are the measured wind-angles.

The terms A_o, S_o and Z_o represent the aerodynamic force due to the contribution of the static terms. It is assumed that the effects of aerodynamic surfaces and dynamic terms are negligible when determining the desired body rates from the slow missile dynamics.

$$A_o = \bar{q}S_{ref}(C_{A_0} + C_{A_\alpha}|\alpha| + C_{A_\beta}|\beta| + C_{A^2_\alpha}\alpha^2 + C_{A^3_\alpha}|\alpha|^3) \tag{3.11a}$$

$$S_o = \bar{q}S_{ref}(C_{S_\beta}\beta + C_{S^2_\beta}\beta|\beta| + C_{S^3_\beta}\beta^3 + C_{S^2_\alpha\beta}\alpha^2\beta + (C_{S_r}r + C_{S_{\dot{\beta}}})\dot{\beta}) \tag{3.11b}$$

$$Z_o = \bar{q}S_{ref}(C_{N_\alpha}\alpha + C_{N^2_\alpha}\alpha|\alpha| + C_{N^3_\alpha}\alpha^3 + C_{N^2_\beta\alpha}\beta^2\alpha + (C_{N_q}q + C_{N_{\dot{\alpha}}})\dot{\alpha}) \tag{3.11c}$$

The desired wind angles are determined from proportional-integral (PI) controller of the normal and lateral load factor as follows:

$$\alpha_d = k_{p_z}(a_{z_d} - a_{z_m}) + k_{i_z}\int(a_{z_d} - a_{z_m})dt \tag{3.12a}$$

$$\beta_d = k_{p_y}(a_{y_d} - a_{y_m}) + k_{i_y}\int(a_{y_d} - a_{y_m})dt \tag{3.12b}$$

where k_{p_z} and k_{p_y} are the proportional gains, k_{i_z} and k_{i_y} are the integral gains for normal and lateral load factors. The PI gains were generated using Matlab control toolboxes for the same FOM as the gain-scheduled autopilot.

3.3.3 Fast Dynamics NDI

The inversion of the angular dynamics is defined as the fast NDI because of the small time constant associated with them. The outputs of the fast dynamic inversion are the tail-fin and canard deflections. Because of the two actuator mechanisms, the fast dynamics were separated into tail-fin-only and canard-only fast dynamics to simplify the design process. The tail-fin dynamic inversion involves all rotational dynamics while the canard dynamic inversion only involves the pitch and yaw dynamics. Equation (3.13) is the inversion used to determine the necessary tail-fin deflection to track the desired pitch ($\dot{q}^t_d$), yaw ($\dot{r}^t_d$) and roll ($\dot{p}^t_d$) accelerations.

$$\begin{bmatrix} \delta_p \\ \delta_q^t \\ \delta_r^t \end{bmatrix} = \frac{1}{\bar{q}S_{ref}d} \begin{bmatrix} 0 & 0 & C_{l_p} \\ C_{m_{\delta_q^t}} + \bar{s}C_{S_{\delta_q^t}} & 0 & 0 \\ 0 & C_{n_{\delta_r^t}} - \bar{s}C_{S_{\delta_q^t}} & 0 \end{bmatrix}^{-1} \begin{bmatrix} I_{xx}\dot{p}_d^t - f_l(\alpha,\beta,p) \\ I_{yy}\dot{q}_d^t - (I_{yy} - I_{xx})pr - f_m(\alpha,\beta,\dot{\alpha},q) \\ I_{yy}\dot{r}_d^t - (I_{xx} - I_{yy})pq - f_n(\alpha,\beta,\dot{\beta},r) \end{bmatrix} \tag{3.13}$$

wheref_l, f_m and f_n are the static and dynamic terms of the roll, pitch and yaw moment.

The desired tail-fin control angular accelerations were selected to be first-order system and defined as follows:

$$\begin{bmatrix} \dot{q}_d^t \\ \dot{r}_d^t \\ \dot{p}_d^t \end{bmatrix} = \begin{bmatrix} \omega_q & 0 & 0 \\ 0 & \omega_r & 0 \\ 0 & 0 & \omega_p \end{bmatrix} \begin{bmatrix} q_d^t - q_m \\ r_d^t - r_m \\ p_d^t - r_m \end{bmatrix} \tag{3.14}$$

where q_m, r_m and p_m are the measured body rates and; ω_q, ω_r and ω_p are the body rate controller bandwidths.

Equation (3.15) defines the dynamic inversion of the angular dynamics used to determine the necessary canard deflection to track the desired pitch and yaw accelerations. The effect of the canard on the roll dynamics was neglected to simplify the inversion process.

$$\begin{bmatrix} \delta_q^c \\ \delta_r^c \end{bmatrix} = \frac{1}{\bar{q}S_{ref}d} \begin{bmatrix} C_{m_{\delta_q^c}} + \bar{s}C_{N_{\delta_q^c}} & 0 \\ 0 & C_{n_{\delta_r^c}} - \bar{s}C_{S_{\delta_r^c}} \end{bmatrix}^{-1} \begin{bmatrix} I_{yy}\dot{q}_d^c - (I_{yy} - I_{xx})pr - f_m(\alpha,\beta,\dot{\alpha},q) \\ I_{yy}\dot{r}_d^c - (I_{xx} - I_{yy})pq - f_n(\alpha,\beta,\dot{\beta},r) \end{bmatrix} \tag{3.15}$$

where q_d^c and r_d^c are the desired canard control pitch rate and yaw rate respectively.

The desired canard-control angular accelerations were selected to be first-order system and defined as follows:

$$\begin{bmatrix} \dot{q}_d^c \\ \dot{r}_d^c \end{bmatrix} = \begin{bmatrix} \omega_q & 0 \\ 0 & \omega_r \end{bmatrix} \begin{bmatrix} q_d^c - q_m \\ r_d^c - r_m \end{bmatrix} \tag{3.16}$$

Table 3.2 illustrates the bandwidth used in the two time-scale separation NDI controller. The bandwidth were obtained by trial and error until the performance FOM were met.

Table 3.2: Two-time separation NDI bandwidth for wind angles and body rates.

Variable	symbol	Value	Units
Angle-of-attack bandwidth	ω_α	10	rad/s
Angle-of-sideslip bandwidth	ω_β	10	rad/s
Yaw rate bandwidth	ω_r	40	rad/s
Pitch rate bandwidth	ω_q	40	rad/s
Roll rat bandwidth	ω_p	80	rad/s

3.4 Results: NDI Autopilot

Figures 3.10 to 3.14 present and compare two time-scale separation NDI with the gain-scheduled dual-controlled three-loop-autopilot respectively. Figure 3.10 compares acceleration response of the NDI and gain-scheduled controller for DAC missile. Although the responses are different in terms of transient dynamics; they both meet the performance specifications, eliminate the inherent tail-fin undershoot and the overshoot is significantly reduced on the NDI when compared to the gain-scheduled canard-only configuration.

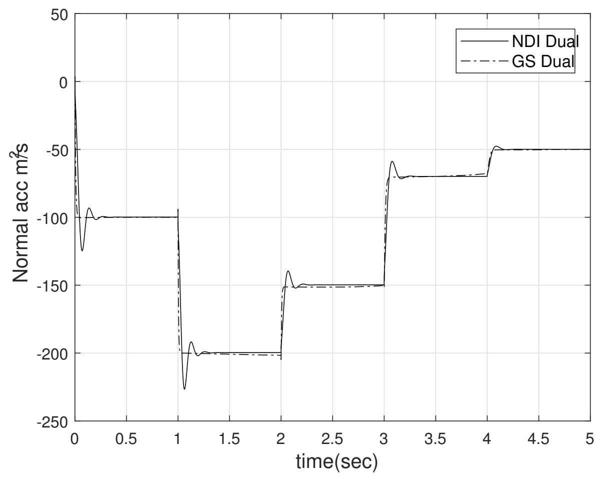

Figure 3.10: Comparison of DAC missile normal acceleration response to tracking normal acceleration with NDI and gain-scheduled three-loop autopilot.

Figure 3.11 illustrates the angle-of-attack response of the NDI controller which follows a different path from the gain-scheduled dual controller. It is clear that the angle-of-attack response of the NDI controller at each step input changes significantly. The NDI controller results in more body normal force contributing to the response due to the change in angle-of-attack.

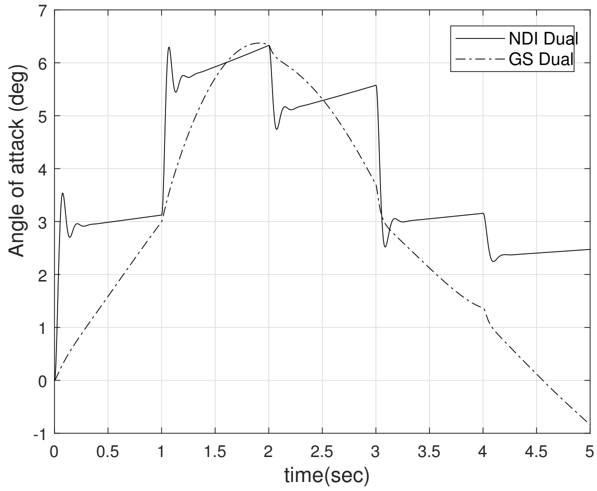

Figure 3.11: Comparison of DAC missile angle-of-attack response to tracking normal acceleration with an NDI and gain-scheduled three-loop autopilot.

Figure 3.12 compares the pitch response of the NDI with that of the gain-scheduled controller respectively. The large pitch rate of the NDI controller at each step change affirms that the normal load response generated by the missile is due to mostly the body lift resulting from the changing angle-of-attack. In contrast to the gain-scheduled pitch rate response which remains relatively desensitised to the acceleration command step variation.

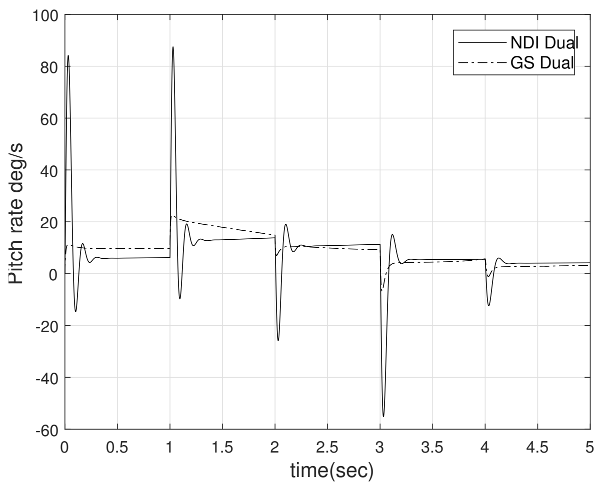

Figure 3.12: Comparison of DAC missile angle-of-attack response to tracking normal acceleration with an NDI and gain-scheduled three-loop autopilot.

Figures 3.13 and 3.14 illustrate the pitch deflection commands of the tail-fin and canard due to the NDI controller. The NDI deflection exhibits a diverted mode behaviour, however their magnitudes are significantly less than that of the gain-scheduled controller. It is thought from the results that a pitching moment that results in a dual-mode control can be achieved, even though the canard and the tail-fin deflections are of the same polarity. When comparing the NDI with the gain-scheduled controller the latter is highly likely to saturate actuators and degrade the DAC missile performance especially in the diverted mode.

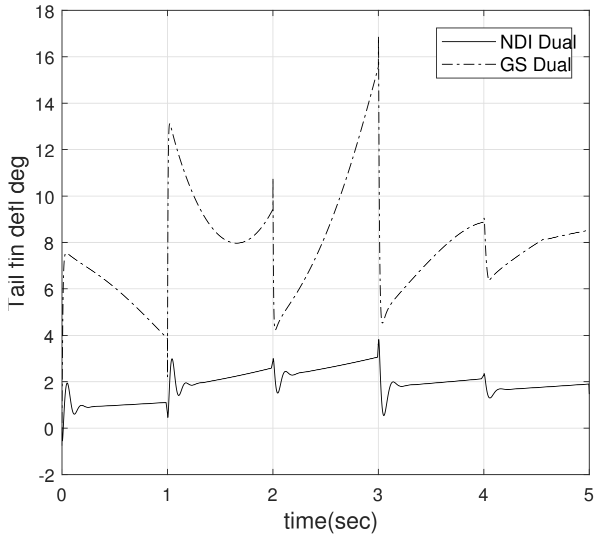

Figure 3.13: Comparison of DAC missile pitch tail-fin deflection commands from NDI and gain-scheduled three- loop autopilot.

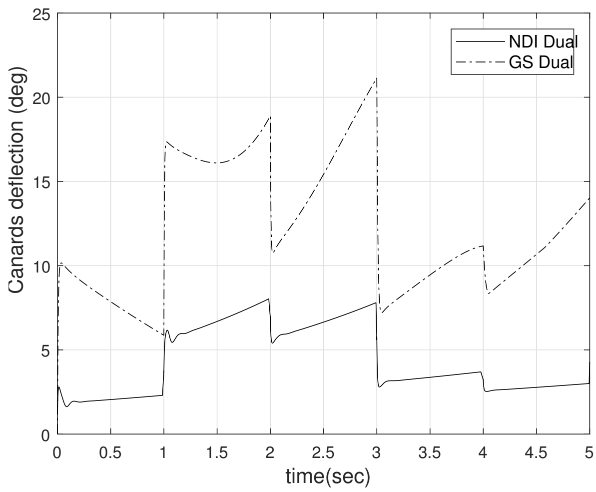

Figure 3.14: Comparison of DAC missile pitch canard deflection commands from NDI and gain-scheduled three-loop autopilot.

Chapter 4

Model Reference Adaptive Controller (MRAC)

A detailed design of an MRAC controller for a DAC missile is presented in this chapter. Adaptive control is capable of improving controller performance beyond the capabilities of convectional deterministic control techniques (Calise et al., 2001). Adaption aims to maintain desired system performance in the presence of uncertainty (parameter or system), system upset, failure or damage (Nguyen, 2012, Padhi et al., 2007).

Two fundamental approaches to adaptive control are: direct and indirect adaptions. Direct adaption determines the additional control signal to the baseline controller necessary to achieve better tracking performance (Hovakimyan et al., 2002, McFarland and Calise, 1997). Indirect adaption on the other hand estimates the control parameters necessary to generate a control signal that achieves desirable tracking performance (McFarland and Calise, 1997). Direct adaption has been the focus of most recent literature on adaptive control and it is the approach employed in this study (Sundararajan et al., 2003). Main components of a direct adaptive controller are: the baseline controller based on known plant properties, reference model, an adaptive element (uncertainty approximation function and gain update rule) and the uncertain plant to be controlled (Padhi et al., 2007). Adaptive control objective is to drive the plant to follow the reference model regardless of whether the uncertainty approximation has converged or not. Gain update rules are fundamental to the performance of an adaptive controller and Lyapunov stability theory is central to selecting suitable update rules (Balakrishnan et al., 2012).

Figure 4.1 illustrates the adaptive controller structure proposed in the current study. The adaptive controller introduces an additional feedback loop through the adaptive element. It is clear that the adaptive controller is added without modifying the baseline autopilot.

Furthermore, the adaption is done on the fast dynamics to ensure that the trim condition is achieved faster in the presence of uncertainty.

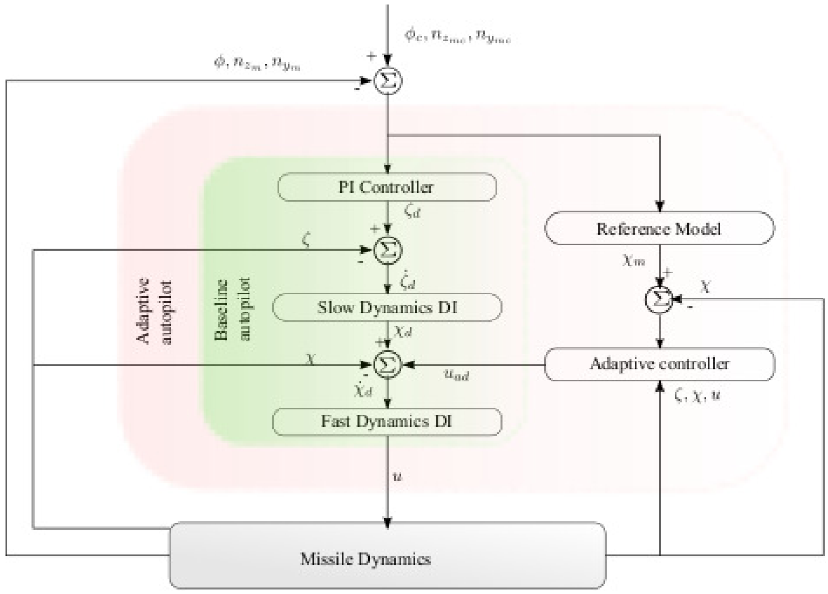

Figure 4.1: Missile adaptive controller schematic.

4.1 Adaptive Controller Synthesis

Plant uncertainty can be characterised as structured, unstructured, unmatched or unmodelled dynamics resulting from incorrect assumptions regarding the plant dynamics (Nguyen, 2018). The characteristics of the uncertainty to some extent influence the structure of the approximation function and the choice of the adaptive technique. Structured uncertainty have a known function structure and unknown parameters, unstructured uncertainty have unknown function structure and parameters and unmatched uncertainty may be structured or unstructured but cannot be eliminated completely by adaption (Matuvsuu et al., 2011).

Out of the four main components of the adaptive controller, major focus in the design process is channelled to the adaptive rule because it influences stability, tracking performance and robustness of the entire system. A poorly selected adaptive law will result in poor performance even if the baseline autopilot is perfect. The update rule/adaptive law defines how adaptive parameters should be adjusted to keep the tracking error as small as possible. The fundamental update rule is what is called the standard-MRAC adaptive law given by equation (4.1) (Nguyen, 2018):

$$\dot{k} = -\gamma\Phi(x)ePb \tag{4.1}$$

where k is the unknown approximation parameters/neural network weights, e is the error between plant response and reference model. $\Phi(x)$ is the basis function, P is a positively-definite matrix determined from Lyapunov equation, b is the control matrix of the reference model and γ is the learning rate. A high learning rate results in improved tracking performance but degrades the robustness of the system.

Equation (4.1) was historically derived using Lyapunov stability theory to guarantee asymptotic stability of the error dynamics between the reference model and the actual plant response. Although asymptotically stability of the tracking error is guaranteed, the standard-MRAC update rule is unable to adjust the bandwidth of the closed-loop system to guarantee robustness due to the unbounded adaption weights (Hovakimyan and Cao, 2010). Bounded adaption weights and tracking error are achieved by introducing a modification term in the standard MRAC. Equation (4.2) defines the structure of the modified MRAC adaptive rule (Balakrishnan et al., 2012):

$$\dot{k} = -\gamma\phi(x)ePb - \gamma\varsigma(x, P, b, A_m, e)k \tag{4.2}$$

where $\varsigma(x, P, b, A_m, e)$ is the learning rate damping term. Where A_m is the reference model state matrix.

The modification term results in an ultimately uniformly bounded stability condition. Modified MRAC adaptive rule achieves better robustness because the modification term limits the gain of the adaption loop and eliminates the integral action inherent in the standard MRAC (Hovakimyan and Cao, 2010).

Historically, the major challenge with adaption lies with the unbounded adaption weights that resulted in undesirable oscillation of the adaption signal (Cao and Hovakimyan, 2007a). Other issues such as large basis function amplitudes can also have the same effect. The problem of high amplitude on the adaption signal is addressed by normalising the modified adaptive rule (Nguyen et al., 2017). Equation (4.3) defines the normalised general modified adaptive law:

$$\dot{k} = \frac{-\gamma}{1 + \phi^T(x)R\phi(x)}(\phi(x)ePb + \varsigma(x, P, b, A_m, e)k) \tag{4.3}$$

where R is the normalisation weight matrix.

Another potential challenge with adaptive law application is persistent learning. Persistent learning results when high learning rates are maintained after adaption has achieved the control objective (Nguyen et al., 2011). Persistent learning has the potential of reducing the robustness of the controller over time. The effect of persistent learning is circumvented by introducing a co-variance adjustable learning rate. Equation (4.4) illustrates the co-variance adjustment learning rate with forget factor.

$$\dot{\gamma} = \iota\gamma(t) - \eta\gamma(t)\Phi(x)\Phi^T(x)\gamma(t) \tag{4.4}$$

where η is the co-variance adjustment parameter and ι is a forget factor.

The adaptive control synthesis process in this chapter was divided into baseline controller implementation which is based on the NDI controller from chapter (3), implementation of the adaptive controller, neural network structure selection and the stability proof of the tracking error dynamics.

4.1.1 Reference Baseline Controller

4.1.1.1 Reference DAC Model

DAC missile utilises both canards and tail-fins to steer the missile in pitch and yaw, while the roll control is primarily handled with the tail-fins only. Equation (4.5) defines the dynamics of the missile in state-space format with some uncertainty. For simplicity, variation in airspeed are neglected without loss of generality in the missile dynamics.

$$\dot{\chi} = A_{11}\chi + A_{12}\zeta + B_1 u + f_1(\chi,\zeta,u) \tag{4.5a}$$

$$\dot{\zeta} = A_{21}\zeta + A_{22}\chi + B_2 u + f_2(\chi,\zeta,u) \tag{4.5b}$$

where $\chi = \begin{bmatrix} p & q & r \end{bmatrix}^T$ defines the body angular velocity vector, $\zeta = \begin{bmatrix} \alpha & \beta \end{bmatrix}^T$ defines the wind angles, $f(\chi,\zeta,u)$ defines the unmatched uncertainty of the plant to be accounted for using adaption, $B_1 = B(1:5,1:3)$, $B_2 = B(1:5,4:5)$, $A_{11} = A(1:3,1:3)$, $A_{12} = A(1:3,4:5)$, $A_{21} = A(4:5,1:3)$ and $A_{22} = A(4:5,4:5)$. The control vector u, control matrix B, and the state matrix A are defined as follows:

$$u = \begin{bmatrix} \delta_p & \delta_q^t & \delta_q^c & \delta_r^t & \delta_r^c \end{bmatrix}^T \tag{4.6a}$$

$$B = \begin{bmatrix} Q_{I_{xx}} C_{l_{\delta_p}} & 0 & 0 & 0 & 0 \\ 0 & Q_{I_{yy}} C_{m_{\delta_q^t}} & Q_{I_{yy}} C_{m_{\delta_q^c}} & 0 & 0 \\ 0 & 0 & 0 & Q_{I_{yy}} C_{n_{\delta_r^t}} & Q_{I_{yy}} C_{n_{\delta_r^c}} \\ 0 & Q_m C_{N_{\delta_q^t}} & Q_m C_{N_{\delta_q^c}} & 0 & 0 \\ 0 & 0 & 0 & Q_m C_{S_{\delta_q^r}} & Q_m C_{S_{\delta_r^c}} \end{bmatrix} \tag{4.6b}$$

$$A = \begin{bmatrix} Q_{I_{xx}} C_{l_p} & 0 & 0 & 0 & 0 \\ 0 & Q_{I_{yy}} C_{m_q} & 0 & Q_{I_{yy}} C_{m_\alpha} & 0 \\ 0 & 0 & Q_{I_{yy}} C_{n_r} & 0 & Q_{I_{yy}} C_{n_\beta} \\ 0 & Q_m C_{N_q} & 0 & Q_m C_{N_\alpha} & 0 \\ 0 & 0 & Q_m C_{S_r} & 0 & Q_m C_{S_\beta} \end{bmatrix} \tag{4.6c}$$

where $Q_m = 0.5\rho U/m$, $Q_{I_{xx}} = 0.5\rho U^2 d/I_{xx}$, $Q_{I_{yy}} = 0.5\rho U^2 d/I_{yy}$, U is the trim airspeed and ρ is the air density.

Table 4.1 illustrates the system parameters of the state-space model of DAC missile given by equation 4.5.where C_{l_p} is the roll damping coefficient, $C_{l_{\delta_p}}$ is the roll moment tail-fin coefficient, $C_{m_{\delta_q^t}}, C_{n_{\delta_r^t}}$ are the yaw and pitch moment tail-fin coefficients, C_{m_q}, C_{n_r} are the pitch and yaw damping moment coefficients, $C_{m_{\delta_q^c}}, C_{n_{\delta_r^c}}$ are the yaw and pitch moment canard coefficients, $C_{m_\alpha}, C_{n_\beta}$ are the pitch and yaw moment slopes, C_{N_q}, C_{S_r} are the normal and side force dynamic coefficients, $C_{N_\alpha}, C_{S_\beta}$ are the normal and side force slopes, $C_{N_{\delta_q^t}}, C_{S_{\delta_q^t}}$ are the normal and side force tail-fin coefficients, $C_{N_{\delta_q^c}}, -C_{S_{\delta_r^c}}$ are the normal and side force canard coefficients.

Table 4.1: System parameters.

Parameter	Values	Parameter	Values
C_{l_p}	-0.012	$C_{m_{\delta_q^t}}, C_{n_{\delta_r^t}}$	-28.72
$C_{m_q}, -C_{n_r}$	$1.29e-05$	$C_{m_{\delta_q^c}}, C_{n_{\delta_r^c}}$	25.54
C_{N_q}, C_{S_r}	$3.98e-07$	$C_{N_{\delta_q^t}}, -C_{S_{\delta_q^r}}$	3.76
$C_{N_\alpha}, C_{S_\beta}$	11.57	$C_{N_{\delta_q^c}}, -C_{S_{\delta_r^c}}$	4.00
$C_{m_\alpha}, -C_{n_\beta}$	7.87	$C_{l_{\delta_p}}$	7.02

Two time-scale separation dynamic inversion (DI) splits the missile dynamics into fast and slow dynamics to allow for application of DI on a non-minimum phase plant. The controller consists of two DI controllers (slow and fast) and outer acceleration and roll angle loops closed with a PI controllers to augment robustness. The slow dynamics consist of the wind angle rates while the fast dynamics consist of body angular velocities. The proposed baseline topology is a skid-to-turn autopilot consisting of five PI controllers, two for canard and tail-fin yaw control, two for pitch control and one for roll angle control. Figure 4.2 illustrates the baseline control structure:

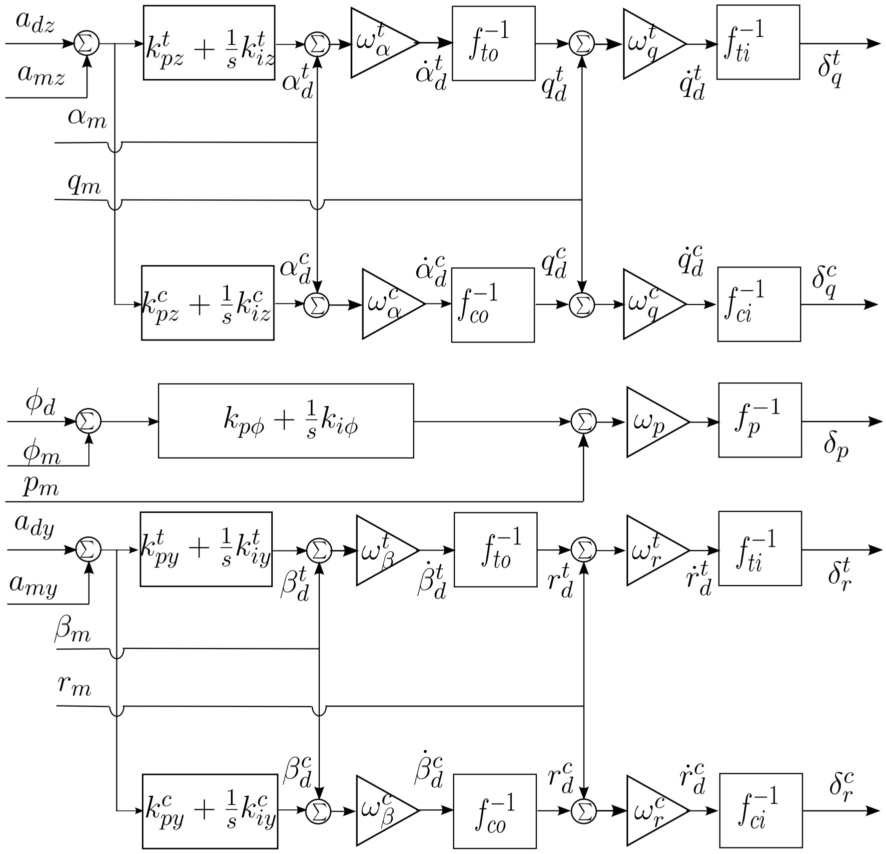

Figure 4.2: Baseline controller architecture.

4.1.1.2 Slow Dynamics DI

The slow dynamics DI controller is determined by inverting Eq. (4.5)b. The effects of control surface deflections are neglected on the slow dynamics to simplify the inversion. Equation (4.7) illustrates the inversion of the slow dynamics. The DI controller is set up such that the canard and tail-fin effects on the desired attitude dynamics χ_d are treated separately to eliminate actuator coupling effects.

$$\begin{bmatrix} \chi^t_d \\ \chi^c_d \end{bmatrix} = \begin{bmatrix} 1 & 0 & 0 \\ 0 & A^{-1}_{22} & 0 \\ 0 & 0 & A^{-1}_{22} \end{bmatrix} \begin{bmatrix} 1 & 0 & 0 \\ 0 & A_{21} & 0 \\ 0 & 0 & A_{21} \end{bmatrix} \begin{bmatrix} \dot{p}_d \\ \dot{\zeta}^t_d \\ \dot{\zeta}^c_d \end{bmatrix} \tag{4.7}$$

where χ^t_d is the desired attitude vector for tail-fin, χ^c_d is the desired attitude vector for canard controller, ζ^t_d is the desired wind angle vector for tail-fin controller, ζ^c_d is the desired wind angle vector for canard controller.

The desired wind angle rates are defined with a first-order plant with bandwidth Ω_ζ:

$$\begin{bmatrix} \dot{p}_d \\ \dot{\zeta}_d^t \\ \dot{\zeta}_d^c \end{bmatrix} = \Omega_\zeta \begin{bmatrix} p_d \\ \zeta_d^t - \zeta^t \\ \zeta_d^c - \zeta^c \end{bmatrix} \tag{4.8}$$

Ω_ζ is a diagonal matrix defined as follows:

$$\Omega_\zeta = diag(1, \omega_\alpha^t, \omega_\beta^t, \omega_\alpha^c, \omega_\beta^c)$$

The desired wind angle vectors ζ_d^t and ζ_d^c are determined from a PI controller of the normal and lateral load factors as defined by equation (4.9) below:

$$\begin{bmatrix} p_d \\ \zeta_d^t \\ \zeta_d^c \end{bmatrix} = \left(K_p + \frac{1}{s} K_i\right) e_a \tag{4.9}$$

where $e_a = \begin{bmatrix} e_\phi & e_z & e_y & e_z & e_y \end{bmatrix}^T$, e_ϕ is the roll angle error, e_y is the lateral acceleration error and e_z is the normal acceleration error. K_p and K_i are the PI proportional and integral gains defined by the following diagonal matrices:

$$K_p = diag(k_{p_\phi}, k_{p_z}^t, k_{p_y}^t, k_{pz}^c, k_{p_y}^c)$$
$$K_i = diag(k_{i_\phi}, k_{i_z}^t, k_{i_y}^t, k_{iz}^c, k_{i_y}^c)$$

4.1.1.3 Fast Dynamics DI

The fast dynamics DI controller is obtained by inverting Eq. (4.5)a to determine the desired actuator commands. Inversion is performed separately for canard and tail-fin command using equation 4.10 and 4.12:

$$u^t = B^{t^{-1}} \left(\dot{\chi}_d^t - A_{11}\chi - A_{12}\zeta\right) \tag{4.10}$$

where $B^t = diag(1, B_{22}, B_{34})$.

The desired tail-fin control angular acceleration were selected to be a first-order system defined as follows:

$$\dot{\chi}_d^t = \Omega_\chi^t (\chi_d^t - \chi^t) \tag{4.11}$$

where $\Omega_\chi^t = diag(\omega_p, \omega_q, \omega_r)$ defines the tail-fin fast dynamics reference model bandwidth. The canard deflection are determined as follows:

$$u^c = B^{c^{-1}} (\dot{\chi}_d^c - A_{11}\chi - A_{12}\zeta) \tag{4.12}$$

where $B^c = diag(0, B_{23}, B_{35})$.

The desired canard-control angular acceleration were selected to be a first-order system defined as follows:

$$\dot{\chi}_d^c = \Omega_\chi^c(\chi_d^c - \chi) \tag{4.13}$$

where $\Omega_\chi^c = diag(\omega_q, \omega_r)$ defines the canard fast dynamics reference model bandwidth.

Consolidating the above expressions and Eqs. (4.7) to (4.10) yields Eq. (4.14) which defines the reference model of the body angular velocities:

$$\begin{aligned}\begin{bmatrix}\dot{\chi}_m^t \\ \dot{\chi}_m^c\end{bmatrix} = &- \begin{bmatrix}\Omega_\chi^t & 0 \\ 0 & \Omega_\chi^c\end{bmatrix}\begin{bmatrix}\chi_m^t \\ \chi_m^c\end{bmatrix} - \\ &\begin{bmatrix}\Omega_\chi^t A_{21}^{-1}(\Omega_\zeta^t + A_{22}) & 0 \\ 0 & \Omega_\chi^c A_{21}^{-1}(\Omega_\zeta^c + A_{22})\end{bmatrix}\begin{bmatrix}p_m \\ \zeta_m^t \\ \zeta_m^c\end{bmatrix} \\ &+ \begin{bmatrix}\Omega_\chi^t A_{21}^{t-1}\Omega_\zeta^t & 0 \\ 0 & \Omega_\chi^c A_{21}^{c-1}\Omega_{zeta}^c\end{bmatrix}\begin{bmatrix}\phi_d \\ \zeta_d^t \\ \zeta_d^c\end{bmatrix}\end{aligned} \tag{4.14}$$

where χ_m^t, ζ_m^t are the reference model tail body rates vector and wind angles vector and χ_m^c, ζ_m^c are the reference model canard body rates vector and wind angles vector.

4.1.2 Adaptive Controller

The main purpose of the adaptive controller is to drive the error between the closed-loop plant response and the reference model to zero while maintaining the plant within acceptable stability margins. Closed-loop actuator commands are determined as follows:

$$\begin{aligned}u = \begin{bmatrix}B^{t-1} & 0 \\ 0 & B^{c-1}\end{bmatrix}\Bigg(&- \begin{bmatrix}A_{11}^t + \Omega_\chi^t & 0 \\ 0 & A_{11}^c + \Omega_\chi^c\end{bmatrix}\begin{bmatrix}\chi_m^t \\ \chi_m^c\end{bmatrix} \\ &- \begin{bmatrix}A_{12}^t + \Omega_\chi^t A_{21}^{-1}(\Omega_\zeta^t + A_{22}) \\ A_{12}^c + \Omega_\chi^c A_{21}^{-1}(\Omega_\zeta^c + A_{22})\end{bmatrix}\zeta_m \\ &+ \Omega_\chi A_{21}^{-1}\Omega_z\left(K_p + \frac{K_i}{s}\right)e_a - \bar{f}(\chi, \zeta, u)\Bigg)\end{aligned} \tag{4.15}$$

Substituting Eq. (4.15) into Eq. (4.5)a yields Eq. (4.16) as the closed-loop response dynamics of the plant. It is worth noting that the substitution is done separately for canard and tail-fin control inputs.

$$\begin{aligned}\begin{bmatrix}\dot{\chi}^t \\ \dot{\chi}^c\end{bmatrix} &= -\begin{bmatrix}\Omega^t_\chi & 0 \\ 0 & \Omega^c_\chi\end{bmatrix}\begin{bmatrix}\chi^t \\ \chi^c\end{bmatrix} \\ &- \begin{bmatrix}\Omega^t_\chi A_{21}^{-1}(\Omega^t_\zeta + A_{22}) & 0 \\ 0 & \Omega^c_\chi A_{21}^{-1}(\Omega^c_\zeta + A_{22})\end{bmatrix}\begin{bmatrix}p_d \\ \zeta^t \\ \zeta^c\end{bmatrix} \\ &+ \begin{bmatrix}\Omega^t_\chi A_{21}^{t-1}\Omega^t_\zeta & 0 \\ 0 & \Omega^c_\chi A_{21}^{c-1}\Omega^c_{zeta}\end{bmatrix}\begin{bmatrix}p_d \\ \zeta^t_d \\ \zeta^c_d\end{bmatrix} + B_I\tilde{f}_1(\chi,\zeta,u)\end{aligned} \tag{4.16}$$

Where $\bar{f}_1(\chi,\zeta,u)$ is the estimated unmatched uncertainty function, B_I is an identity matrix and $\tilde{f}_1(\chi,\zeta,u)$ is the difference between estimated and actual uncertainty.

The tracking error e between the reference model (Eq. (4.14)) and plant closed-loop response (Eq. (4.16)) is given as follows:

$$\dot{e} = A_m e + B_I\tilde{f}(\chi,\zeta,u) \tag{4.17}$$

where, $A_m = -\begin{bmatrix}\Omega^t_\chi & 0 \\ 0 & \Omega^c_\chi\end{bmatrix}$, $e = \begin{bmatrix}\chi^c_m - \chi & \chi^t_m - \chi\end{bmatrix}$, χ is the measured body rate.

4.1.2.1 Neural Network

Neural networks are the preferred uncertainty approximation technique in the current study because of their renowned ability to approximate any function. A feedforward radial basis function single hidden layer is selected over other networks because of easy design, good generalisation, strong tolerance to input noise, and online learning ability (Yu et al., 2011). Equation (4.18) defines the approximation function of the neural network:

$$f = \Theta^T\Phi(W^T\bar{x}) \tag{4.18}$$

where the hidden layer weights are given by $W^T = \begin{bmatrix}W_0 & W_x\end{bmatrix} \in \mathbb{R}^{m\times(n+1)}$, the output layer weights are given by $\Theta^T = \begin{bmatrix}V_0 & V^T\end{bmatrix} \in \mathbb{R}^{n\times(m+1)}$, $\bar{x} = \begin{bmatrix}1 & x^T\end{bmatrix}^T \in \mathbb{R}^{n+1}$, $\Phi(W^T\bar{x}) = \begin{bmatrix}1 & \sigma'(W^T\bar{x})\end{bmatrix} \in \mathbb{R}^{m+1}$, $x = \begin{bmatrix}\chi^T & \zeta^T & u^T\end{bmatrix}^T$ and the activation function $\sigma(W^T\bar{x})$ is Gaussian. W_0 is the hidden layer bias weights matrix, W_x is the hidden layer weight matrix, V_0 is the output layer bias weight matrix, V is the output layer weights matrix and Φ is the basis function of the neural network.

Substituting Eq. (4.18) into error Eq. (4.17) yields:

$$\dot{e} = A_m e + B_I \Theta^T \Phi(W^T \bar{x}) - B_I {\Theta^*}^T \Phi({W^*}^T \bar{x}) \tag{4.19}$$

where Θ^* and W^* are the ideal neural network gain matrices; Θ and W are the estimated gain matrices.

The nonlinear third term of the error dynamics is approximated using first-order Taylor series expansion with respect to ${W^*}^T \bar{x}$ about the estimated term $W^T \bar{x}$ to yield the following error dynamics given as follows:

$$\dot{e} = A_m e + B_I \tilde{\Theta}^T \Phi(W^T \bar{x}) + B_I V^T \sigma'(W^T \bar{x}) \tilde{W} \bar{x} + B_I \delta \tag{4.20}$$

where $\tilde{\Theta} = \Theta^* - \Theta, \tilde{W} = W^* - W$ and δ is the uncertainty due to high order terms.

4.1.2.2 Adaptive Rules

The following modified adaptive rules are the subject of study for application of MRAC with neural networks: $\sigma-$ modification, $\epsilon-$ modification, adaptive loop recovery and optimal control modification. The robust update rules guarantee ultimately uniformly bounded tracking error and basis function weights. $\sigma-$ modification adds a constant learning damping to the update rule and it is the simplest modification rule (Nguyen, 2018). $\epsilon-$ modification introduces an error dependent learning damping-ratio with a goal of recovering the asymptotic stability of the standard MRAC rule (Rohrs et al., 1985). Adaptive loop recovery has a damping-ratio that seeks to minimise nonlinearities in the feedback loop and maintain the stability margins of the reference model (Calise and Yucelen, 2012). Optimal control modification introduces an L_2-norm optimised damping effect to the update rule that ensures optimal bounded tracking error and basis function weights (Nguyen et al., 2008). Table 4.2 illustrates the modified adaptive rules discussed above.

Table 4.2: Modified adaptive rules.

Adaptive rule	
$\sigma-$ Mod	$\dot{\Theta} = -\Gamma\left(\Phi(\bar{x}) e^T PB + \sigma\Theta\right)$
$\epsilon-$Mod	$\dot{\Theta} = -\Gamma\left(\Phi(\bar{x}) e^T PB + \mu \left\| e^T PB \right\| \Theta\right)$
L_2 Mod (OCM)	$\dot{\Theta} = -\Gamma\Phi(\bar{x})\left(e^T PB - \nu\Phi^T(\bar{x})\Theta B^T P A_m^{-1} B\right)$
ALR Mod	$\dot{\Theta} = -\Gamma(\Phi(\bar{x}) e^T PB + \eta\Phi_{\bar{x}}(\bar{x})\Phi_{\bar{x}}^T(\bar{x})\Theta)$

Since a single hidden layer neural network is used, a hidden layer update rule is necessary and for all cases in this study the hidden layer weights are updated with a $\sigma-$ modification rule. A normalised optimal control modification with normalised co-variance adjustment will be considered with the aim of eliminating effects of large basis-function amplitudes on the adaption rate. Equation (4.21) is the normalised OCM update rule for the neural network output weights and Eq. (4.22) is the normalised co-variance adjustment update rule for the output weights learning rate:

$$\dot{\Theta} = \frac{-\Gamma_\Theta \Phi(W^T\bar{x})}{1+\Phi^T(W^T\bar{x})R\Phi(W^T\bar{x})}\left[e^T P - \nu\Phi^T(W^T\bar{x})\Theta B^T P A_m^{-1}\right]B \tag{4.21}$$

$$\dot{\Gamma}_\Theta = \frac{\eta\Gamma_\Theta \Phi(W^T\bar{x})\Phi^T(W^T\bar{x})\Gamma_\Theta}{1+\Phi^T(W^T\bar{x})R\Phi(W^T\bar{x})} \tag{4.22}$$

Equation (4.23) is the sigma modification update rule used for the hidden layer gains.

$$\dot{W} = -\Gamma_W \bar{x} e^T PBV^T\sigma'(W^T\bar{x}) + \sigma_w W \tag{4.23}$$

$$PA_m + A_m^T P = -Q$$

where P and Q are a positively definete matrices, Γ_W is the learning rate for W gain matrix, Γ_Θ is the learning rate for Θ, ν is the optimal modification learning damping ratio, σ_W is the learning damping ratio for the $\sigma-$modification update rule, R is the normalisation weight matrix and η is the co-variance adjustment parameter.

4.2 Stability Proof

The proof of stability of the adaptive controller is carried-out using Lyapunov direct method. This section details the stability of the MRAC controller with normalised co-variance adjustment optimal control modification. The other adaptive rule stability proof have been presented in the literature and will not be repeated here.

The stability of the normalised OCM with co-variance adjustment and $\sigma-$ modification for single hidden layer neural network is presented by the following theorem. The theorem and the stability proof are an extension of results derived in reference (Nguyen et al., 2017), for separate case of normalised OCM and co-variance adjustment OCM.

Theorem 1. *The normalised optimal control modification update rule with co-variance adjustment (Eq. (4.21) and (4.22)) and $\sigma-$modification (Eq. (4.23)) are stable for single hidden layer neural network and resulting in uniformly ultimately bounded tracking error for $0 < \nu < \nu_{max}$, $0 < \eta < \nu\lambda_{min}(B^T A_m^{-T} Q A_m^{-1} B)$ and $0 < R < R_{max}$ such that $\nu c_1 c_2 c_7 - c_8^2 > 0$ where $c_1 = \lambda_{min}(Q)$, $c_2 = \|PB\| \|\delta_0\| / \lambda_{min}(Q)$ and $c_7 = 1 + \lambda_{min}(R)\Phi_0^2$ (Nguyen et al., 2017).*

Proof. Choose a Lyapunov candidate $\mathcal{V}$ function Eq. (4.24)

$$\begin{aligned}\mathcal{V}(e,\tilde{\Theta},\tilde{W}) &= e^T P e + trace(\tilde{\Theta}\Gamma_{\tilde{\Theta}}^{-1}\tilde{\Theta}) \\ &\quad + trace(\tilde{W}\Gamma_{\tilde{W}}^{-1}\tilde{W})\end{aligned} \tag{4.24}$$

Evaluating $\dot{\mathcal{V}}$ and substituting Eqs. (4.20), (4.23),(4.21), (4.22) and using the following definition yield Eq. (4.25)

$$\frac{d\Gamma_{\Theta}^{-1}}{dt} = -\Gamma_{\Theta}^{-1}\dot{\Gamma}_{\Theta}\Gamma_{\Theta}^{-1} = \frac{\eta\Phi(W^T\bar{x})\Phi^T(W^T\bar{x})}{1+\Phi^T(W^T\bar{x})R\Phi(W^T\bar{x})}$$

$$trace(A^T B) = BA^T$$

$$\begin{aligned}\dot{\mathcal{V}}(e,\tilde{\Theta},\tilde{W}) &= -e^T Q e + 2e^T PB\delta \\ &\quad + \frac{2e^T PB\tilde{\Theta}^T\Phi(W^T\bar{x})\Phi^T(W^T\bar{x})R\Phi(W^T\bar{x})}{1+\Phi^T(W^T\bar{x})R\Phi(W^T\bar{x})} \\ &\quad + \frac{2\nu\Phi^T(W^T\bar{x})\Theta^* B^T P A_m^{-1} B\tilde{\Theta}^T\Phi(W^T\bar{x})}{1+\Phi^T(W^T\bar{x})R\Phi(W^T\bar{x})} \\ &\quad - \frac{\nu\Phi^T(W^T\bar{x})\tilde{\Theta}B^T A_m^{-T} Q A_m^{-1} B\tilde{\Theta}\Phi(W^T\bar{x})}{1+\Phi^T(W^T\bar{x})R\Phi(W^T\bar{x})} \\ &\quad + \frac{\eta\Phi^T(W^T\bar{x})\tilde{\Theta}\tilde{\Theta}^T\Phi(W^T\bar{x})}{1+\Phi^T(W^T\bar{x})R\Phi(W^T\bar{x})} \\ &\quad - 2\sigma_w\tilde{W}\tilde{W}^T + 2\sigma_w W^*\tilde{W}^T\end{aligned} \tag{4.25}$$

$\dot{\mathcal{V}}$ is bounded by

$$\begin{aligned}\dot{\mathcal{V}} &\le -c_1\left(\left(\|e\| - c_2\right)^2 - c_2^2\right) + \frac{2c_8}{c_7}\|e\|\left\|\tilde{\Theta}\right\| \\ &\quad - \frac{\nu c_3}{c_7}\left(\left(\left\|\tilde{\Theta}\right\| - c_4\right)^2 - c_4^2\right) \\ &\quad - 2\sigma_w\left(\left(\left\|\tilde{W}\right\| - \frac{W_0}{2}\right)^2 - \frac{W_0}{2}\right)^2\right)\end{aligned} \tag{4.26}$$

where $c_1 = \lambda_{min}(Q)$, $c_2 = \|PB\| \|\delta_0\| / \lambda_{min}(Q)$, $c_3 = (\lambda_{min}(B^T A_m^{-T} Q A_m^{-1} B) - \eta/\nu)\Phi_0^2$, $c_4 = \left\|B^T P A_m^{-1} B\right\| \Theta_0 / c_3$, $c_7 = 1 + \lambda_{min}(R)\Phi_0^2$, $c_8 = \|PB\| \lambda_{max}(R)\Phi_0^3$, $\left\|\Phi(W^T\bar{x})\right\| \le \Phi_0$, $\delta_0 = \delta$, $\Theta_0 = \|\Theta^*\|$ and $W_0 = \|W^*\|$

The values of $\|e\|$, $\|W\|$ and $\|\Theta\|$ that maximise $\dot{\mathcal{V}}$ are determined by evaluating the partial derivative of $\dot{\mathcal{V}}$ with respect to $\|e\|$, $\|W\|$ and $\|\Theta\|$:

$$\frac{\partial \dot{\mathcal{V}}}{\partial \|e\|} \leq -2c_1(\|e\| - c_2) + 2\frac{\nu c_8}{c_7}\left\|\tilde{\Theta}\right\| = 0 \tag{4.27a}$$

$$\frac{\partial \dot{\mathcal{V}}}{\partial \left\|\tilde{\Theta}\right\|} \leq \frac{2\nu c_3}{c_7}(\|\Theta\| - c_4) + 2\frac{\nu c_8}{c_7}\|e\| = 0 \tag{4.27b}$$

$$\frac{\partial \dot{\mathcal{V}}}{\partial \left\|\tilde{W}\right\|} \leq -2\sigma_w(\|W\| - \frac{W_0}{2}) = 0 \tag{4.27c}$$

Solving for the value of $\|e\|$, $\|W\|$ and $\|\Theta\|$ that maximise $\dot{\mathcal{V}}$ yields the following:

$$\|e\| = \epsilon = \frac{\nu c_3(c_4c_8 + c_1c_2c_7)}{\nu c_1c_3c_7 - c_8^2}, \left\|\tilde{\Theta}\right\| = \kappa = \frac{c_1c_7(c_2c_8 + \nu c_3c_4)}{\nu c_1c_2c_7 - c_8^2}, \left\|\tilde{W}\right\| = \xi = \frac{W_0}{2}$$

The minimum bounds of $\|e\|$, $\|W\|$ and $\|\Theta\|$ are given by Eq. (4.28):

$$\|e\| \geq \epsilon\left[1 + \sqrt{1 + \frac{\nu(c_3c_4^2 + 2\sigma_w\xi^2)\sigma_1}{\nu c_3(c_4c_8 + c_1c_2c_7)^2}}\right] \tag{4.28a}$$

$$\left\|\tilde{\Theta}\right\| \geq \kappa\left[1 + \sqrt{1 + \frac{(c_1c_2^2 + 2\sigma_w\xi^2)\sigma_1}{c_1(c_8c_2 + \nu c_3c_4)^2}}\right] \tag{4.28b}$$

$$\left\|\tilde{W}\right\| \geq \xi + \sqrt{2\sigma_w\xi + c_1c_2\epsilon + \frac{\nu c_3c_4}{c_7}\kappa + \frac{\nu c_1c_2c_3c_4c_8}{\sigma_1}} \tag{4.28c}$$

provided that $0 < R < R_{max}$, $0 < \eta < \eta_{max}$ and $0 < \nu < \nu_{max}$ such that $\sigma_1 = \nu c_1c_2c_7 - c_8^2 > 0$ resulting in the following upper bound for the basis function norm:

$$\Phi_0^2 < \frac{\nu\lambda_{min}(Q)(\lambda_{min}(B^TA_m^{-T}QA_m^{-1}B) - \frac{\eta}{\nu})\lambda_{min}(R)}{2\|PB\|^2\lambda_{max}^2(R)}\left[1 + \sqrt{1 + \frac{4\|PB\|^2\lambda_{max}^2(R)}{\nu\lambda_{min}(Q)(\lambda_{min}(B^TA_m^{-T}QA_m^{-1}B) - \frac{\eta}{\nu})\lambda_{min}^2(R)}}\right] \tag{4.29}$$

Hence, $\dot{\mathcal{V}}(e,\tilde{\Theta},\tilde{W}) \leq 0$ outside the compact set:

$$B_\delta = \left\{\left(e,\tilde{\Theta},\tilde{W}\right) \in \mathbb{R}^n \times \mathbb{R}^{m\times p} \times \mathbb{R}^{k\times l} : c_1\left(\|e\| - c_2\right)^2 \frac{2c_8}{c7}\|e\|\left\|\tilde{\Theta}\right\| + \frac{\nu c_3}{c_7}\left(\left\|\tilde{\Theta}\right\| - c_4\right)^2 + 2\sigma_w\left(\left\|\tilde{W}\right\| - \frac{W_0}{2}\right)^2 \leq c_1c_2^2 + \frac{\nu c_3}{c_7}c_4^2 + 2\sigma_w\left(\frac{W_0}{2}\right)^2\right\} \tag{4.30}$$

Therefore the closed-loop system is ultimately uniformly bounded for $0 < R < R_{max}$, $0 < \eta < \nu\lambda_{min}(B^TA_m^{-1}B)$ and $0 < \nu < \nu_{max}$

4.3 MRAC Controller Simulation Results

Flight simulation of a DAC missile with robust adaptive control was conducted using Matlab- Simulink platform. The following robust adaptive controllers were studied, $\sigma-$ mod, $\epsilon-$ mod, ALR, OCM and normalised OCM with co-variance adjustment. All the adaptive controllers used a single hidden layer RBFNN for uncertainty estimation and the hidden layer weights for all adaptive controllers were updated using $\sigma-$ modification update rule. The same baseline controller was employed for all adaptive controllers. The adaptive controller responses are compared to the reference model and baseline controller. The reference model is based on the desired state matrix A_m constructed with the desired bandwidths for the fast and slow dynamics. The following desired bandwidths were used in this study: $\omega_p = 80\ rad/s$, $\omega_q^t = \omega_r^t = \omega_q^c = \omega_r^c = 40\ rad/s$ $\omega_\phi = 20\ rad/s$ and $\omega_\alpha^t = \omega_\beta^t = \omega_\alpha^c = \omega_\beta^c = 10\ rad/s$. The fast dynamics bandwidths are quadruple that of the slow dynamics to reduce interference between the two control loops. Baseline controller is a two time-scale separation DI controller with normal and lateral accelerations and roll angle PI controllers to augment robustness. The PI controllers were tuned with an LTI plant linearised about the point $\alpha = 0$ for both tail-fin and canard control PI. Table 4.3 illustrates the PI gain used with the baseline DI controller.

Table 4.3: Baseline PI controller gains.

Channel	Type	K_p	K_i
Normal Acc tail	PI	0.0018	0.0275
Normal Acc canards	PI	0.0025	0.0297
Lateral Acc tail	PI	0.0018	0.0275
Lateral Acc Canard	PI	0.0025	0.0297
Roll angle	PI	3.2875	3.1292

Uncertainty approximation was implemented using a feedforward single-hidden-layer RBFNN. The inputs to the feedforward neural network are wind angles, body angle rates, air speed, tail-fin and canard deflections. The output of the neural network are $u_{ad} = \begin{bmatrix} \dot{p}_{ad}^t & \dot{q}_{ad}^t & \dot{r}_{ad}^t & \dot{q}_{ad}^c & \dot{r}_{ad}^c \end{bmatrix}^T$. Adaption of uncertainty is done on the commands for the fast dynamics while the performance of the slow dynamics are accounted only for by the PI controller. Adaption on the fast dynamics is preferred over adaption of the slow dynamics because variation in deflections of both tail-fins and canards have high and quick effect on fast dynamics, hence adaption of this dynamics will allow the control to achieve trim condition faster in the presence of extraneous or non-extraneous uncertainties.

The results section is divided into three subsections: subsection 4.3.1 details the adaptive control of canard, tail-fin and DAC missile and contrasts it with the baseline controller performance. Subsection 4.3.2 presents the 6-DoF responses of a DAC missile for different adaptive controllers respectively. Subsection 4.3.3 details the results of normalised OCM with co-variance adjustment adaptive controller for DAC missile.

4.3.1 Adaptive Control for Different Missile Configuration.

Figures 4.3 to 4.7 present the responses of tail-fin-only, canard-only and DAC missile with the baseline autopilot and OCM autopilot. Due to lack of roll authority for canard-only configuration, only the longitudinal dynamics are compared. A learning rate of $\Gamma_\Theta = \Gamma_W = 50000$ and damping factor of $\nu = \sigma_W = 0.3$ were used for the hidden layer and the output layer.

Figures 4.3a and 4.3b compare the normal acceleration response of the three control configurations. It is clear from the responses that the adaptive autopilot results in better transient dynamics. Although the adaptive autopilot shows improved transient dynamics it results in a larger steady-state error. The steady-state error is consequence of the unmatched uncertainty. The adaptive controller eliminates the oscillation on the canard-only response, however a large sluggish overshoot is observed.

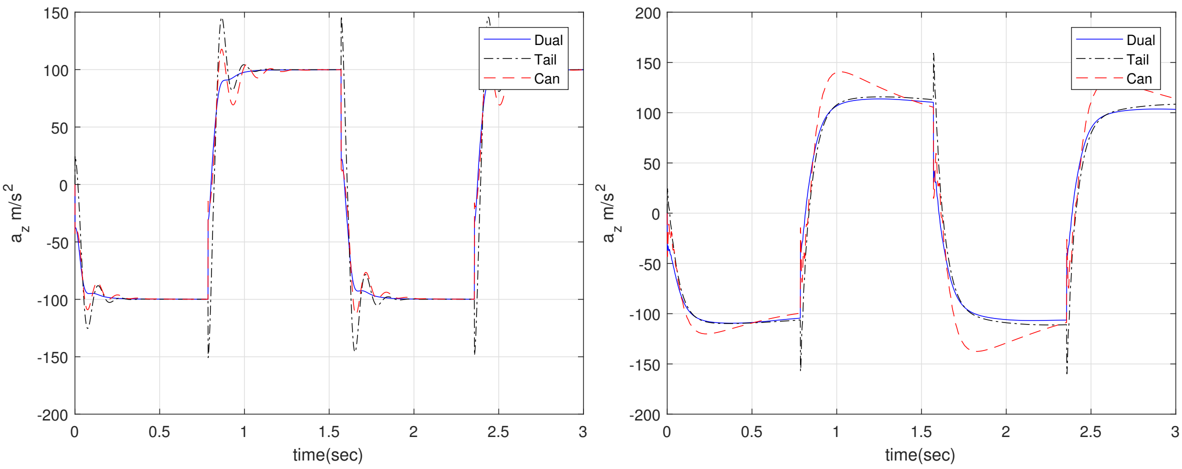

(a) Baseline autopilot.

(b) OCM autopilot.

Figure 4.3: Normal acceleration response for different missile configurations.

The angle-of-attack response of the three configurations with baseline and OCM controller are depicted in figures 4.4a and 4.4b. Similar to the acceleration response, the adaptive control angle-of-attack response eliminates the oscillation in the canard-only and tail-fin-only resulting in a smooth transient response. It is clear from the pitch response of the three configuration with OCM adaptive controller that adaptive controller improves the overall angular response (see Figs. 4.5a and 4.5b).

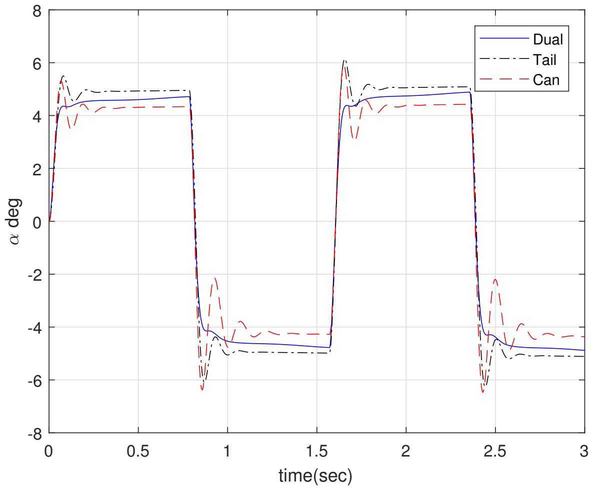

(a) Baseline autopilot.

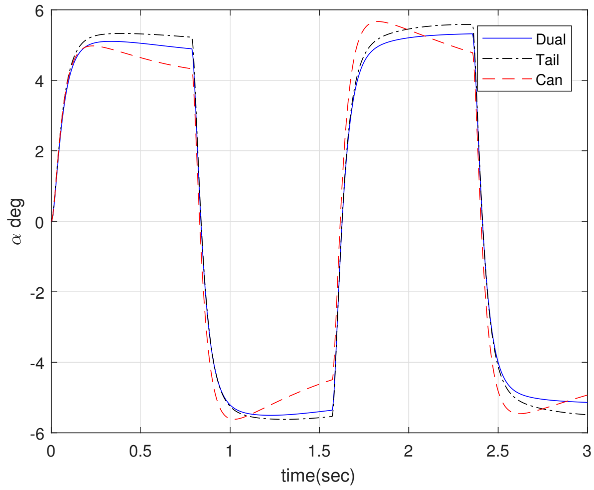

(b) OCM autopilot.

Figure 4.4: Angle-of-attack response for different missile configurations.

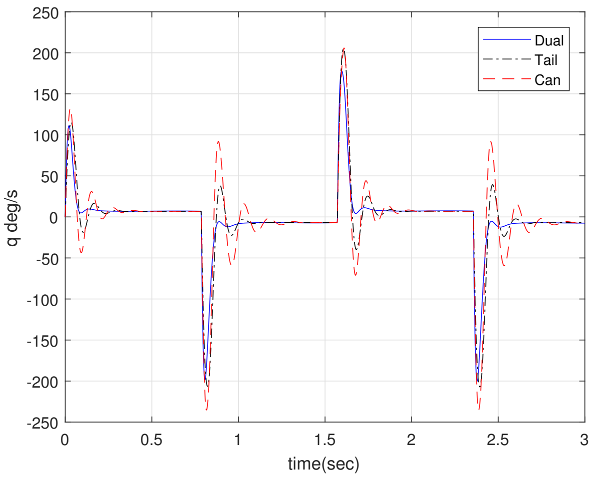

(a) Baseline autopilot.

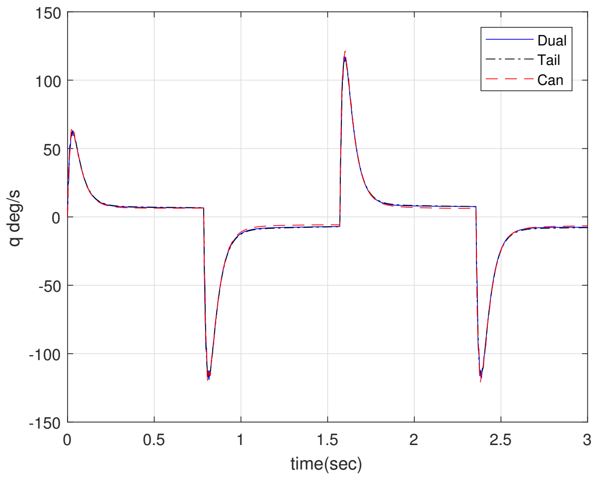

(b) OCM autopilot.

Figure 4.5: Pitch rate response for different missile configurations.

The tail-fin commands of the tail-fin-only and DAC configuration are illustrated in figure 4.6a and 4.6b. For both controllers the DAC missile shows less control deflection at each acceleration step hence suggesting that dual controller is less prone to actuator saturation. The adaptive tail-fin-only deflection shows significant improvement in terms of oscillation and settling time.

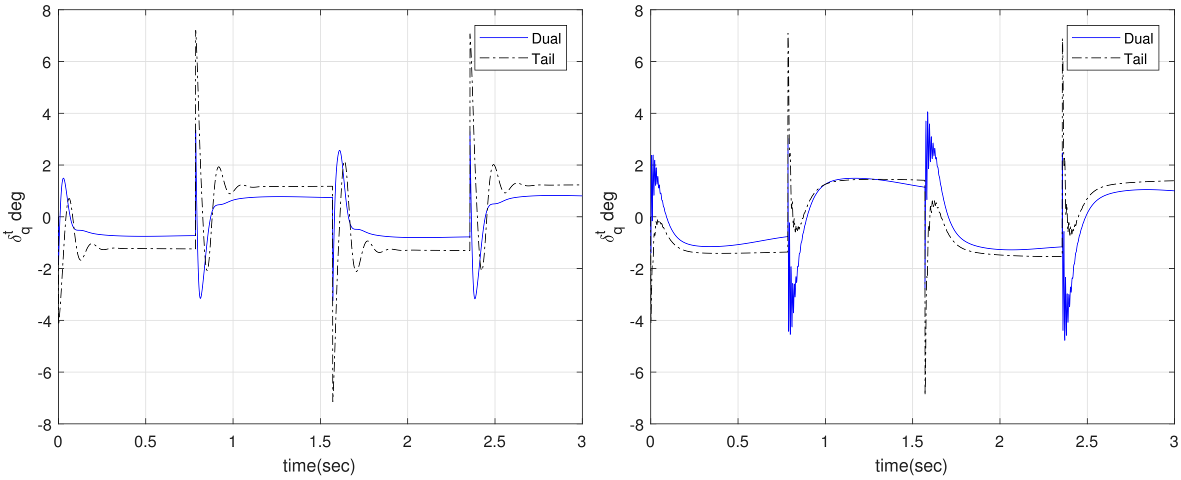

(a) Baseline autopilot.

(b) OCM autopilot.

Figure 4.6: Tail-fin pitch deflection command of tail-fin and dual missile configurations.

Figures 4.7a and 4.7b depicts the canard command of the canard-only and dual configuration baseline and OCM adaptive controllers. The canard-only missile show high steady-state value for both controller architectures. The low steady-state value in DAC control is attributed to fact that the actuation authority is shared between the tail-fins and the canards. Furthermore, the OCM controller significantly improves the behaviour of the canard commands and eliminates the inherent canard oscillations.

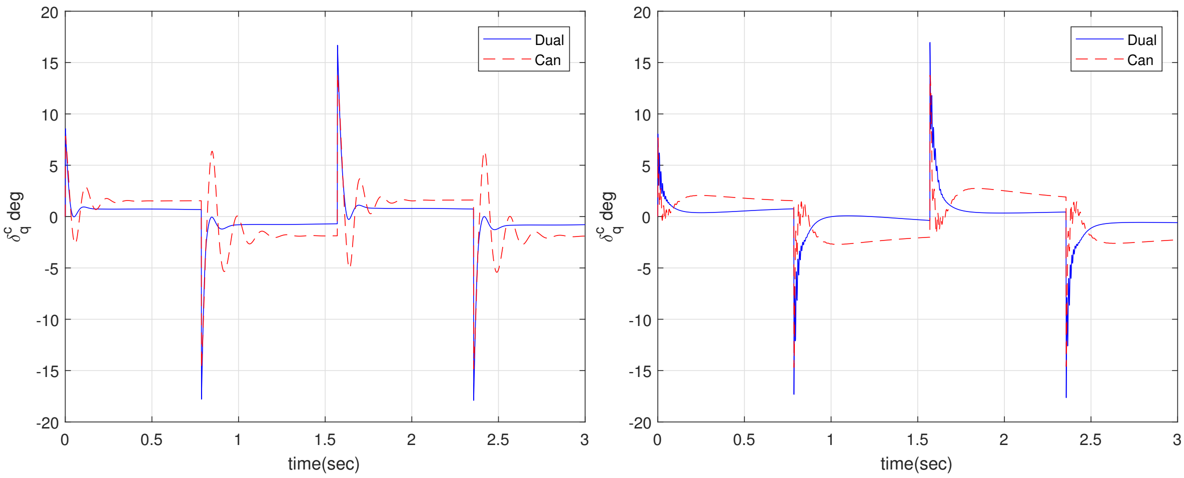

(a) Baseline

(b) OCM

Figure 4.7: Canard pitch deflection commands of canard and dual missile configurations.

4.3.2 Different Adaptive Rule for DAC Missile.

Figures 4.8 to 4.15 illustrate the 6-DoF response of DAC missile with the baseline controller and four different adaptive controllers. The adaptive controllers compared are ALR, OCM, $\sigma-$modification and $\epsilon-$ modification. Simulation for each of the adaptive controllers was set up such that it tracks a normal square wave acceleration command of amplitude 100 m/s^2, a lateral sine wave acceleration command of amplitude 100 m/s^2 and a zero roll angle throughout. Table 4.4 presents the learning rates and damping ratios used for each adaptive rule.

Table 4.4: Learning rates and damping ratio for different adaptive rules.

Update rule	Γ_Θ	Γ_W	σ_W	σ_Θ
$\epsilon-$ mod	50000	50000	0.3	$\epsilon = 0.3$
$\sigma-$ mod	50000	50000	0.01	$\sigma = 0.01$
$ALR-$mod	50000	50000	0.3	$\eta = 0.3$
OCM	50000	35000	0.3	$\nu = 0.3$

Figures 4.8 and 4.9 depict the angle-of-attack and angle-of-sideslip responses of the DAC missile with the four adaptive controllers. By introducing adaption, the tracking performance improves when compared with the baseline controller. It is clear from the angle-of-attack response that ALR and OCM improve the tracking performance quite substantially. For the case of OCM this improvement is attributed to the optimal bounded tracking error and adaption gains that strike a balance between robustness and tracking performance, while for ALR the benefit is attributed to the adaptive loop eliminating the nonlinear uncertainty and maintaining the margins of the reference model in the closed-loop.

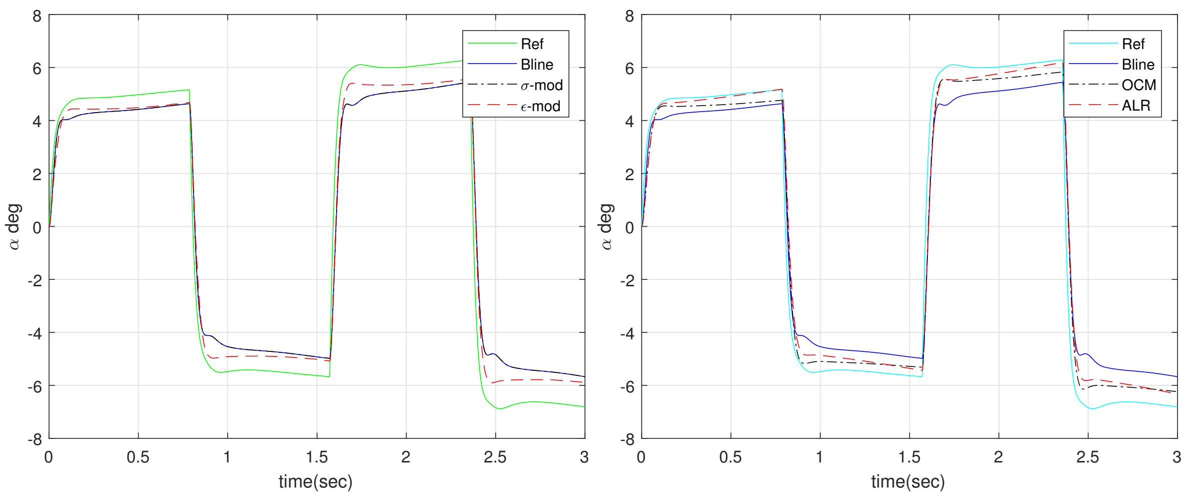

Figure 4.8: Angle-of-attack response of DAC missile for different adaptive controllers.

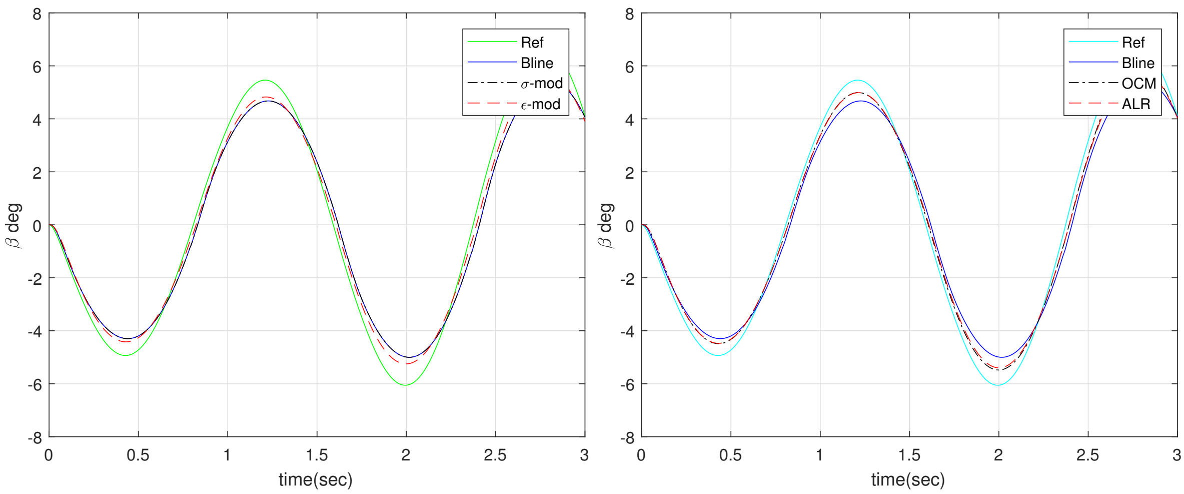

Figure 4.9: Angle-of-side-slip response of DAC missile for different adaptive controllers.

Figures 4.10 to 4.11 illustrate the body rates responses of the DAC missile with different adaptive controllers. The body rates are directly adapted to drive the missile to follow the dynamics of the reference model hence they exhibit better tracking when compared with the wind angles. Again it is evident that the ALR and OCM exhibits smooth and calmer tracking performance when compared with $\sigma-$ and $\epsilon-$ modifications for the same reason mentioned in the above paragraph. Figures 4.17 to 4.18 illustrate the responses of the lateral acceleration, normal acceleration and the roll angle. The outer-loop responses of the adaptive controllers remain relatively comparable, even though they do not settle at the same steady-state value. The steady-state error can be accounted for by adaptive controller not eliminating all uncertainty due to the unmatched nature of the plant uncertainty.

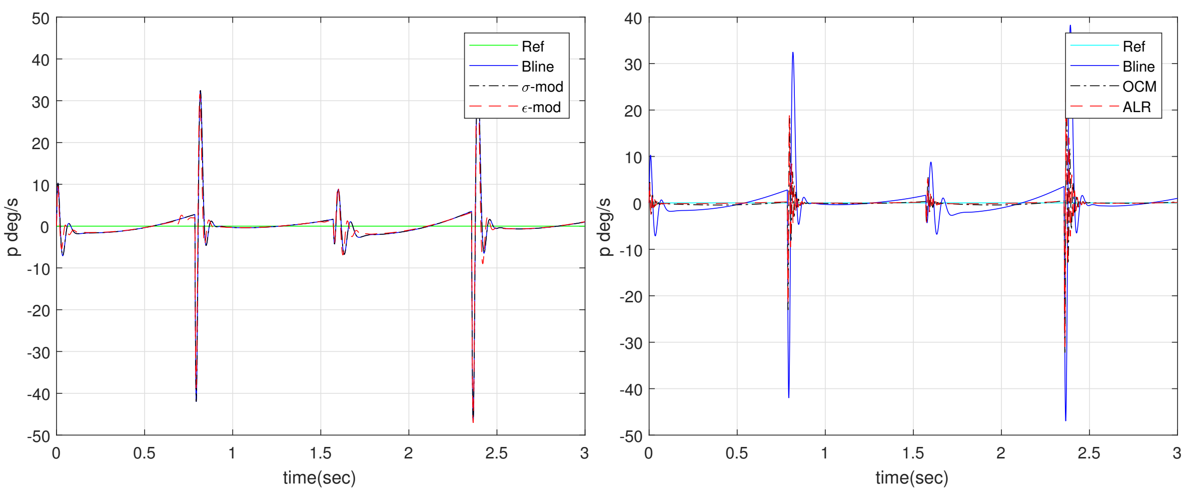

Figure 4.10: Roll rate response of DAC missile for different adaptive controllers.

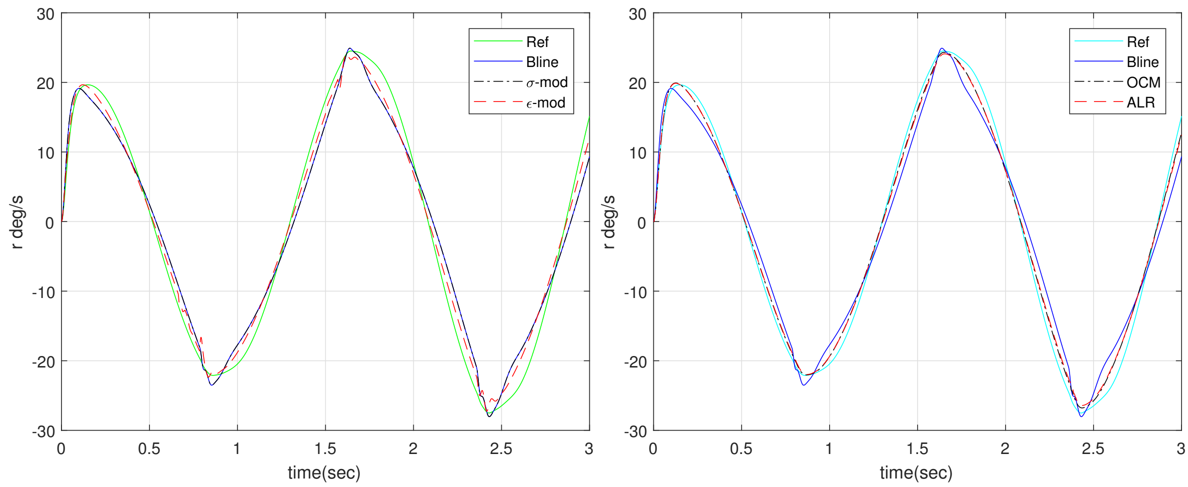

Figure 4.11: Yaw rate response of DAC missile for different adaptive controllers.

Figures 4.12 to 4.15 depict the actuator commands for the DAC missile due to the different adaptive controller considered. Figures 4.12 to 4.13 illustrate the tail-fin deflection commands and Figures 4.14 and 4.15 show the yaw and pitch deflection canard commands. The adaptive controllers show similar behaviour in command dynamics, however they all have different steady-state values. This discrepancy can be attributed to the fact that although all the adaptive rules aim to achieve UUB of the tracking error, they achieve this condition through different adaption dynamics. Adaptive yaw deflection commands appear to be mildly robust to the variation in pitch dynamics.

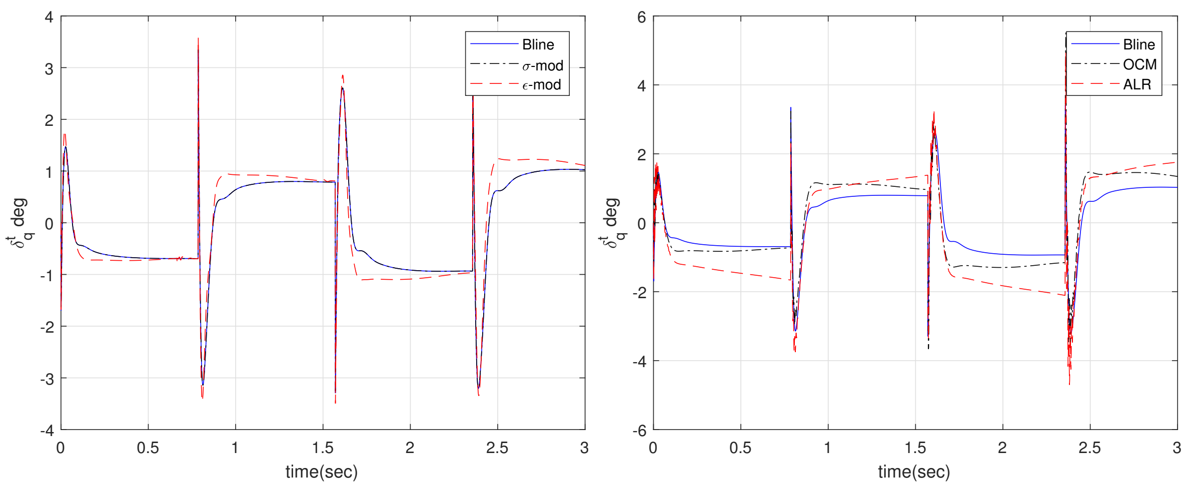

Figure 4.12: Tail-fin pitch deflections of DAC missile for different adaptive controllers.

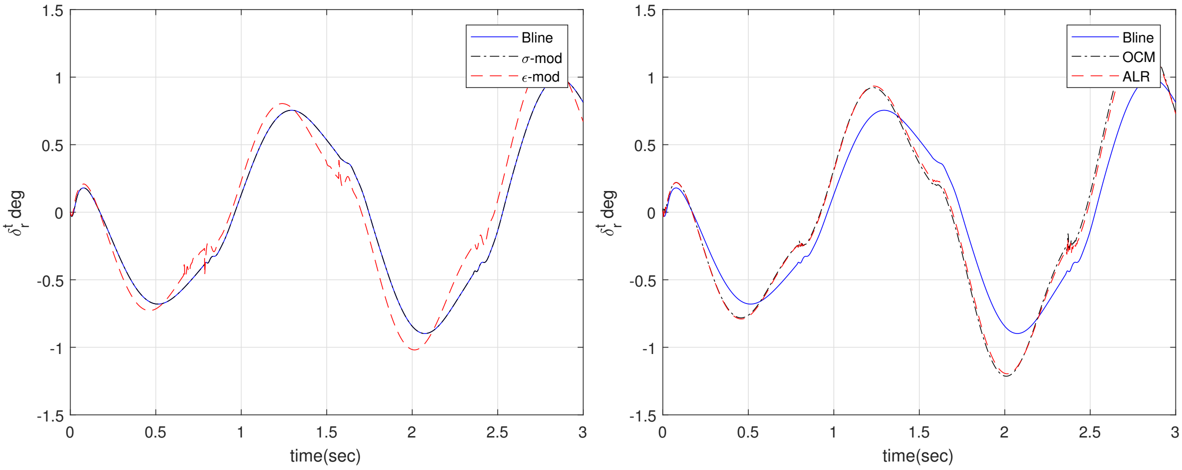

Figure 4.13: Tail-fin yaw deflections of DAC missile for different adaptive controllers.

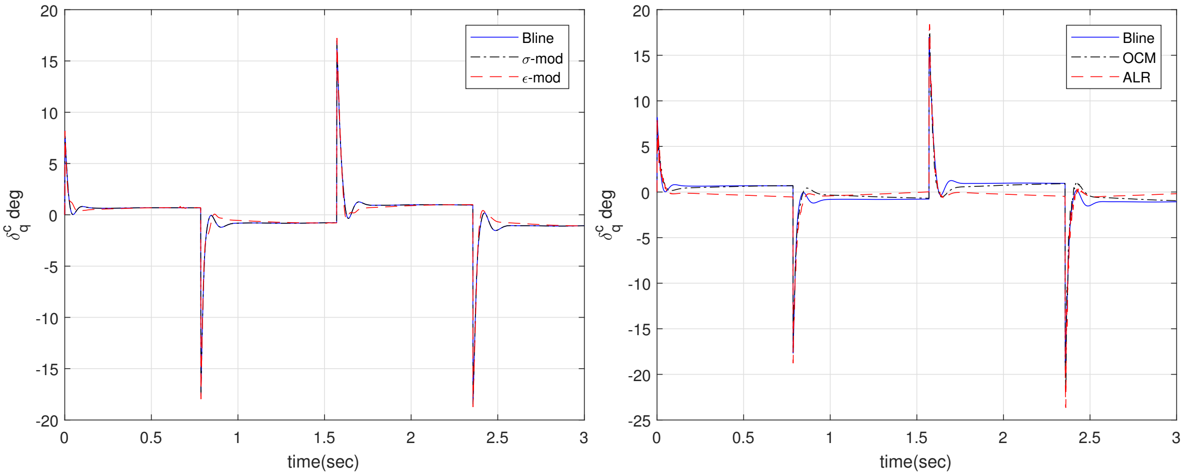

Figure 4.14: Canard pitch deflections of DAC missile for different adaptive controllers.

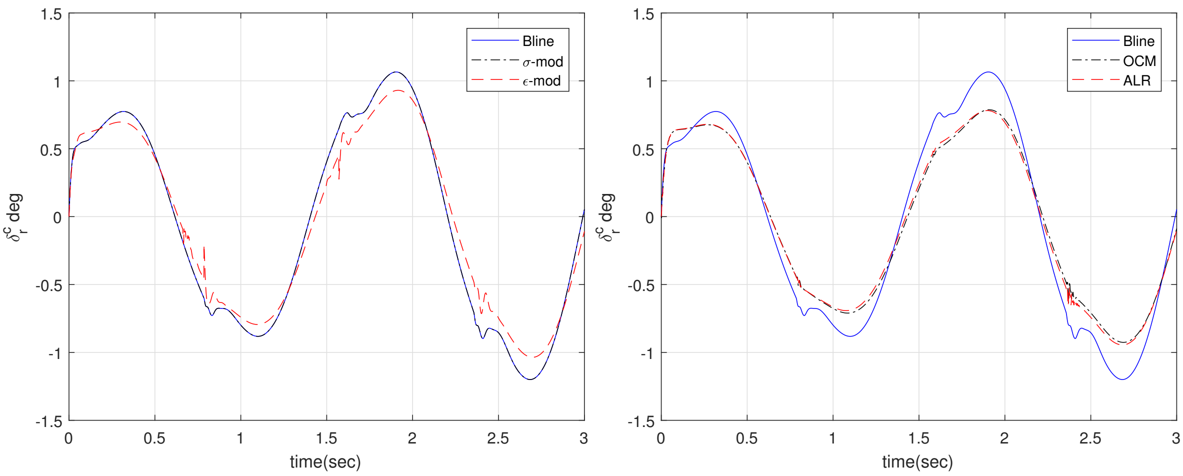

Figure 4.15: Canard yaw deflections of DAC missile for different adaptive controllers.

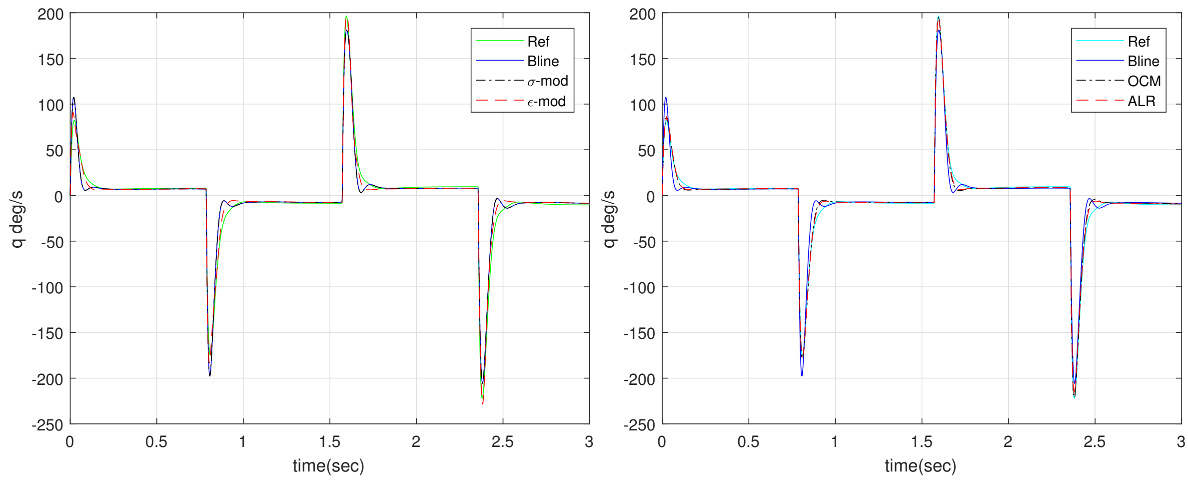

Figure 4.16: Pitch rate response of DAC missile for different adaptive controllers.

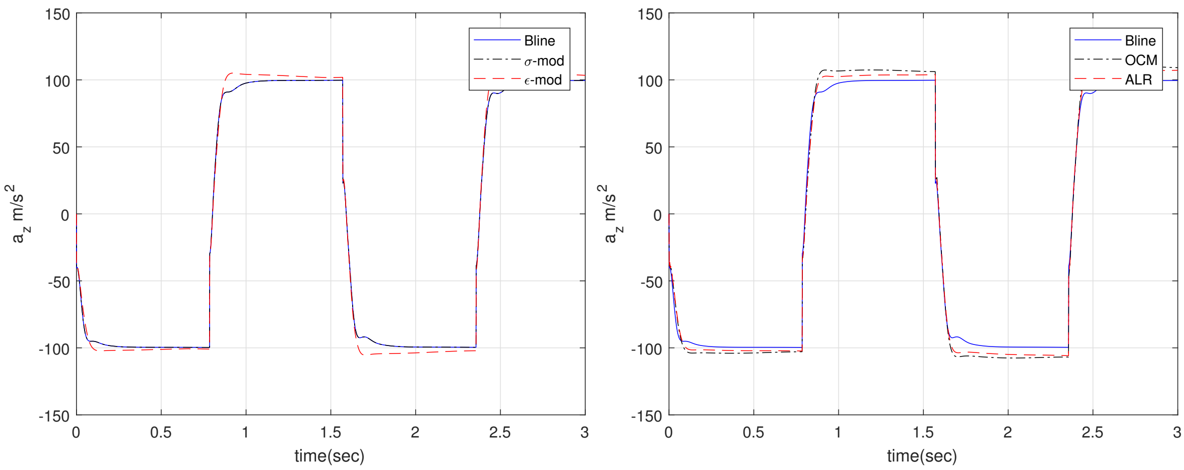

Figure 4.17: Normal acceleration response of DAC missile for different adaptive controllers.

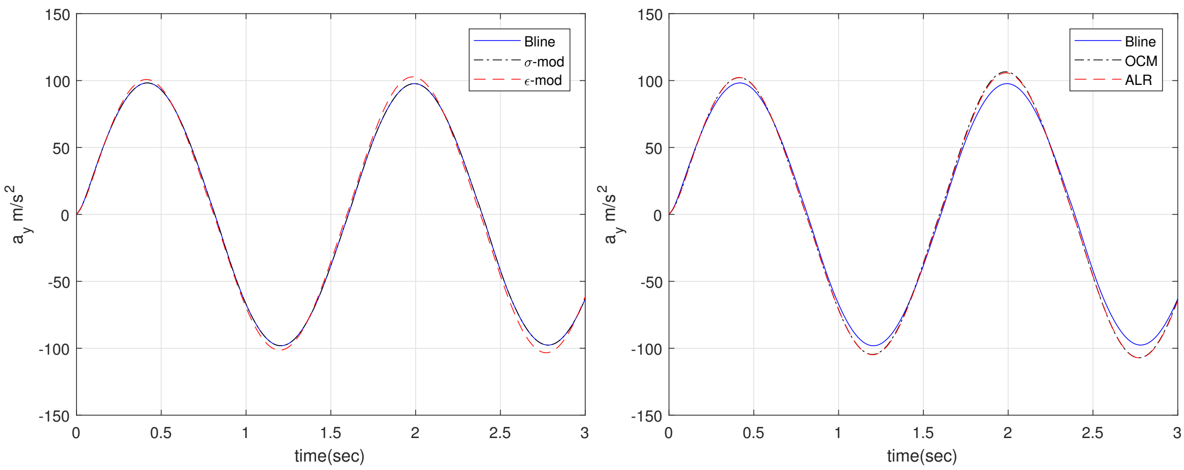

Figure 4.18: Lateral acceleration response of DAC missile for different adaptive controllers.

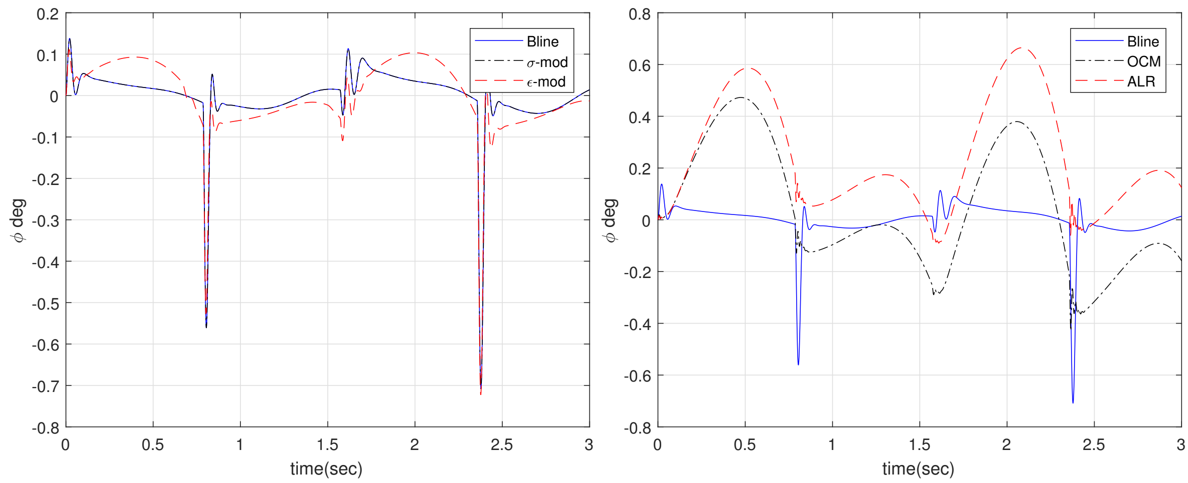

Figure 4.19: Roll angle response of DAC missile for different adaptive controllers.

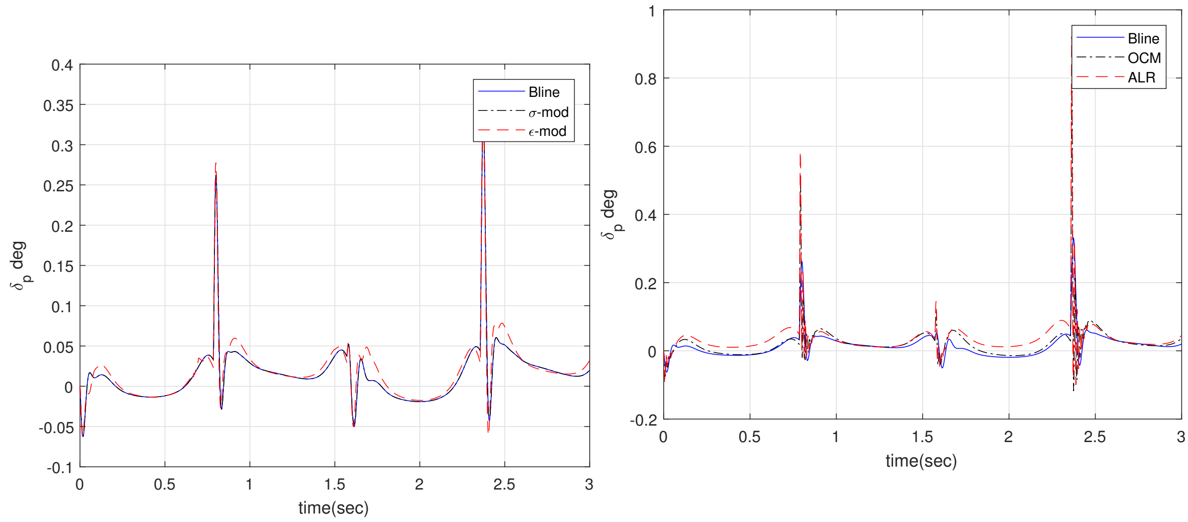

Figure 4.20: Tail-fin roll deflections of DAC missile for different adaptive controllers.

4.3.3 Normalised OCM With Co-variance Adjustment for DAC Missile.

Figures 4.21 to 4.33 illustrate the responses and actuator commands of reference model, baseline controller, standard OCM and normalised OCM with co-variance adjustment, tracking a normal acceleration square wave and lateral acceleration sine wave both with a magnitude of 100 m/s^2. $\sigma-$modification was used for updating the hidden layer weights for both OCM and normalised OCM with co-variance adjustment. A learning damping ratio of $\sigma_W = 0.3$ and $\nu = 0.3$ were used for $\sigma-$ modification and OCM. Adaptive gains of $\Gamma_\Theta = \Gamma_W = 50000I$ were used for both $\sigma-$modification and OCM adaption. Such high adaptive gains are necessary to guarantee that the update of the neural network weights is done sufficiently fast to ensure adequate controller performance. Initial adaptive gains of

$\Gamma_{\Theta_0} = 70000I$ were used for the normalised OCM with co-variance adjustment. Co-variance adjustment parameter of $\eta_\Theta = 0.0001$ and normalisation matrix $R = 0.1I$ were selected.

Figures 4.21 to 4.22 compare the body rate responses of the baseline and adaptive controllers to reference model response. It is clear from the response that adaption improves the tracking performance of the controller. Figures 4.24 and 4.25 illustrate angle-of-attack and angle-of-sideslip responses of the reference model, baseline controller and adaptive controller. Although the angle-of-attack and angle-of-sideslip of the plant are not directly driven like the body rates to follow the reference model, the angle-of-attack and angle-of-sideslip responses of the plant do follow the reference model hence affirming that adaption of the fast dynamics is adequate to yield an acceptable plant response. It is evident from Figures 4.26 to 4.28 that the adaptive controller results in a relatively smooth tracking response.

Figures 4.29 to 4.33 compare the actuator command from the three controllers. It is evident that the baseline controller and the adaptive control pitch deflections (see Fig. 4.29) follow a similar trajectory except that the adaptive controllers have a higher steady-state pitch deflections. Yaw deflection of the tail-fin and canard (see Figs. 4.30 and 4.33) follow a smooth sinusoidal trajectory inherited from the lateral sinusoidal acceleration command. Canard pitch deflection exhibits the highest deflection (see Fig.4.32) at each step change, this can be attributed to the fact that the canards have more control authority at low angle-of-attack. Baseline canard pitch deflection follows a slightly oscillatory trajectory, while the adaptive deflection are relatively smooth. Spikes on the roll deflection (see Fig.4.31) can be attributed to the roll controller rejecting disturbances induced by the pitch-roll and yaw-roll coupling dynamics. An overall observation on both deflections and wind angles is that the steady magnitude of the responses seems to be increasing with time for the same acceleration command, this phenomenon is attributed to the fact that as the airspeed decrease due to drag more control authority is needed to track the same acceleration commands.

Figures 4.34 to 4.37 compare the estimate of the uncertain dynamics with the actual unmodelled plant dynamics for standard OCM update rule and normalised OCM with co-variance adjustment update rule. The estimates of both adaptive controllers do not match the unmodelled dynamics and this phenomenon is explained by the fact that an adaptive controller serves a purpose of driving the closed-loop response to track the reference model closely irrespective of uncertainty estimation convergence. Figure 4.38 illustrates the time varying adaptive gain of the normalised OCM with co-variance adjustment. The adaptive gains are adjusted to a lower value by default due to absence of a forget factor in the co-variance adjustment rule. From the plant response it is clear that the adaptive gain adjustment did not penalise controller performance even for cases where the adaptive gain is far below the initial adaptive gain used in the standard OCM.

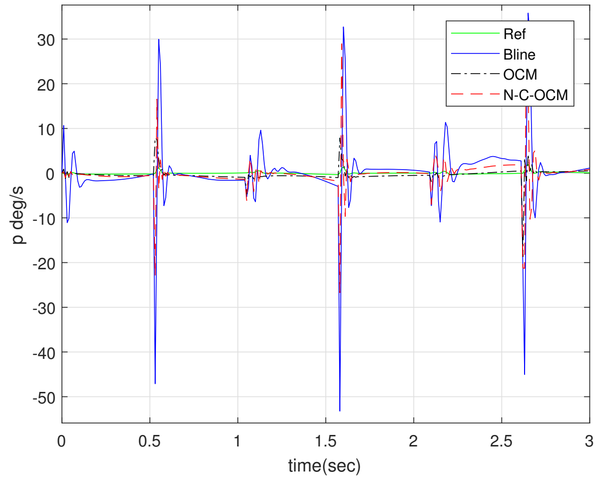

Figure 4.21: Roll rate responses of the reference model, baseline controller, adaptive standard OCM and adaptive normalised.

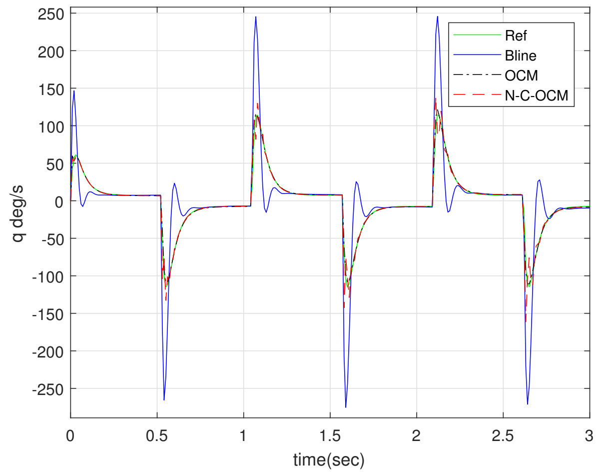

Figure 4.22: Pitch rate responses of the reference model, baseline controller, adaptive standard OCM and adaptive normalised OCM.

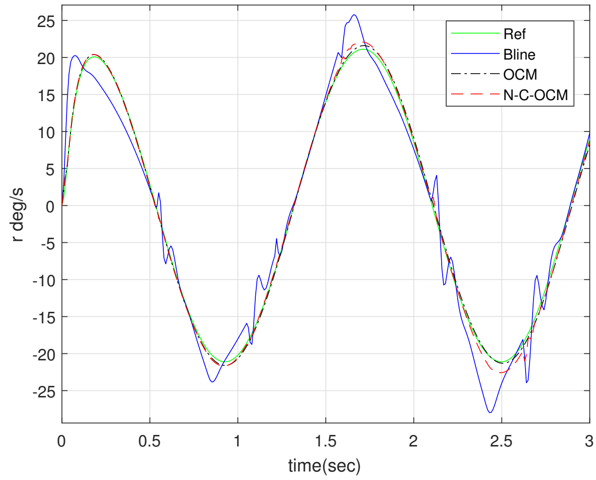

Figure 4.23: Yaw rate responses of the reference model, baseline controller, adaptive standard OCM and adaptive normalised OCM.

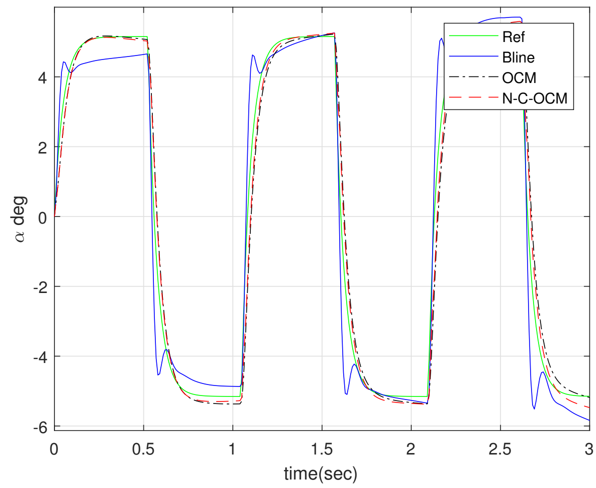

Figure 4.24: Angle-of-attack response of the reference model, baseline controller, adaptive standard OCM and adaptive normalised OCM.

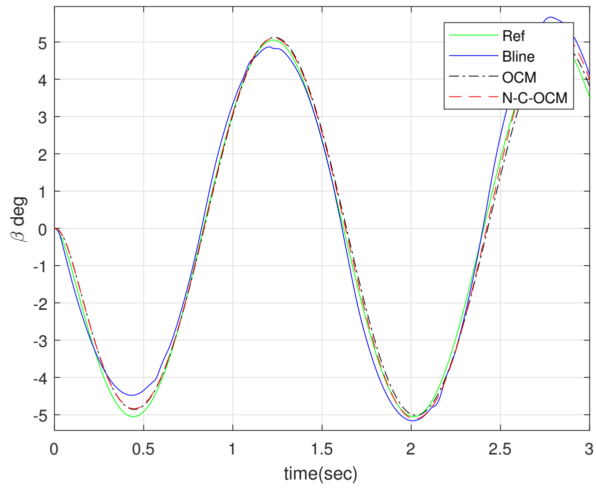

Figure 4.25: Angle-of-sideslip response of the reference model, baseline controller, adaptive standard OCM and adaptive normalised OCM.

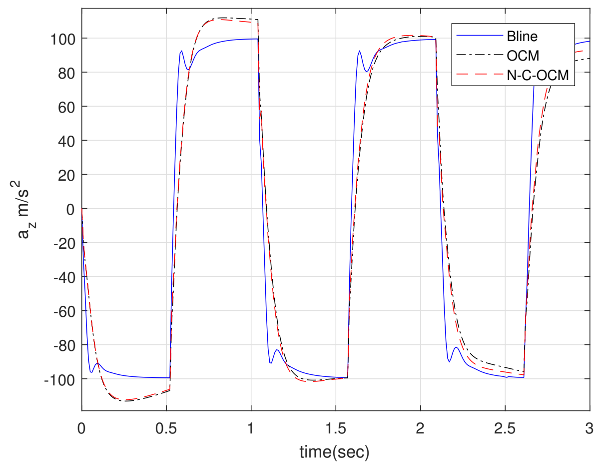

Figure 4.26: Normal acceleration responses of baseline controller, adaptive standard OCM and adaptive normalised OCM.

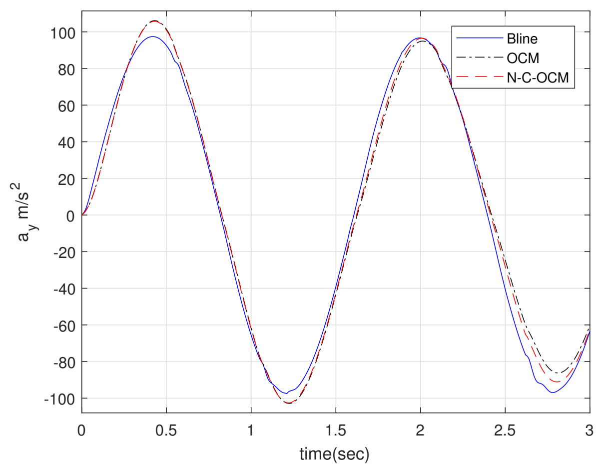

Figure 4.27: Lateral acceleration responses of baseline controller, adaptive standard OCM and adaptive normalised OCM.

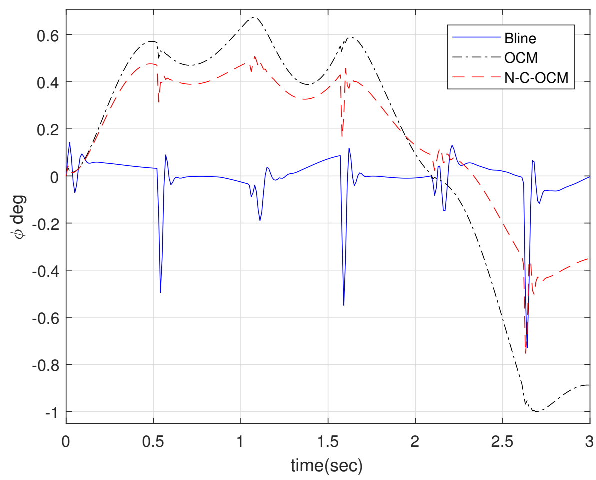

Figure 4.28: Roll Euler angle responses of baseline controller, adaptive standard OCM and adaptive normalised OCM.

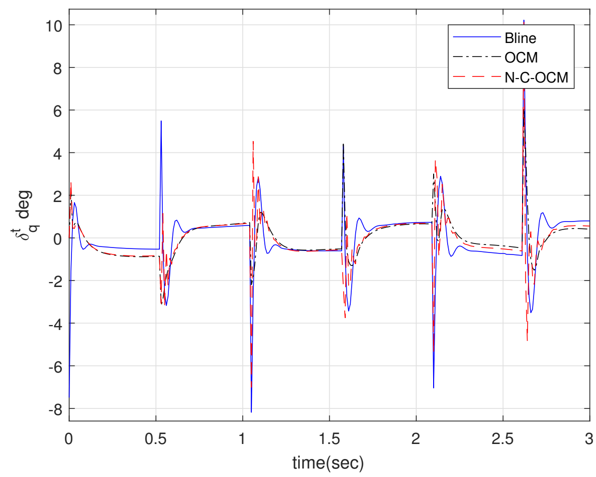

Figure 4.29: Tail-fin pitch deflections of baseline controller, adaptive standard OCM and adaptive normalised OCM.

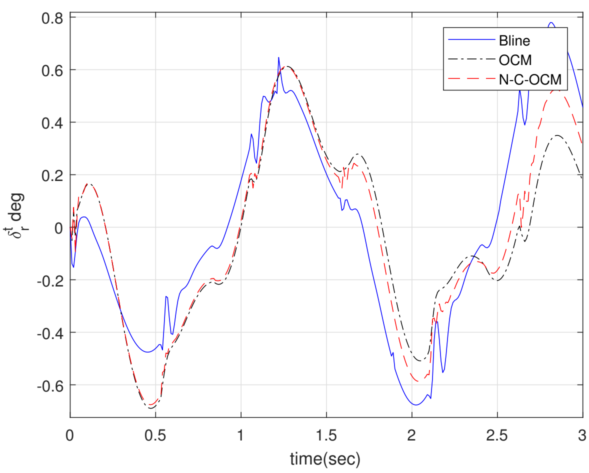

Figure 4.30: Tail-fin yaw deflections of baseline controller, adaptive standard OCM and adaptive normalised OCM.

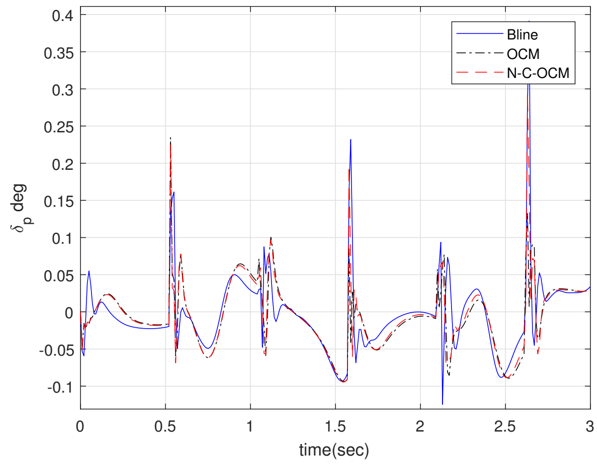

Figure 4.31: Tail-fin roll deflections of baseline controller, adaptive standard OCM and adaptive normalised OCM.

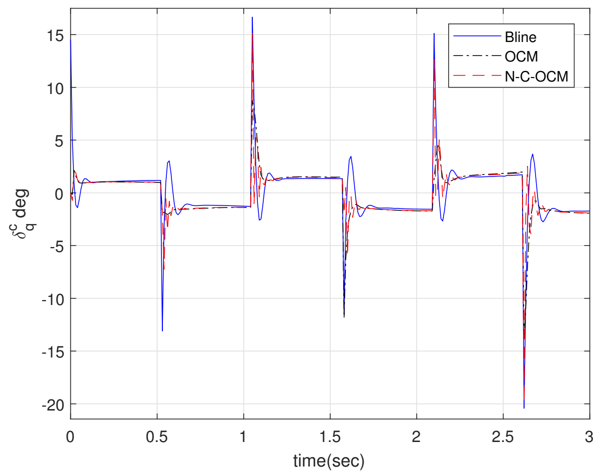

Figure 4.32: Canard pitch deflections of baseline controller, adaptive standard OCM and adaptive normalised OCM.

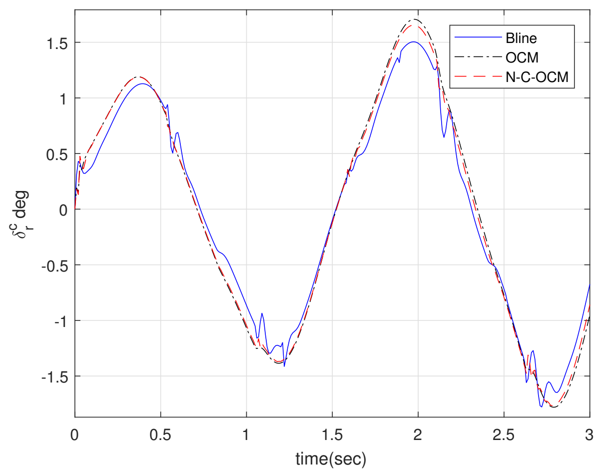

Figure 4.33: Canard yaw deflections of baseline controller, adaptive standard OCM and adaptive normalised OCM .

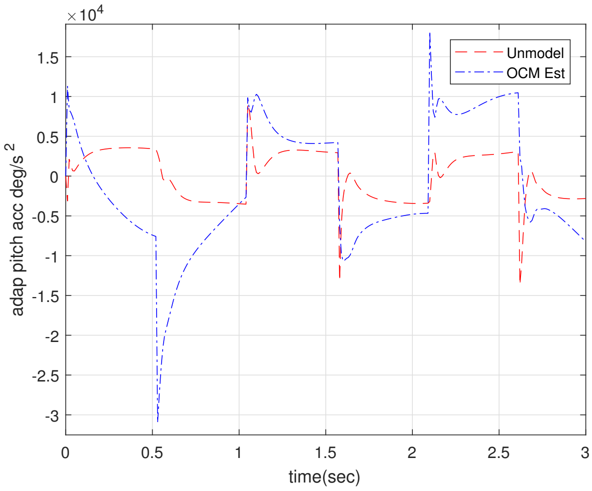

Figure 4.34: OCM estimated unmodelled pitch dynamics.

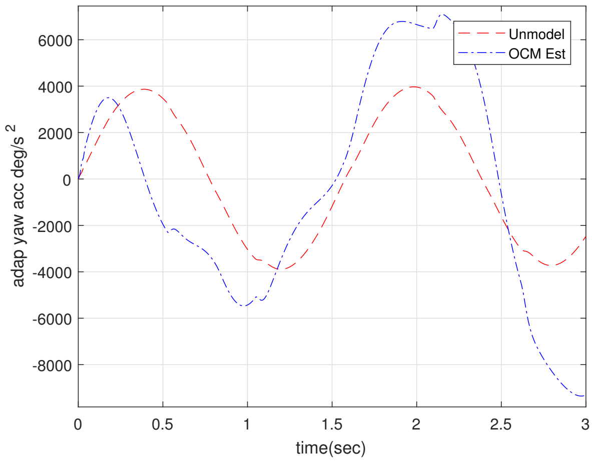

Figure 4.35: OCM estimated unmodelled yaw dynamics.

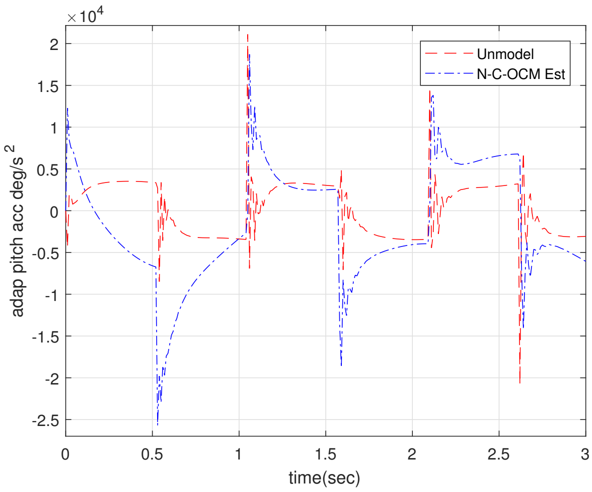

Figure 4.36: Normalised OCM with co-variance adjustment estimated unmodelled pitch dynamics.

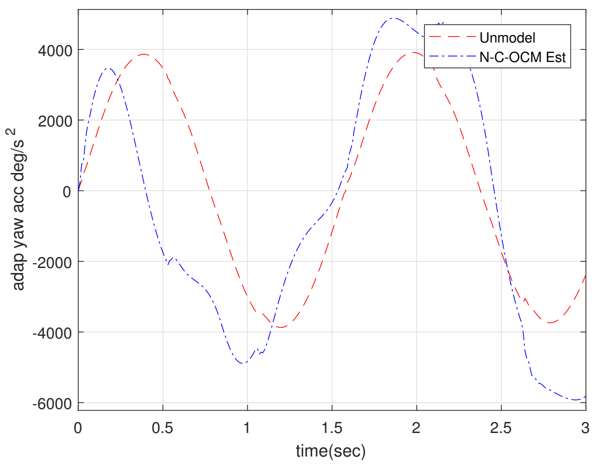

Figure 4.37: Normalised OCM with co-variance adjustment estimated unmodelled pitch dynamics.

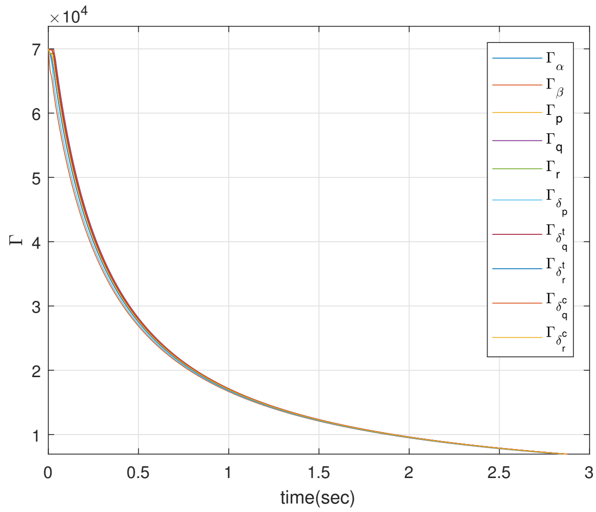

Figure 4.38: Time varying adaptive gain of normalised OCM with normalise co-variance adjustment adaptive gain .

Chapter 5

Homing Loop: Missile Guidance and Target Tracking

In this chapter a homing loop of a DAC missile with adaptive autopilot is presented. Only the cruise terminal phase is considered in this chapter. The homing loop serves to track the target, generate commands for the autopilot and accounts for velocity variations which were neglected when designing the autopilot in the previous chapter.

5.1 Homing Loop

The homing loop is the mostouter and critical loop on the flight control because it determines the overall performance of the missile against manoeuvring targets. Figure 5.1 illustrates the major components that define the missile flight control system. The homing loop is made up of the target tracker (active radar seeker) and guidance block which consists of a target tracking filter/states estimator, the guidance rule and the target acceleration model. Extraneous inputs to the flight controller are the target dynamics and tracking noise. A seeker is used to measure the relative kinematics between the target and the missile during the terminal phase. An active radar seeker is capable of measuring the relative distance, line-of-sight angles and the closing speed. The state estimator is used to filter measurement noise and to estimate unmeasured target states such as target acceleration. Estimated states are fed to a guidance law that determines the required acceleration necessary to get the missile into a collision course with the target at minimum energy cost. Guidance commands are fed to the autopilot which in turn drives the servos to change the orientation of the missile and alter the relative trajectory of missile until it is on the desired collision course.

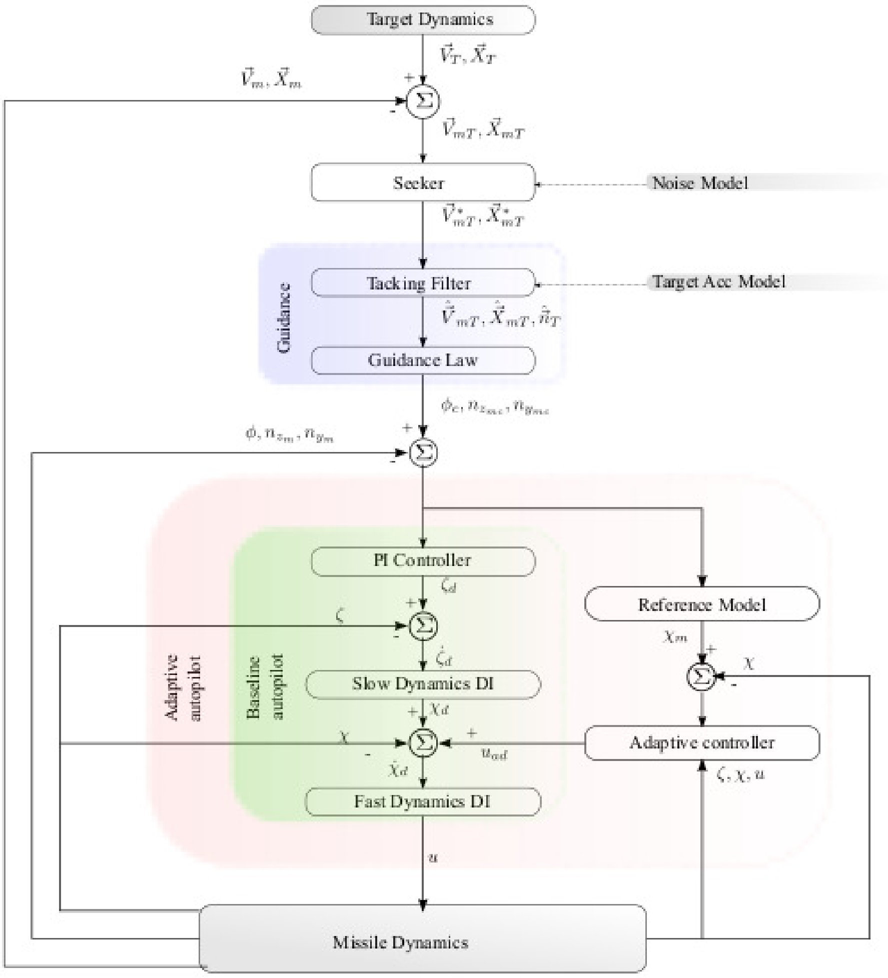

Figure 5.1: Schematic of a missile adaptive flight control system.

5.1.1 Guidance Law

The purpose of the guidance as previously alluded to, is to provide autopilot commands that alter the trajectory of a vehicle by prescribing certain states to compel the vehicle to follow a desired trajectory. The aim of the guidance law in a tactical missile is to prescribe inertial acceleration of the missile to ensure that it is on a collision course with the target. Proportional navigation-based guidance rules are the preferred guidance law for missile terminal guidance. Firstly, because they have been proven countless of time in application and secondly, because they provide a simple interface with an acceleration autopilot common in missile terminal flight control (Palumbo et al., 2010). Figure 5.2 illustrates the planar missile target engagement. The PN guidance rule ensures that the missile stays on a collision course with the target.

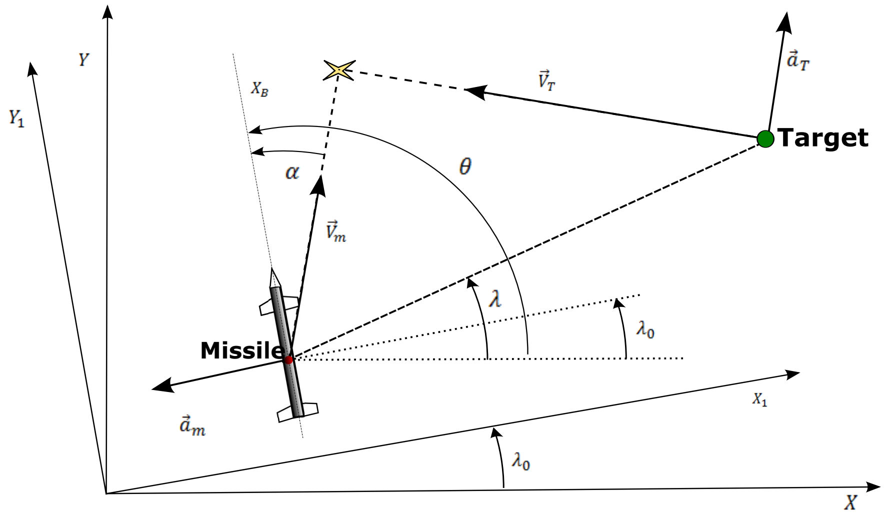

Figure 5.2: Missile target engagement geometry.

Equation 5.1 defines the augmented proportional navigation rule in vector form.

$$\vec{n}_{Mc} = \mathcal{N}\frac{\vec{R}_{TM} \times \vec{V}_{TM}}{\left\|\vec{R}_{TM}\right\|^2} \times \vec{V}_{TM} + \frac{\vec{n}_T}{2} \tag{5.1}$$

where $\vec{n}_{Mc}$ is the commanded missile acceleration, $\mathcal{N}$ is the guidance gain, $\vec{R}_{TM}$ is the relative position vector between the missile and the target, $\vec{V}_{TM}$ is the relative velocity vector and $\vec{n}_T$ is the target acceleration.

The augmented PN guidance takes into account the acceleration of the target and reduces the acceleration commands necessary to counter the target. Inclusion of the target acceleration increases the complexity of the target tracking filter but has an advantage that it preserves kinetic energy to ensure effective target engagement. Preservation of the kinetic energy is critical because most tactical missile are cruising without propulsion during the terminal phase.

5.2 Perfect Target Engagement Simulation.

This section presents ideal engagement scenario of the DAC missile against a weaving target and a constant manoeuvre target. A constant manoeuvre target aims to get out of the missile kill zone by accelerating as quickly as possible, while a weaving target aims to dissipate the kinetic energy of the missile by having it track an oscillating target position. A perfect seeker is assumed to demonstrate the effectiveness of the flight control against weaving targets and constant manoeuvre. A guidance gain of $\mathcal{N} = 4$ was found to be effective and it is used in all the homing simulations. Table 5.1 details the initial conditions of the target and the missile. The manoeuvring target follows a sinusoidal acceleration in both lateral and normal direction with an amplitude of 20g at a frequency of 2 rad/s. The constant manoeuvre target does a pull-up manoeuvre of 20g in the normal direction for 3s and then does a pull-down manoeuvre 20g for the remainder of the flight. A target engagement scenario was considered successful if the missile achieved a radial miss distance of 2.0 m or less.

Table 5.1: Initial conditions for missile and target for different scenarios.

	Acc Amplitude (g)	$\omega_{acc} rad$	$(U_0, V_0, W_0) m/s$	$(x_0, y_0, z_0) m$
Missile	N/A	N/A	(1000,0,0)	(0, 0, -6000)
Weaving Tgt	20	2	(-300,0,0)	(7000, 2000, -6000)
Cst Man Tgt	$a_T(t < 3) = 20, a_T(t > 3) = -20$	N/A	(-300,0,0)	(7000 , 2000, -6000)

Figures 5.3 to 5.5 illustrate the engagement trajectories and the airspeed of a DAC missile and tail-fin-only missile against weaving and constant manoeuvre. Engagement is simulated with augmented proportional navigation guidance law for different autopilots: OCM and baseline autopilot. Figures 5.3a and b illustrate the x-z engagement plane. It is clear from the trajectories that the type of autopilot has little effect on the nominal trajectory followed by the missile (see Figs. 5.3 and 5.4). Figure 5.5 shows the airspeed variation during target engagement period. The airspeed drops sharply for constant manoeuvre engagement scenario and this is due to high angles-of-attack needed to follow the commanded high normal acceleration (see Fig. 5.5a). The airspeed for the weaving target engagement scenario decreases in an oscillatory fashion as a result of tracking a target with oscillating dynamics (see Fig. 5.5b). The DAC missile was able to achieve a miss distance of below 2.0 m with both baseline and OCM autopilot. Tail-fin missile was able to achieve below 2.0 m missile with the OCM autopilot and the scenarios with a baseline autopilot resulted in a below 5 m misses.

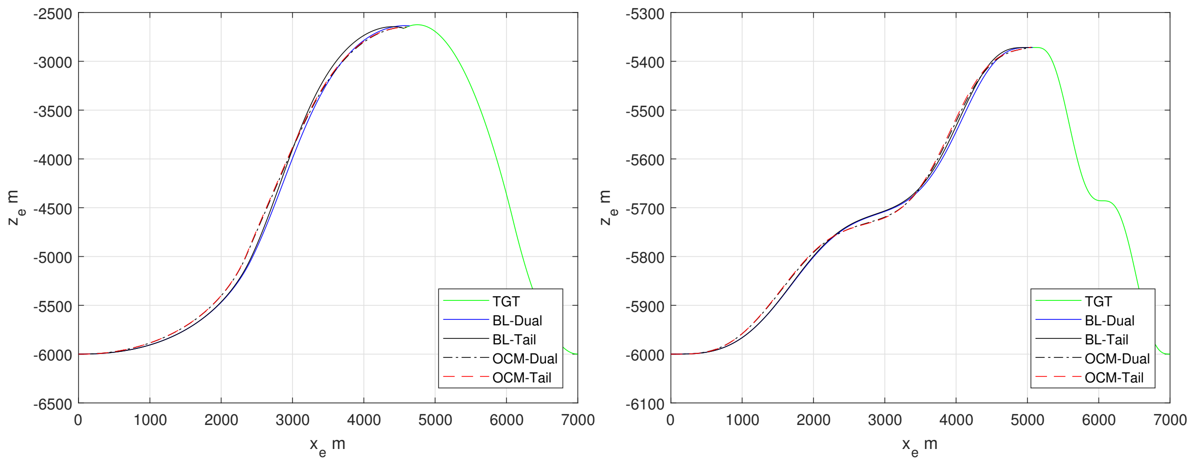

(a) Constant manoeuvre target.

(b) Weaving target.

Figure 5.3: x-z plane view of DAC missile and tail-fin target engagement scenarios.

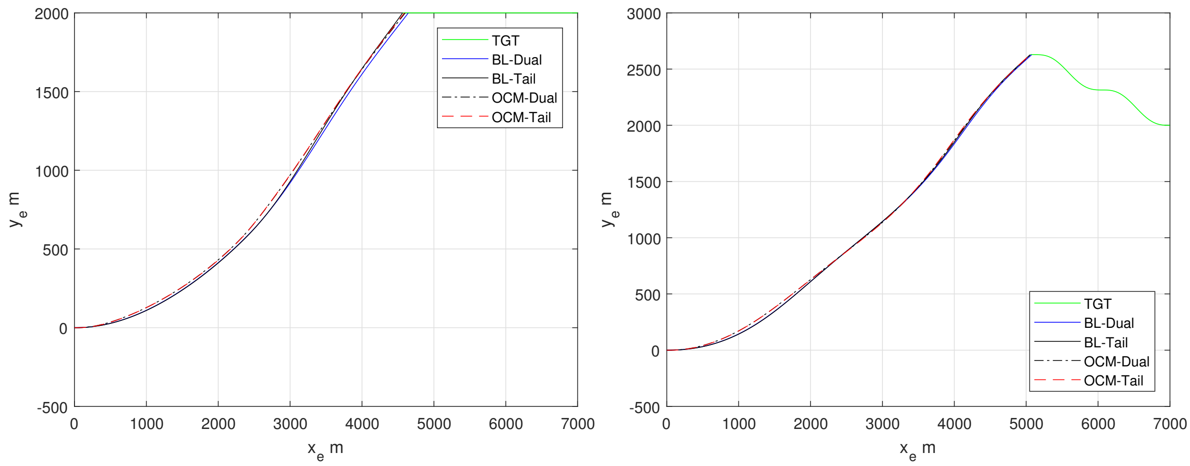

(a) Constant manoeuvre target.

(b) Weaving target.

Figure 5.4: x-y plane view of DAC missile and tail-fin target engagement scenarios

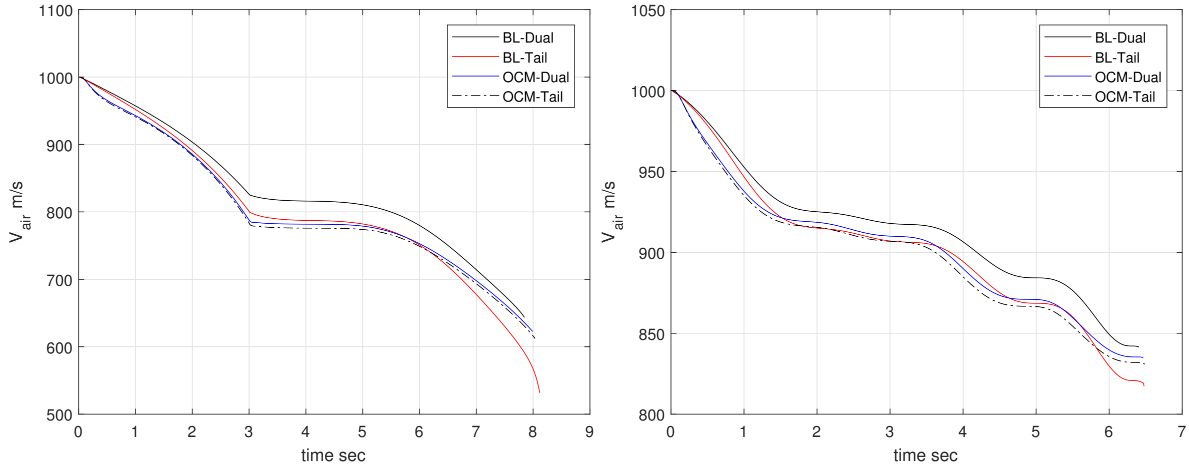

(a) Constant manoeuvre target.

(b) Weaving target.

Figure 5.5: Missile airspeed variation during DAC missile and tail-fin target engagement.

Figures 5.6 to 5.8 illustrate the engagement kinematics of a DAC missile against a constant manoeuvre target and weaving target. The figures compare the kinematics of a DAC missile with baseline autopilot with that of the OCM and normalised OCM with co-variance adjustment. There is very little variation between the trajectory followed by the OCM and the normalised OCM with co-variance adjustment hence suggesting that a reduced adaptive gain in the normalised OCM with co-variance adjustment does not penalise the overall performance of the missile.

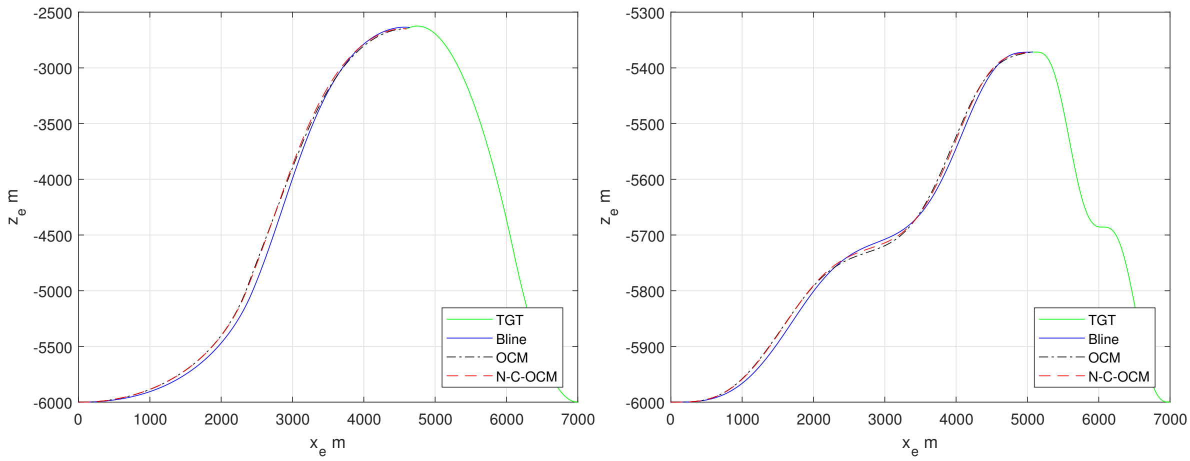

(a) Constant manoeuvre target.

(b) Weaving target.

Figure 5.6: x-z plane view of DAC missile (with different autopilots) target engagement scenarios.

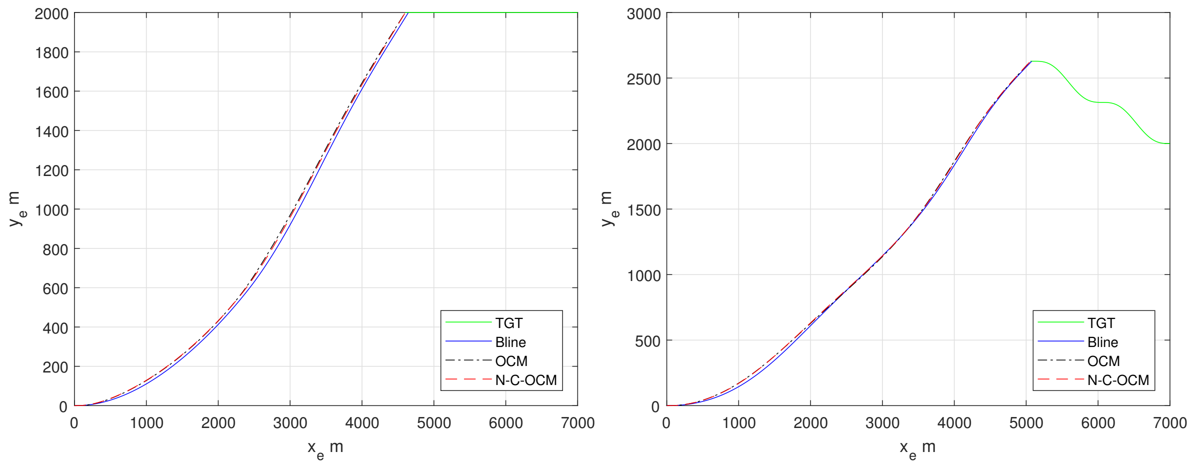

(a) Constant manoeuvre target. (b) Weaving target.

Figure 5.7: x-y plane view of DAC missile (with different autopilots) target engagement scenarios.

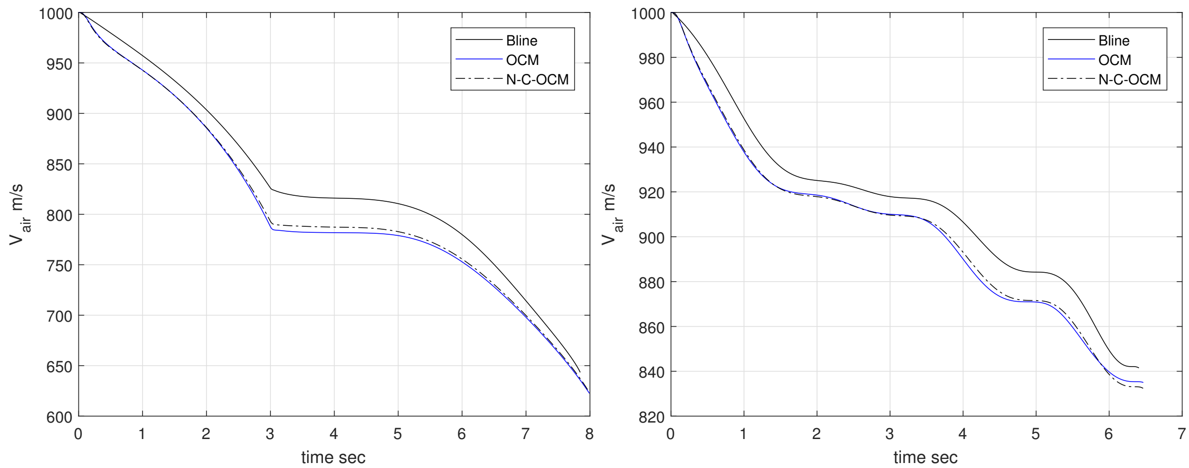

(a) Constant manoeuvre target. (b) Weaving target.

Figure 5.8: Airspeed variation of a DAC missile (with different autopilots) target engagement scenarios.

5.3 Target Tracking Filter

An active radar seeker model is used as the target tracker for the DAC missile. The seeker provides pseudo-measurements of the target position by measuring the line of sight angles and closing in range from the target. Pseudo measurement of the closing in velocity are done by examining the Doppler shift of the radar signal (Chen et al., 2006). Seeker measurements contain noise in the real world hence the need for a noise filter. Measurements are corruptd by mainly range dependent thermal noise and fading noise (Zarchan, 2012).

The noise is widely considered to be white noise with zero mean and can be reasonably approximated with a normal distribution (Ibarrondo, 2015). Main objective of the tracking filter is to remove measurement noise of the seeker and estimate both measured and unmeasured states from the noisy signal. The number of estimated states are driven by the guidance rule employed and the capabilities of the seeker. For augmented proportional navigation guidance law a three-state Kalman filter is needed for each axis to estimate the closing range, speed and target acceleration for one to get the full benefits of the augmented PN. The following subsection presents a nine-state linear Kalman filter that estimates closing velocity, range and the target acceleration vectors.

5.3.1 Nine-State Guidance Kalman Filter

Linear Kalman filter is the preferred guidance state estimator because it is reliable and easy to implement. Equation (5.2) defines the time varying linear Kalman filter. The filter is time varying because of the non-stationary noise co-variance as a result of range-dependent thermal noise (Palumbo et al., 2010):

$$\dot{\hat{\boldsymbol{x}}}_{\boldsymbol{f}} = A_f \hat{\boldsymbol{x}}_{\boldsymbol{f}} + B_f \boldsymbol{u}_{\boldsymbol{f}} + \boldsymbol{\mathcal{W}} \tag{5.2a}$$

$$\boldsymbol{z}^*_{\boldsymbol{f}} = H_f \boldsymbol{x}_{\boldsymbol{f}} + \boldsymbol{\mathcal{V}} \tag{5.2b}$$

where the state vector is given by $\hat{\boldsymbol{x}}_{\boldsymbol{f}} = \begin{bmatrix} \vec{R}_{TM} & \vec{V}_{TM} & \vec{n}_T \end{bmatrix}^T$, measurement vector is defined by $\boldsymbol{z}^*_{\boldsymbol{f}} = \begin{bmatrix} \vec{R}^*_{TM} & \vec{V}^*_{TM} \end{bmatrix}^T$ and $\boldsymbol{u}_{\boldsymbol{f}} = \vec{n}_m$ is the missile acceleration. A_f is the state matrix, B_f is the control input matrix, H_f is the measurement matrix, $\boldsymbol{\mathcal{V}}$ is the measurement noise vector and $\boldsymbol{\mathcal{W}}$ is the white noise process vector.

The state matrix A_f, the control input matrix B_f and the measurement matrix H_f of the filter are defined as follows:

$$A_f = \begin{bmatrix} [0] & \boldsymbol{I}_3 & [0] \\ [0] & [0] & \boldsymbol{I}_3 \\ [0] & [0] & [0] \end{bmatrix}, B_f = \begin{bmatrix} [0] \\ [0] \\ \begin{bmatrix} -1 & -1 & -1 \end{bmatrix}^T \end{bmatrix}, H_f = \begin{bmatrix} \boldsymbol{I}_3 & [0] & [0] \\ [0] & \boldsymbol{I}_3 & [0] \end{bmatrix}$$

The measurement noise vector $\boldsymbol{\mathcal{V}}$ and the white noise process vector $\boldsymbol{\mathcal{W}}$ are defined as follow:

$$\boldsymbol{\mathcal{V}} = \begin{bmatrix} \nu_R & \nu_V \end{bmatrix}^T, \boldsymbol{\mathcal{W}} = \begin{bmatrix} [0] & [0] & \vec{w} \end{bmatrix}^T$$

Equation (5.2) is valid only for continuous system. For a discrete measurement at an interval T_s, the discrete Kalman filter is given by equation (5.3). The discrete Kalman filer is common in the literature because the seeker provides discrete measurement in missile application. Figure 5.9 illustrates block diagram implementation of the discrete Kalman filter.

$$\hat{\boldsymbol{x}}_{fk} = (\boldsymbol{I}_9 - \boldsymbol{K}_{fk}H_f)(\oplus_k \hat{\boldsymbol{x}}_{fk-1} + \boldsymbol{G}_{fk}\boldsymbol{u}_{fk-1}) + \boldsymbol{K}_{fk}\boldsymbol{z}^*_{fk} \tag{5.3}$$

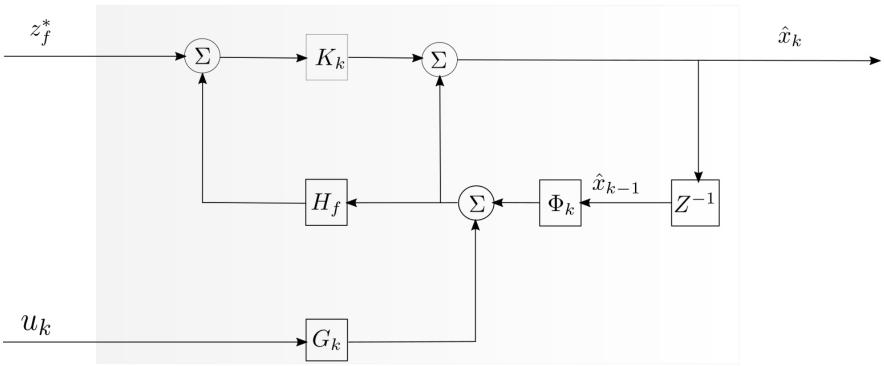

Figure 5.9: Discrete Kalman filter implementation diagram (Palumbo et al., 2010).

$\oplus$ is the fundamental matrix related to the dynamic matrix by the following expression:

$$\oplus(t) = \mathcal{L}^{-1}\{(s\boldsymbol{I}_9 - A_f)^{-1}\} = \begin{bmatrix} 1 & t & 0.5t^2 \\ 0 & 1 & t \\ 0 & 0 & 1 \end{bmatrix} \otimes \boldsymbol{I}_3 \tag{5.4}$$

where $\otimes$ is the Kronecker product.

The discrete fundamental matrix is simply the continuous matrix at time $t = T_s$:

$$\oplus_k = \oplus(T_s) \tag{5.5}$$

The discrete matrix $\boldsymbol{G}_{fk}$ is given as follows

$$\boldsymbol{G}_{fk} = \int^{T_s} \oplus(\tau)B_f(\tau)d\tau = \begin{bmatrix} -0.5T_s^2 \\ -T_s \\ 0 \end{bmatrix} \otimes \boldsymbol{I}_3 \tag{5.6}$$

The Kalman filter gains $\boldsymbol{K}_{fk}$ are calculated online using the discrete recursive Riccati equation. The recursive Riccati equation is given as follows:

$$\boldsymbol{P}_k^{(-)} = \oplus_k \boldsymbol{P}_{k-1}^{(+)} \boldsymbol{\Phi}_k^T + \boldsymbol{Q}_{fk} \tag{5.7a}$$

$$\boldsymbol{K}_{fk} = \boldsymbol{P}_k^{(-)} H_f^T (H_f \boldsymbol{P}_k^{(-)} H_f^T + \boldsymbol{R}_{fk})^{-1} \tag{5.7b}$$

$$\boldsymbol{P_{f}}_k^{+} = (\boldsymbol{I}_9 - \boldsymbol{K_{f}}_k H_f)\boldsymbol{P}_k^{(-)} \tag{5.7c}$$

where $\boldsymbol{P_{f}}_k$ is the co-variance matrix, $\boldsymbol{R_{f}}_k$ is the measurement noise matrix and $\boldsymbol{Q_{f}}_k$ is the discrete process noise matrix given as follows:

$$\boldsymbol{Q_{f}}_k = \int^{T_s} \oplus(\tau)E[\boldsymbol{\mathcal{W}\mathcal{W}}^T]\boldsymbol{\Phi}(\tau)d\tau = \begin{bmatrix} \frac{T_s^5}{20} & \frac{T_s^4}{8} & \frac{T_s^3}{6} \\ \frac{T_s^4}{8} & \frac{T_s^3}{3} & \frac{T_s^2}{2} \\ \frac{T_s^3}{6} & \frac{T_s^2}{3} & T_s \end{bmatrix} \otimes diag(\phi_s) \tag{5.8}$$

where ϕ_s is the spectral density of the white process noise and it is given by:

$$\phi_s = \frac{1}{t_F}\begin{bmatrix} n_{T_{max}}^2 & n_{T_{max}}^2 & n_{T_{max}}^2 \end{bmatrix} \tag{5.9}$$

where $n_{T_{max}}$ is the maximum manoeuvre level of the target the missile can counter (based on the 3 to 1 rule of thumb $n_{T_{max}} = 200m/s^2$) and t_F was assumed to be equal to the cruise duration before self-destruct ($t_F = 8s$). Measurement noise matrix is given by the expectation value of the measurement noise vector and it is equivalent to a diagonal matrix of the variance of each noise source:

$$\boldsymbol{R_{f}}_k = E[\mathcal{V}\mathcal{V}^T] = \boldsymbol{\sigma}^2 \tag{5.10}$$

$$\boldsymbol{\sigma} = diag\left\{ \begin{bmatrix} \sigma_x & \sigma_y & \sigma_z & \sigma_{vx} & \sigma_{vy} & \sigma_{vz} \end{bmatrix} \right\} \tag{5.11}$$

5.4 Engagement With Target Filtering

This section presents the results for target engagement in the presence of seeker measurement noise. The nine-state Kalman filter described above is used to estimate the closing velocity, range and target acceleration. The radar noise model and the target acceleration model are presented in the Table 5.2. Only the range-dependent noise model is considered in the current simulation. A spectral density of the white noise process of 625 m^2/s^5 was used in the Kalman filter.

Table 5.2: Noise parameters

	Symbols	Value
Closing velocity	$\sigma_{R_{TM}}$	$1.73 \times 10^{-6} \|R_{TM}\|^2$
Closing Range	$\sigma_{V_{TM}}$	$1.73 \times 10^{-6} \|V_{TM}\|^2$

The initial co-variance matrix for the nine-state Kalman filter was:

$$P_0 = diag([10, 10, 10, 200, 200, 200, 2000, 2000, 2000])$$

The initial values of the target are selected such that they are in the order of the expected target kinematics and noise variance. The estimates of the measured states of the target by Kalman filter are presented in Figures 5.10 to 5.12. It is clear from these figures that the Kalman filter yields acceptable estimation of the closing velocity and the closing in range. The deviation of the measurement from the true values decrease as the missile approaches the target because the noise levels are range dependent.

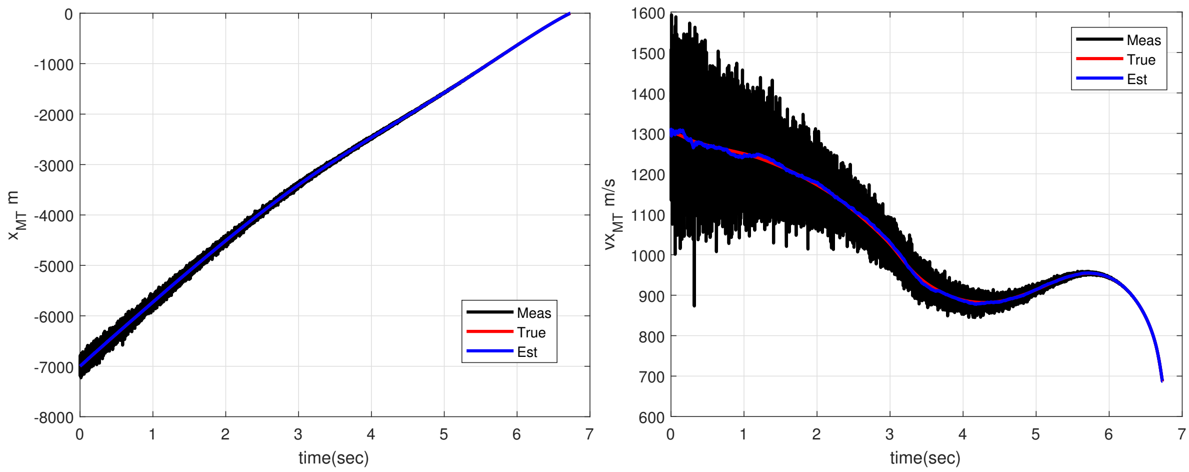

(a) Estimated closing distance.

(b) Estimate closing velocity.

Figure 5.10: Estimated and measured x-axis target-missile closing kinematics.

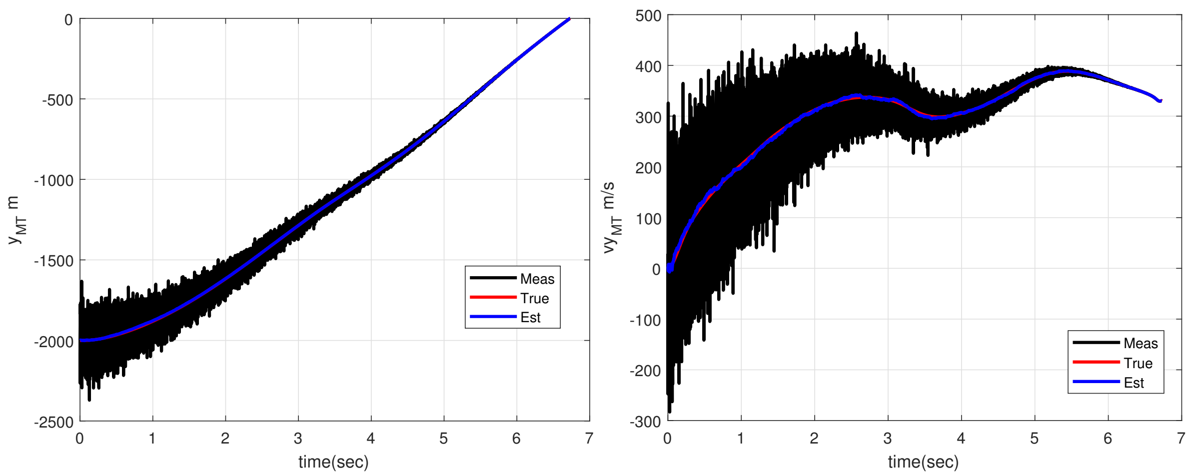

(a) Estimated closing distance.

(b) Estimated closing velocity.

Figure 5.11: Estimated and measured y-axis target-missile closing kinematics.

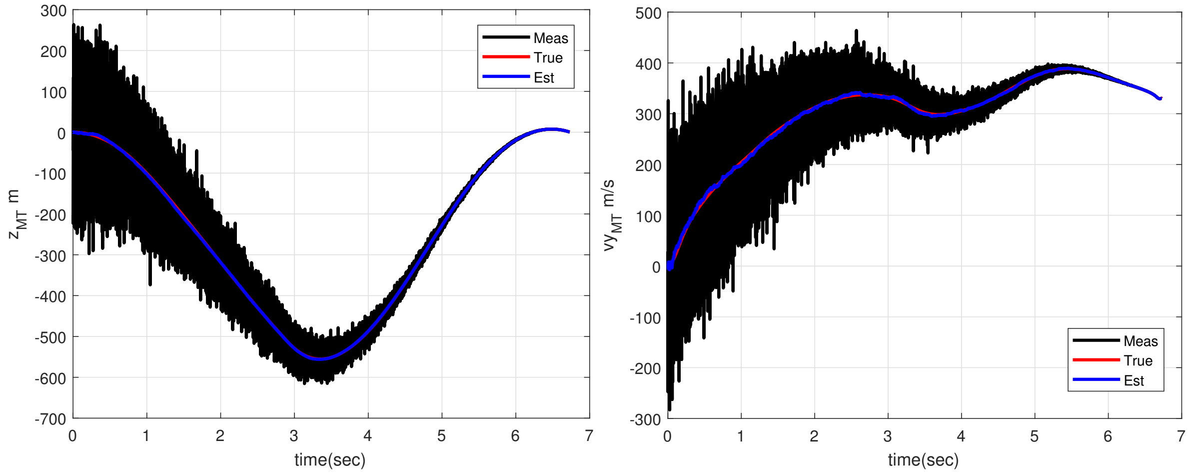

(a) Estimated closing distance.

(b) Estimated closing velocity.

Figure 5.12: Estimated and measured z-axis target-missile closing kinematics.

Figures 5.13a, b and 5.14a and b illustrate the estimated target acceleration and error dynamics of the estimation. It is clear that the filter does estimate the target acceleration to within three sigma of the nominal value. The lateral acceleration estimate spike at 3.5 s is a result of step change in the normal acceleration. Furthermore, both the estimate and the error diverge as the missile gets closer to the target. This phenomenon is attributed to the fact that the guidance law diverges as the closing distance approaches zero.

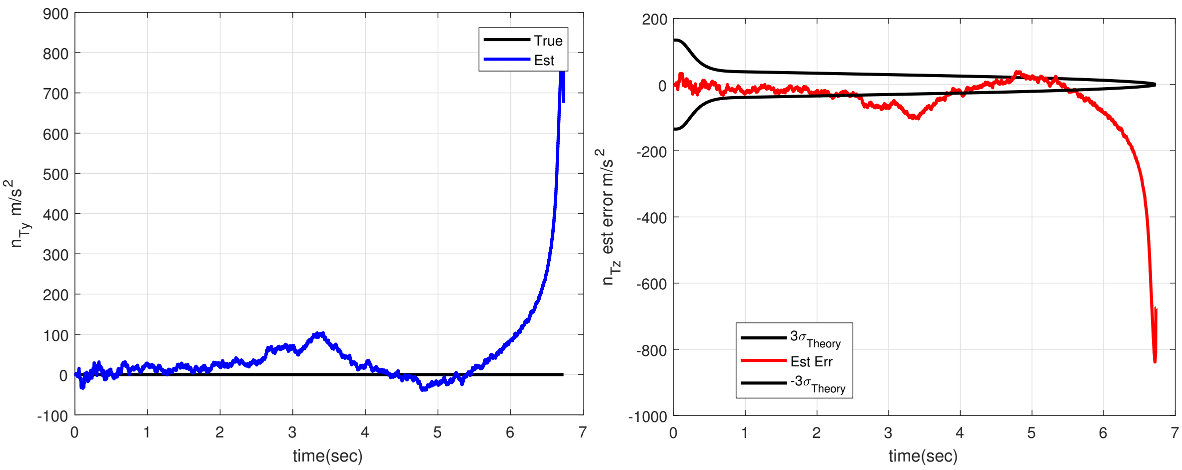

(a) Estimated lateral load factor

(b) Lateral load factor estimation error

Figure 5.13: Estimated lateral load factor and resulting estimation deviations.

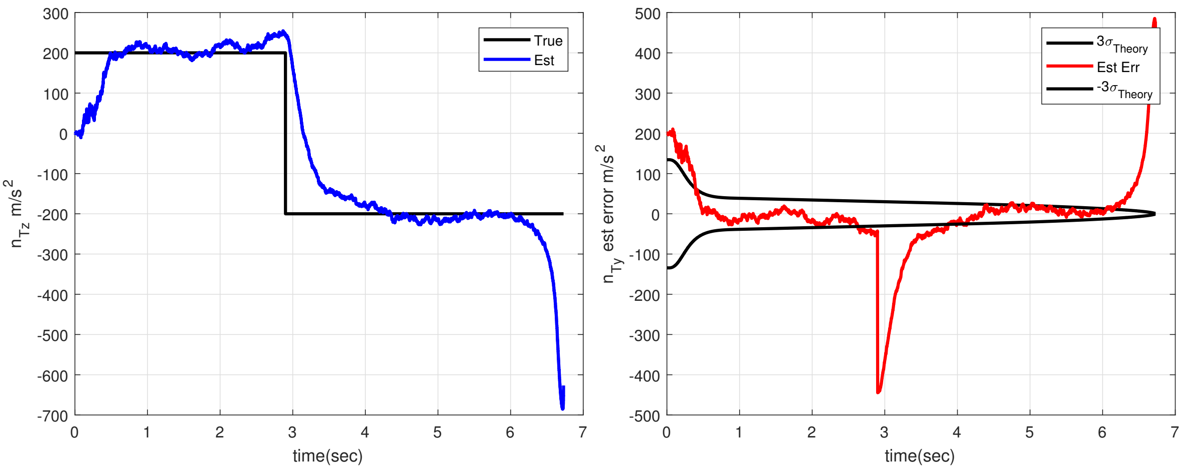

(a) Estimated normal load factor (b) Normal load factor estimation error

Figure 5.14: Estimated normal load factor and resulting estimation deviations.

It is clear from the plot that the estimation error is within three sigma bounds except at points where there are dynamic variations in target acceleration or where the guidance law diverges (see Figs. 5.13 and 5.14). The theoretical standard deviation of the target acceleration are determined by taking the square root of the corresponding diagonal entry of the co-variance matrix P_k.

Figures 5.15a and 5.15b illustrate the acceleration responses of the missile during target engagement. The acceleration commands, although sufficient to guide the missile to the target, they are not smooth signals clearly indicating transmission of some measurement noise throughout the control system. The acceleration command diverges at the target-missile rendezvous point because the acceleration command is inversely proportional to the closing-in range.

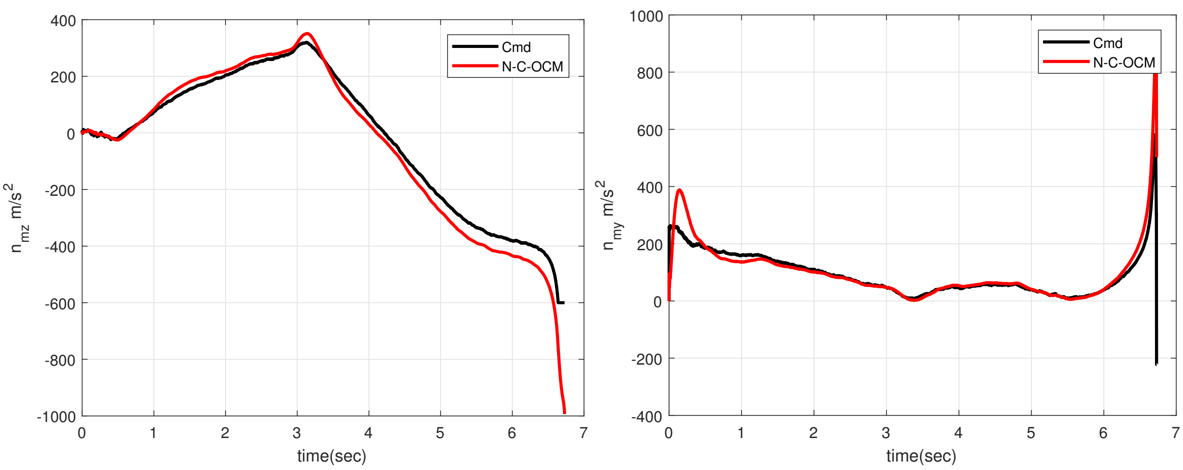

Figure 5.15: Missile normal and lateral acceleration commands from the guidance law.

Kinematic responses of a DAC missile with and without tracking filter in the guidance loop are presented in the figures 5.16, 5.17 and 5.18 for different autopilots. Pure proportional navigation guidance law was used for the target engagement scenario without a tracking filter. The baseline autopilot and the OCM autopilot in the case of unfiltered target state result in the DAC missile failing to meet the 2 m miss distance requirement. In fact, the missile without tracking filter results in a miss of order 10^2 m. An overall observation from the engagement kinematics is that a combination of augmented proportional navigation and tracking filter improves the dynamics of the missile and the chance of the missile achieving the desired end-game miss distance.

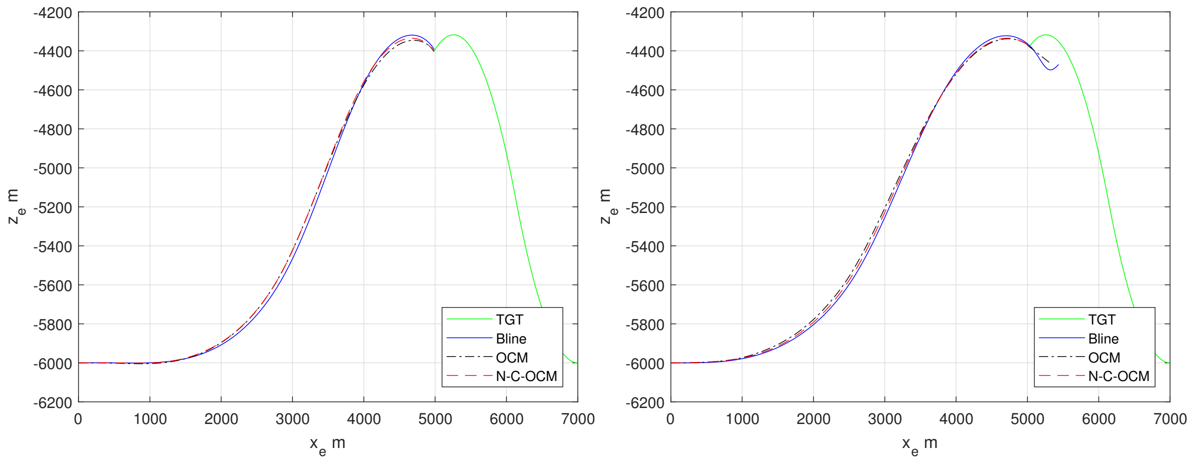

(a) Homing with Kalman filter. (b) Homing without Kalman filter.

Figure 5.16: xz-plane kinematics for different homing scenarios.

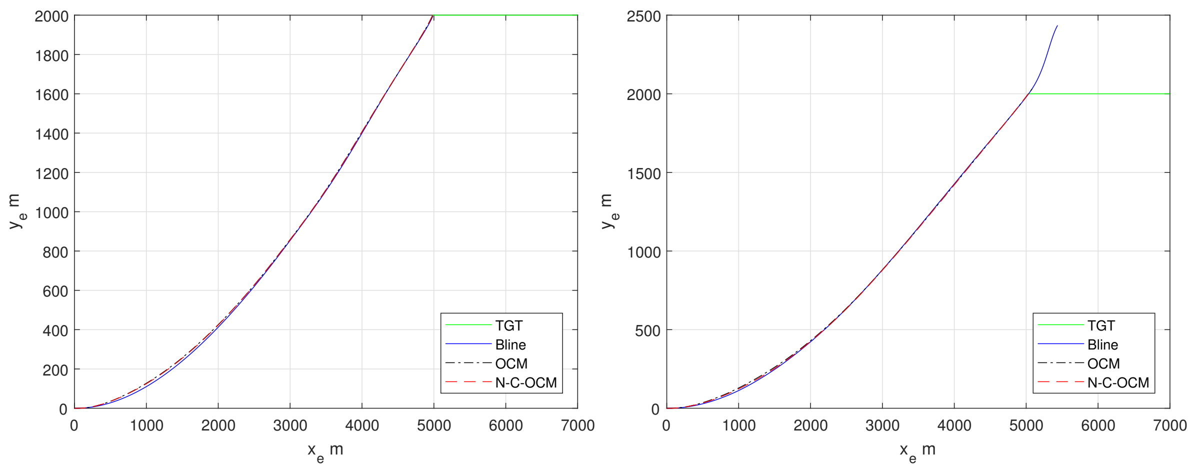

(a) Homing with Kalman filter. (b) Homing without Kalman filter.

Figure 5.17: xy-plane kinematics for different homing scenarios.

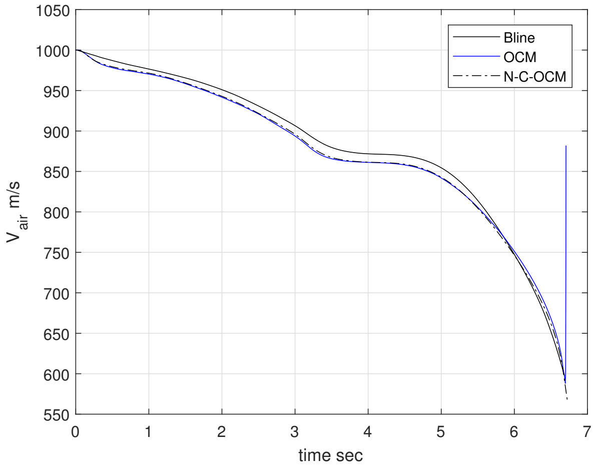

(a) Homing with Kalman filter.

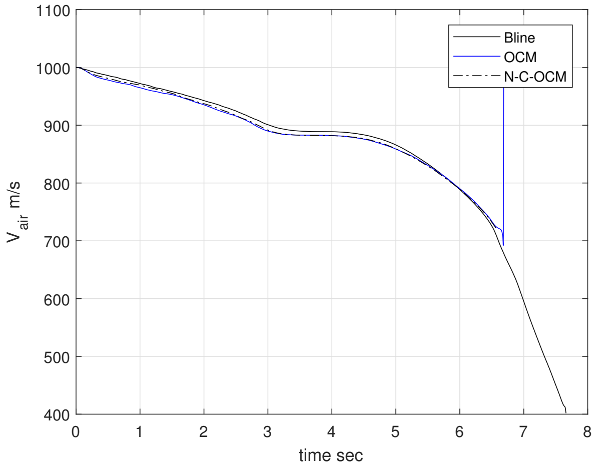

(b) Homing without Kalman filter.

Figure 5.18: Airspeed variations for different homing scenarios.

Chapter 6

Homing Performance Analysis

6.1 Introduction

Homing performance analysis of a missile is one of the most critical steps in the missile design process that influences the missions and the manner in which the system is deployed in the field. The end goal of the analysis is an envelope that shows the operator the performance bounds of the missile in terms of range and target engagement capabilities. The performance envelope is primarily limited by tracking capability of the guidance system, sensors and the kinematics of the missile. Within the performance envelope the missile is required to travel from the launch point to the intercept point and on arrival it must have enough energy to reduce the final miss distance to ensure a high kill rate (Zarchan, 2012).

In the case of an air-to-air or air-to-surface missile the performance envelope is presented as a launch acceptable region (LAR) which is made up of launch point that results in the missile rendezvousing the target at the specified intercept conditions. For a given missile design the resulting LAR is influenced mainly by the launch altitude, launch speed, and target speed. The performance envelope in the case of a surface-to-air missile is presented as an action volume. Action volume defines the volume in region in which the missile is capable of eliminating an incoming threat. The action volume is a result of the fact that surface-to-air missile are used to defend a point against incoming threats from multiple directions (Fleeman, 2006).

This chapter presents an action envelope of the DAC missile with an adaptive autopilot. Due to the fact that only the terminal performance are under consideration, only the relative action envelope that results during the terminal phase will be presented for the DAC and tail-only missile. Canard-controlled missile was excluded because the current aerodynamic model has no provision for roll authority in the case of canard control.

6.2 Performance Envelope Synthesis

The envelopes presented were generated for three different target manoeuvres: a constant speed target, a weaving target and a constant manoeuvre target. A weaving target tries to dissipate the energy of the missile before reaching the intercept point by having it track a continuously varying closing velocity and position. A constant manoeuvre target attempts to evade the missile by flying out of the kill zone with the highest acceleration possible. Table 6.1 illustrates the initial velocity and acceleration of each target manoeuvre:

Table 6.1: Types of target manoeuvres considered.

Manoeuvre	Value (m/s^2)	Initial Velocity (m/s)	Initial altitude (m)
Constant	100	100	6000
Weaving	200	300	6000
None	0	300	6000

Table 6.2 illustrates the initial conditions of the DAC missile. As previously noted only the terminal performance is analysed in this study. For each simulation point the missile starts from the origin at the given altitude with a heading of zero. Due to the fact that for each simulation a different intercept point is conceived the possible heading error between the missile and the target is between -90 and 90 deg.

Table 6.2: Missile initial cruise conditions.

Initial State	Values	units
Velocity	900	m/s
Angle-of-attack	0	rad
Altitude	6000	m

Only the incoming performance envelope is presented because a surface-to-air missile defends a point on the ground. The missile is always launched and positioned by the mid-course guidance such that the terminal phase starts of as a head-on engagement with some initial heading error.

6.3 Performance Envelope Results

Kinematic performance of a DAC missile and tail-controlled missile with baseline and adaptive controller are presented here. Normalised OCM update rule with co-variance adjustment was used as the adaptive controller for both missile configurations. Figures 6.1 to 6.3 illustrate variation of final miss distance with initial missile-to-target range from when the missile rocket motor burns-out for the two controller configurations. Figure 6.1 presents the miss distance variation against a constant speed target, Figure 6.2 presents the miss distance variation against a weaving target and Figure 6.3 shows the miss distance against a constant manoeuvre target.

It is clear from the results that the largest initial missile-to-target range is independent of the control configurations, which is expected since both missiles have the same kinematic and inertial properties. The lowest initial missile-to-target range at which the missile can still counter the target is different for each missile controller, configuration and target engagement scenario. Discrepancy in the lowest acceptable initial missile-to-target range is driven by missile agility. The DAC missile general has better performance in terms of the lowest acceptable initial missile-to-target range mainly because of the superior manoeuvrability. Furthermore, The OCM controller in most of the cases exhibits a better lowest initial missile-to-target range, thus suggesting that it offers better manoeuvre capability than the baseline controller.

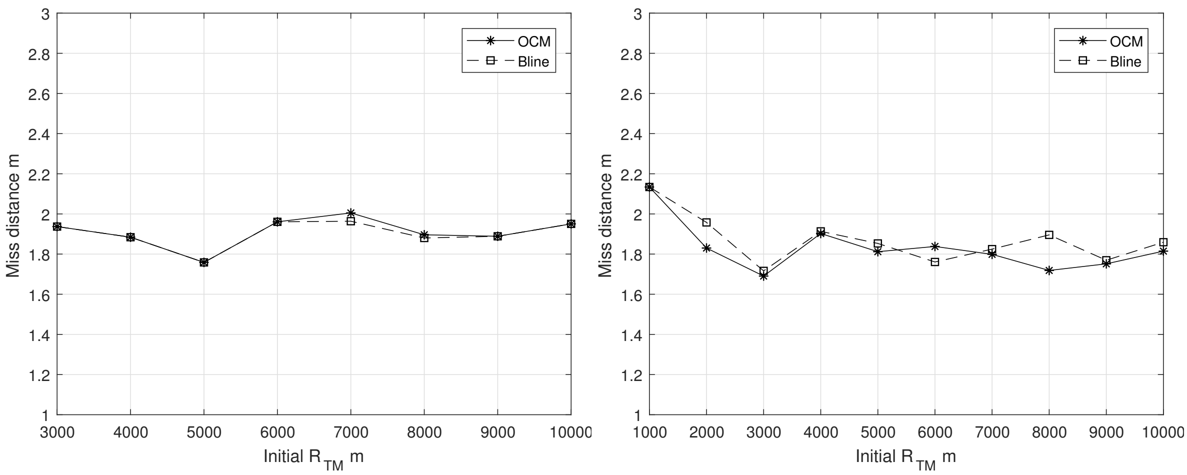

(a) Tail-fin Missile (b) DAC missile

Figure 6.1: Variation in miss distance with initial missile-to-target distance of a DAC and tail-fin missile against a constant speed target.

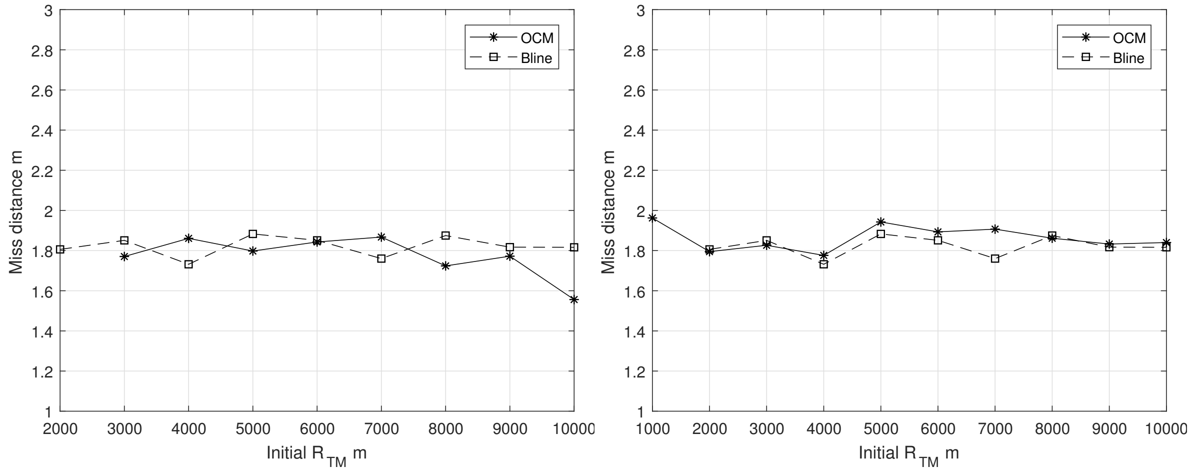

(a) Tail-fin Missile (b) DAC missile

Figure 6.2: Variation in miss distance with initial missile-to-target distance of a DAC and tail-fin missile against a weaving target.

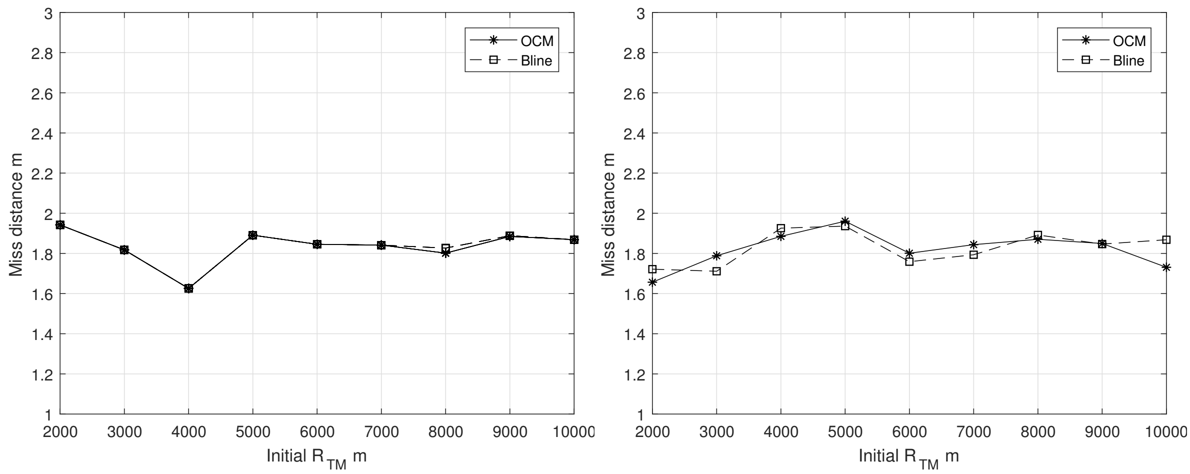

(a) Tail-fin Missile (b) DAC missile

Figure 6.3: Variation in miss distance with initial missile-to-target distance of a DAC and tail-fin missile against a constant manoeuvre target.

Figures 6.4 to 6.9 illustrate the performance envelope of a tail-controlled missile and a dual-controlled missile against a constant speed target, constant manoeuvre target and a weaving target. For each target scenario, a performance envelope was generated for both the baseline autopilot and the OCM autopilot. Only intercept point that resulted in a miss distance of 2.0 m or less were included in the performance envelope for both missile configurations. The overall observation from the results is that both dual and tail-only missile have an equal maximum range indicating that even though the dual-controlled missile has a high wet surface area due to the presence of canards, the overall drag does not penalise the DAC missile range in the terminal phase.

Figures 6.4 and 6.5 illustrate constant speed target performance envelope of the tail-only and dual-controlled missiles. The constant speed scenario represents an ideal engagement where missile trajectory corrections are done only at the beginning of a terminal phase flight and the missile flies to a predetermined intercept point. The constant speed target result in the largest performance envelope of the three scenarios, this is due to the little trajectory corrections during the flight thus the missile has more kinetic energy to reach farther rendezvous points.

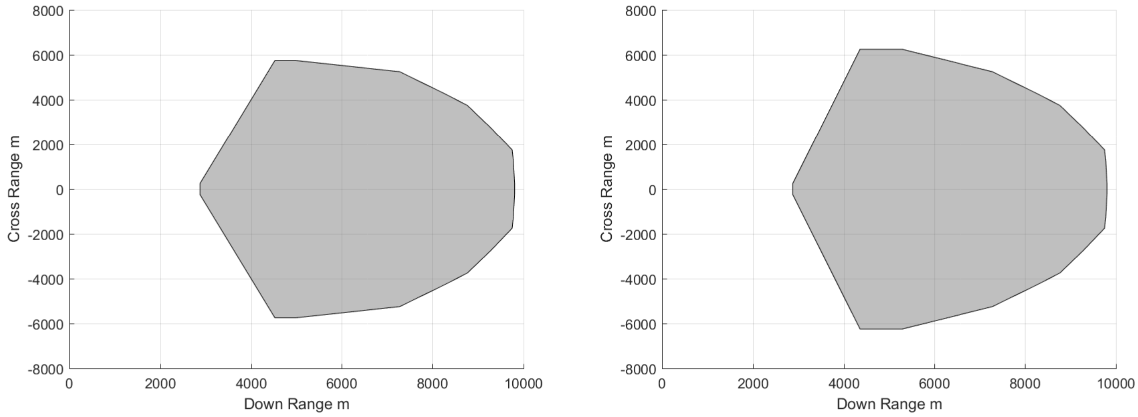

(a) Baseline Autopilot

(b) Adaptive OCM autopilot

Figure 6.4: Tail-fin only missile cruise performance envelope against a constant speed target.

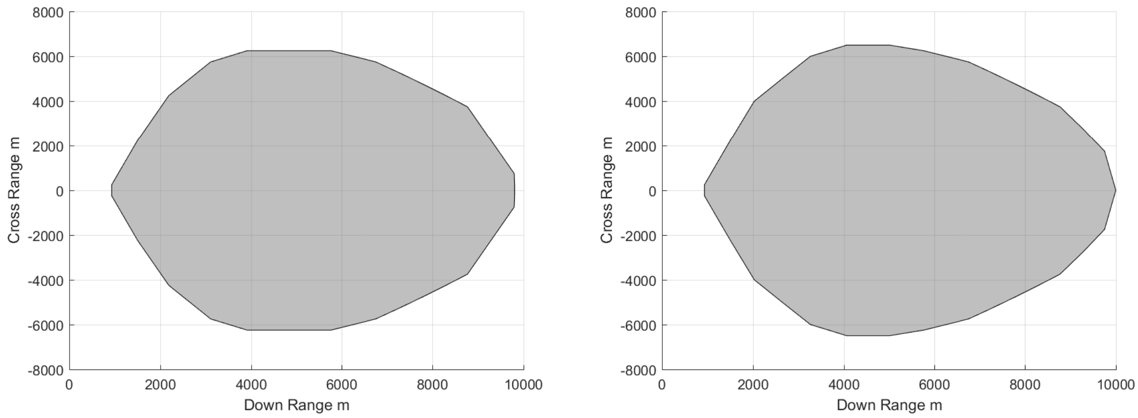

(a) Baseline Autopilot

(b) Adaptive OCM autopilot

Figure 6.5: DAC missile cruise performance envelope against a constant speed target.

The performance envelope against a weaving target of the tail-only and dual-controlled missile are presented in Figures 6.6 and 6.7. It is clear from figure 6.6 that the envelope of the tail-fin only missile reduces significantly for the weaving target when compared with the same configuration against a constant speed target. The reduction in envelope can be attributed to fast dissipation of kinematic energy by tracking an oscillating intercept point and the cost associated with overcoming the undershoot due to the minimum phase phenomenon. The envelope of the DAC missile against a weaving target remains relatively unchanged when compared with the constant speed envelope.

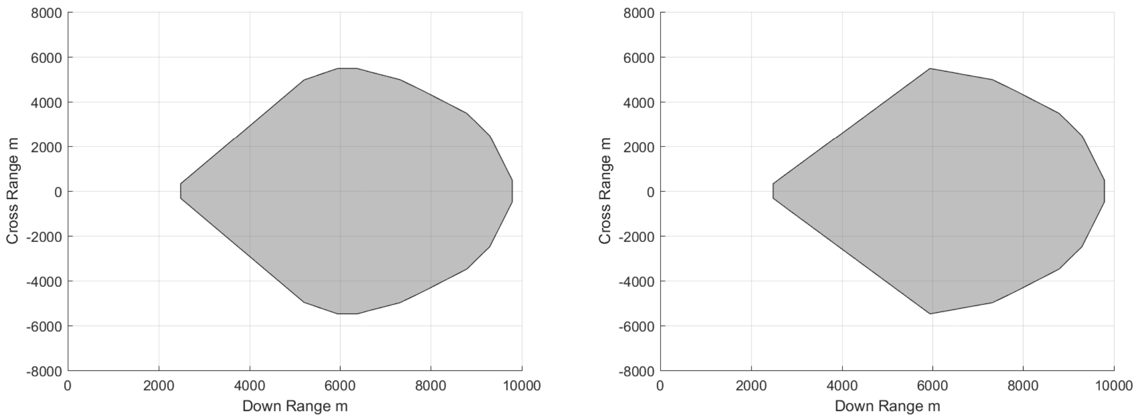

(a) Baseline Autopilot (b) Adaptive OCM autopilot

Figure 6.6: Tail-fin only missile cruise performance envelope against a weaving target.

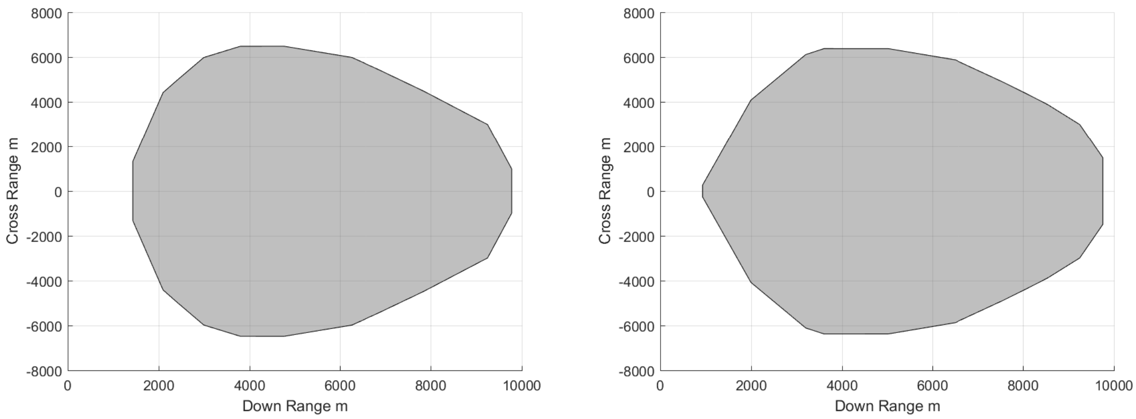

(a) Baseline Autopilot (b) Adaptive OCM autopilot

Figure 6.7: DAC missile cruise performance envelope against a weaving target.

Figures 6.8 and 6.9 depict the cruise performance envelope of the tail-fin and DAC missile against a constant manoeuvre target. It is clear that engaging a manoeuvring target results in a smaller performance envelope. Furthermore, there is little discrepancy between the baseline envelope and the adaptive control envelope for both tail-fin-only and dual controlled missile. The resulting envelope suggest that a constant manoeuvre has the highest survival chance. This follows because the missile is in a continuous state of pull-up manoeuvre which results in high angles-of-attack and high drag thus penalising the maximum cruise performance range.

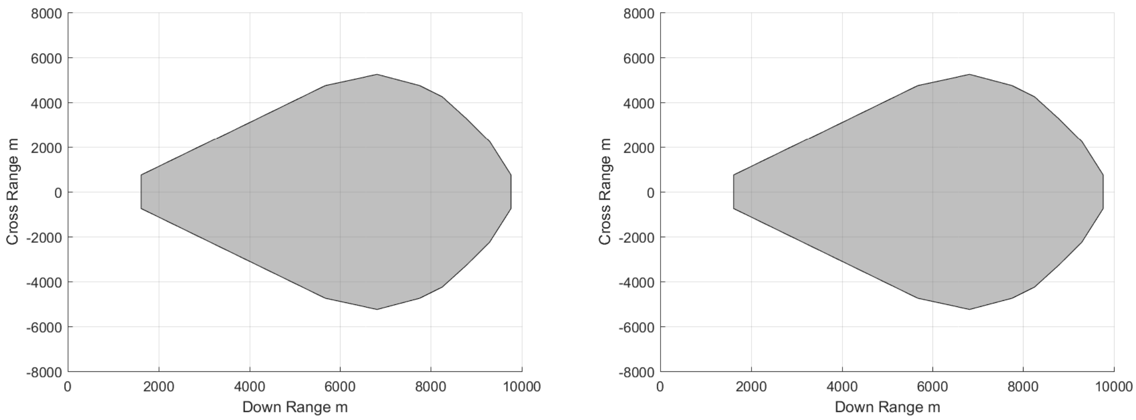

(a) Baseline Autopilot (b) Adaptive OCM autopilot

Figure 6.8: Tail-fin only missile cruise performance envelope against a constant manoeuvre target.

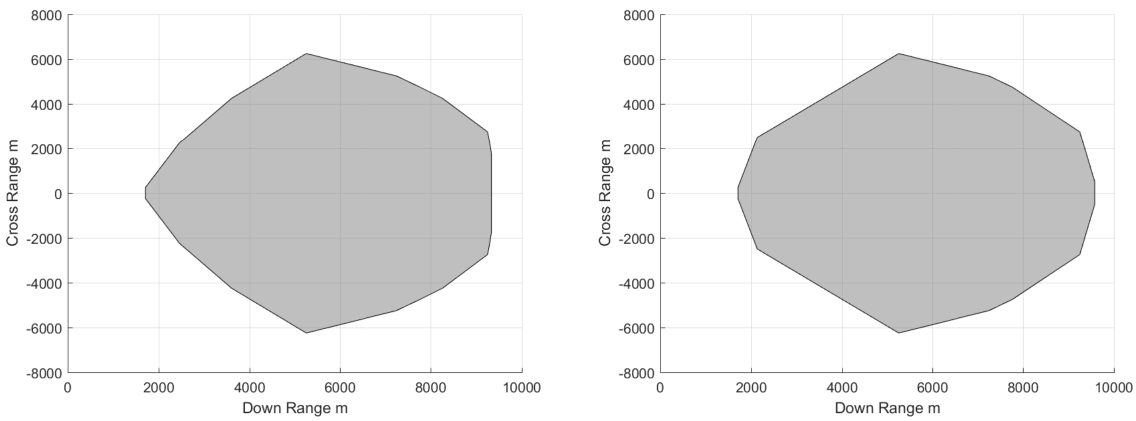

(a) Baseline Autopilot (b) Adaptive OCM autopilot

Figure 6.9: DAC missile cruise performance envelope against a constant manoevre target.

Chapter 7

Conclusions and Recommendations

In this study, an adaptive controller with model reference adaptive control topology was investigated for a dual aerodynamically-controlled missile. A nonlinear model of a dual-controlled missile was developed and a trim map was generated. Due to the two actuator inputs the trim equation of the dual-controlled missile is indeterminate and to obtain a unique trim condition for a given speed; the angle-of-attack and canard deflection were fixed while the tail-fin deflection was unconstrained. The trim map was used to design a benchmark gain-scheduled three-loop autopilot. A two time-scale separation dynamic inversion controller was designed and used as the baseline controller for the proposed MRAC controller. The following adaptive rules were investigated on the DAC missile MRAC controller: $\sigma-$modification, $\epsilon-$modification, adaptive loop recovery and optimal control modification. Adaptive loop recovery and optimal control modification update rule exhibited better performance in terms of uncertainty compensation, transient response and actuator deflection magnitudes necessary to track a given acceleration command. A novel normalised optimal control modification update rule with co-variance adjustment was proposed. A stability proof based on Lyapunov theory is presented to prove the uniformly ultimately bounded stability condition of the proposed update rule. The rule aims to eliminate the effects of basis-function amplitudes on the adaptive gain and the co-variance adjustment prevents the possibility of persistent learning by adjusting initially set high adaptive gains to lower values with time. The normalised optimal control modification with co-variance adjustment did not penalise controller performance when compared to the standard optimal control modification controller. Kinematic performance of the missile was investigated and the results were presented as a performance envelope. Missile kinematic performance were evaluated with both baseline controller and normalised optimal control modification with co-variance adjustment. It was observed that the missile with adaptive controller was highly manoeuvrable and was capable of countering very close targets and yielded the largest performance envelope for engagement against constant-speed, weaving and constant-manoeuvre target.

7.1 Recommendations and Future Work

It is recommended that future works focus on applying the adaptive controller on an expanded aerodynamic model that includes lower flight speed and high sideslip angles. Furthermore, full state feedback is an ideal assumption since the philosophy in missile design is to have as few sensors as possible, therefore it is recommended that a state estimator for the DAC missile be designed and implemented with the adaptive controller to evaluate controller performance in a more practical setting. A high-fidelity servo model for both tail-fins and canards is recommended to ensure that the adaptive controller still has acceptable stability margins when integrated with a realistic actuator. The performance envelope presented in this study is limited to the terminal phase, it is recommended that with the availability of a full-range aerodynamic model a more detailed action volume be regenerated with the current controller configuration to obtain a high confidence performance envelope.

Bibliography

P. Apkarian, J.-M. Biannic, and P. Gahinet. Self-scheduled h-infinity control of missile via linear matrix inequalities. *Journal of Guidance, Control, and Dynamics*, 18(3):532–538, 1995.

I. Astrov, A. Pedai, and E. Rustern. Simulation of two-rate adaptive hybrid control with neural and neuro-fuzzy networks for stochastic model of missile autopilot. In *Intelligent Control and Automation, 2004. WCICA 2004. Fifth World Congress on*, volume 3, pages 2603–2607. IEEE, 2004.

A. T. Azar and F. E. Serrano. Adaptive sliding mode control of the furuta pendulum. In *Advances and applications in sliding mode control systems*, pages 1–42. Springer, 2015.

S. Balakrishnan, A. Tsourdos, and B. A. White. *Advances in missile guidance, control, and estimation*. CRC Press, New York, USA, 2012.

I. Barkana. Simple adaptive control–a stable direct model reference adaptive control methodology–brief survey. *International Journal of Adaptive Control and Signal Processing*, 28(7-8):567–603, 2014.

J. H. Blakelock. *Automatic control of aircraft and missiles*. John Wiley & Sons, New York, USA, 1991.

A. Calise, T. Yucelen, J. Muse, and B.-J. Yang. A loop recovery method for adaptive control. In *AIAA Guidance, Navigation, and Control Conference Chicago, Illinois*, pages 5967–5979, 2009.

A. J. Calise and R. T. Rysdyk. Nonlinear adaptive flight control using neural networks. *IEEE Control Systems Magazine*, 18(6):14–25, 1998.

A. J. Calise and T. Yucelen. Adaptive loop transfer recovery. *Journal of Guidance, Control, and Dynamics*, 35(3):807–815, 2012.

A. J. Calise, M. Sharma, and J. E. Corban. Adaptive autopilot design for guided munitions. *Journal of Guidance, Control, and Dynamics*, 23(5):837–843, 2000.

A. J. Calise, N. Hovakimyan, and M. Idan. Adaptive output feedback control of nonlinear systems using neural networks. *Automatica*, 37(8):1201–1211, 2001.

C. Cao and N. Hovakimyan. Design and analysis of a novel l_1 adaptive controller, part i: Control signal and asymptotic stability. In *American Control Conference Minneapolis, MN, USA*, pages 3397–3402, 2006.

C. Cao and N. Hovakimyan. Guaranteed transient performance with l_1 adaptive controller for systems with unknown time-varying parameters and bounded disturbances: Part i. In *American Control Conference*, pages 3925–3930, New York, USA, 2007a.

C. Cao and N. Hovakimyan. Novel l_1 neural network adaptive control architecture with guaranteed transient performance. *IEEE Transactions on Neural Networks*, 18(4):1160–1171, 2007b.

V. C. Chen, F. Li, S.-S. Ho, and H. Wechsler. Micro-doppler effect in radar: phenomenon, model, and simulation study. *IEEE Transactions on Aerospace and Electronic Systems*, 42(1): 2–21, 2006.

T. Cimen. State-dependent riccati equation (SDRE) control: A survey. *IFAC Proceedings Volumes, Seoul, Korea*, 41(2):3761–3775, 2008.

T. Cimen. Survey of state-dependent Riccati equation in nonlinear optimal feedback control synthesis. *Journal of Guidance, Control, and Dynamics*, 35(4):1025–1047, 2012.

T. ÇImen and S. P. Banks. Nonlinear optimal tracking control with application to supertankers for autopilot design. *Automatica*, 40(11):1845–1863, 2004.

Y. Elhalwagy and M. Tarbouchi. Fuzzy logic sliding mode control for command guidance law design. *ISA transactions*, 43(2):231–242, 2004.

G. Feng. A survey on analysis and design of model-based fuzzy control systems. *IEEE Transactions on Fuzzy systems*, 14(5):676–697, 2006.

E. L. Fleeman. *Tactical missile design*. American Institute of Aeronautics and Astronautics, Reston, USA, 2006.

H. Goldstein, C. P. Poole, and J. L. Safko. *Classical Mechanics*. Addison-Wesley, San Francisco, USA, 3rd edition, 2001.

S. Gutman. Superiority of canards in homing missiles. *IEEE Transactions on Aerospace and Electronic Systems*, 39(3):740–746, 2003.

N. Hovakimyan and C. Cao. *L1 adaptive control theory: guaranteed robustness with fast adaptation*, volume 21. SIAM-Society for Industrial and Applied Mathematics, Philadelphia, USA, 2010.

N. Hovakimyan, F. Nardi, A. Calise, and N. Kim. Adaptive output feedback control of uncertain nonlinear systems using single-hidden-layer neural networks. *IEEE Transactions on Neural Networks*, 13(6):1420–1431, 2002.

Y.-J. Huang, T.-C. Kuo, and S.-H. Chang. Adaptive sliding-mode control for nonlinear systems with uncertain parameters. *IEEE Transactions On Systems, Man And Cybernetics Part B Cybernetics"*, 38(2):534, 2008.

K. J. Hunt, D. Sbarbaro, R. Żbikowski, and P. J. Gawthrop. Neural networks for control systems: A survey. *Automatica*, 28(6):1083–1112, 1992.

F. Ibarrondo. *Optimization of the Integrated Guidance and Control for a Dual Aerodynamic Control Missile*. PhD thesis, Aeronauticos, Polytechnic University of Madrid, 2015.

F. Ibarrondo and P. Sanz-Aránguez. Integrated versus two-loop guidance-autopilot for a dual control missile with high-order aerodynamic model. *Proceedings of the Institution of Mechanical Engineers, Part G: Journal of Aerospace Engineering*, 230(1):60–76, 2016.

P. A. Ioannou and P. V. Kokotovic. Instability analysis and improvement of robustness of adaptive control. *Automatica*, 20(5):583–594, 1984.

P. B. Jackson. Overview of missile flight control systems. *Johns Hopkins APL Technical Digest*, 29(1):9–24, 2010.

P. Kantue. Design and flight testing of a gain-scheduled autopilot based on reduced model constraints. In *Control Conference Africa, Johannesburg, RSA*, pages 187–192, 2017.

H. K. Khalil. *Noninear Systems*. Prentice-Hall, New Jersey, USA, 1996.

B. S. Kim and A. J. Calise. Nonlinear flight control using neural networks. *Journal of Guidance, Control, and Dynamics*, 20(1):26–33, 1997.

K. Kim, T. Yucelen, and A. Calise. K-modification in adaptive control. In *AIAA Infotech@ Aerospace*, pages 3321–3335. 2010.

S. Kim, D. Cho, and H. J. Kim. Force and moment blending control for fast response of agile dual missiles. *IEEE Transactions on Aerospace and Electronic Systems*, 52(2):938–947, 2016.

C.-C. Lee. Fuzzy logic in control systems: Fuzzy logic controller. i. *IEEE Transactions on Systems, Man, and cybernetics*, 20(2):404–418, 1990.

C.-H. Lee, B.-E. Jun, and J.-I. Lee. Connections between linear and nonlinear missile autopilots via three-loop topology. *Journal of Guidance, Control, and Dynamics*, 39(6):1426–1432, 2016.

M. Levy, T. Shima, and S. Gutman. Linear quadratic integrated versus separated autopilot-guidance design. *Journal of Guidance, Control, and Dynamics*, 36(6):1722–1730, 2013.

H.-X. Li and S. Tong. A hybrid adaptive fuzzy control for a class of nonlinear MIMO systems. *IEEE Transactions on Fuzzy Systems*, 11(1):24–34, 2003.

K.-S. Li, X.-F. Liu, and Z.-Z. Shi. Review of research status and development direction of dieless drawing. *Metallurgical Research & Technology*, 113(6):610–622, 2016.

S. Liu, X. Qu, and Y. Liu. Design of missile autopilot based on fuzzy control. In *Information and Automation (ICIA), 2016 IEEE International Conference on*, pages 1339–1343, Ningbo, China, 2016. IEEE.

X. Liu, Y. Wu, Y. Deng, and S. Xiao. A global sliding mode controller for missile electromechanical actuator servo system. *Proceedings of the Institution of Mechanical Engineers, Part G: Journal of Aerospace Engineering*, 228(7):1095–1104, 2014.

H. J. Marquez. *Nonlinear Control Systems: Analysis and Design*. John Wiley and Sons, Inc, Hoboken, New Jersey, 2003.

R. Matuvsuu, R. Prokop, and L. Pekavr. Parametric and unstructured approach to uncertainty modelling and robust stability analysis. *International Journal of Mathematical Models and Methods in Applied Sciences*, 5(6):1011–1018, 2011.

M. McFarland and A. Calise. Multilayer neural networks and adaptive nonlinear control of agile anti-air missiles. In *Guidance, Navigation, and Control Conference*, pages 401–410, New Orleans, LA, U.S.A., 1997.

M. B. McFarland and A. J. Calise. Neural networks and adaptive nonlinear control of agile anti-air missiles. *Journal of Guidance, Control, and Dynamics*, 23(3):547–553, 2000.

P. Menon and E. Ohlmeyer. Integrated design of agile missile guidance and autopilot systems. *Control Engineering Practice*, 9(10):1095–1106, 2001.

S. Mobayen. Fast terminal sliding mode controller design for nonlinear second-order systems with time-varying uncertainties. *Complexity*, 21(2):239–244, 2015.

C. Mracek and D. Ridgely. Missile longitudinal autopilots: connections between optimal control and classical topologies. In *AIAA guidance, Navigation, and Control Conference and Exhibit*, pages 6381–6410, San Francisco, California, 2005.

C. Mracek and D. Ridgely. Optimal control solution for dual (tail and canard) controlled missiles. In *AIAA Guidance, Navigation, and Control Conference and Exhibit*, pages 6569–6591, Keystone, Colorado, 2006.

C. P. Mracek. *Tactical Missile Autopilots*, pages 1459–1465. Springer London, 2015.

K. Narendra and A. Annaswamy. A new adaptive law for robust adaptation without persistent excitation. *IEEE Transactions on Automatic Control*, 32(2):134–145, 1987.

N. Nguyen. *Model Reference Adaptive Control - A Primer*. Springer International Publishing, New york, 2018.

N. Nguyen, J. Burken, and C. Hanson. Optimal control modification adaptive law with covariance adaptive gain adjustment and normalization. In *AIAA Guidance, Navigation, and Control Conference*, pages 6606–6624, Portland, Oregon, USA, 2011.

N. Nguyen, C. Hanson, J. Burken, and J. Schaefer. Normalized optimal control modification and flight experiments on NASA F/A-18 aircraft. *Journal of Guidance, Control, and Dynamics*, 40(4):1061–1075, 2017.

N. T. Nguyen. Robust optimal adaptive control method with large adaptive gain. In *AIAA Infotech@ Aerospace Conference and AIAA Unmanned Unlimited Conference*, pages 1802–1822, St. Louis, MO, USA, 2009.

N. T. Nguyen. Optimal control modification for robust adaptive control with large adaptive gain. *Systems & Control Letters*, 61(4):485–494, 2012.

N. T. Nguyen, K. Krishnakumar, and J. Boskovic. An optimal control modification to model-reference adaptive control for fast adaptation. In *AIAA Guidance, Navigation and Control Conference and Exhibit*, pages 7283–7301, Honolulu, Hawaii, 2008.

R. Padhi, N. Unnikrishnan, and S. Balakrishnan. Model-following neuro-adaptive control design for non-square, non-affine nonlinear systems. *IET Control Theory & Applications*, 1 (6):1650–1661, 2007.

N. F. Palumbo, R. A. Blauwkamp, and J. M. Lloyd. Modern homing missile guidance theory and techniques. *Johns Hopkins APL technical digest*, 29(1):42–59, 2010.

J. O. Pedro, A. Panday, and L. Dala. A nonlinear dynamic inversion-based neurocontroller for unmanned combat aerial vehicles during aerial refuelling. *International Journal of Applied Mathematics and Computer Science*, 23(1):75–90, 2013.

F. Plestan, Y. Shtessel, V. Bregeault, and A. Poznyak. New methodologies for adaptive sliding mode control. *International Journal of Control*, 83(9):1907–1919, 2010.

K. Rajagopal, A. Mannava, S. Balakrishnan, N. Nguyen, and K. Krishnakumar. Neuroadaptive model following controller design for non-affine and non-square aircraft systems. In *AIAA Guidance, Navigation, and Control Conference*, pages 5737–5758, Chicago, Illinois, USA, 2009.

D. Ridgely, Y. Lee, and T. Fanciullo. Dual aero/propulsive missile control-optimal control and control allocation. In *AIAA Guidance, Navigation, and Control Conference and Exhibit*, pages 6570–6591, Keystone, Colorado, 2006.

C. Rohrs, L. Valavani, M. Athans, and G. Stein. Robustness of continuous-time adaptive control algorithms in the presence of unmodeled dynamics. *IEEE Transactions on Automatic Control*, 30(9):881–889, 1985.

J.-H. Ryu, C.-S. Park, M.-J. Tahk, J.-H. Ryu, C.-S. Park, and M.-J. Tahk. Plant inversion control of tail-controlled missiles. In *Guidance, Navigation, and Control Conference*, pages 1691–1696, New Orleans, LA, U.S.A, 1997.

B. Sampath, K. Perera, W. Wijesuriya, and V. Dassanayake. Fuzzy based stabilizer control system for quad-rotor. *International Journal of Mechanical, Aerospace, Industrial and Mechatronics Engineering*, 8(2):455–461, 2014.

J.-J. E. Slotine and W. Li. On the adaptive control of robot manipulators. *The international journal of robotics research*, 6(3):49–59, 1987.

A. S. Snell, D. F. Enns, and W. L. Arrard. Nonlinear inversion flight control for a supermaneuverable aircraft. *Journal of Guidance, Control, and Dynamics*, 15(4):976–984, 1992.

M. G. Snyder. Nonlinear stabilization and control of medium range surface to air interceptor missiles. Master's thesis, University of Central Florida Orlando, Florida, 2009.

N. Sundararajan, P. Saratchandran, and Y. Li. *Fully tuned radial basis function neural networks for flight control*, volume 12. Springer Science & Business Media, New York, USA, 2003.

R. Vepa. *Nonlinear Control of Robots and Unmanned Aerial Vehicles: An Integrated Approach*. CRC Press, New York, USA, 2016.

T. Vialar. *Handbook of Mathematics*. BoD-Books on Demand, Norderstedt, Germany, 2015.

D. E. Williams, B. Friedland, and A. N. Madiwale. Modern control theory for design of autopilots for bank-to-turn missiles. *Journal of Guidance, Control, and Dynamics*, 10(4): 378–386, 1987.

M. Xin, S. Balakrishnan, D. T. Stansbery, and E. J. Ohlmeyer. Nonlinear missile autopilot design with $\theta - D$ technique. *Journal of Guidance, Control, and Dynamics*, 27(3):406–417, 2004.

H. Yu, T. Xie, S. Paszczynski, and B. M. Wilamowski. Advantages of radial basis function networks for dynamic system design. *IEEE Transactions on Industrial Electronics*, 58(12): 5438–5450, 2011.

T. Yucelen. *Advances in adaptive control theory: Gradient-and derivative-free approaches*. PhD thesis, School of Aerospace Engineering, Georgia Institute of Technology, 2012.

T. Yucelen and A. J. Calise. Robustness of a derivative-free adaptive control law. *Journal of Guidance, Control, and Dynamics*, 37(5):1583–1599, 2014.

T. Yucelen and W. M. Haddad. Low-frequency learning and fast adaptation in model reference adaptive control. *IEEE Transactions on Automatic Control*, 58(4):1080–1085, 2013.

P. Zarchan. *Tactical and strategic missile guidance*. American Institute of Aeronautics and Astronautics, Reston, USA, 5th edition, 2012.

P. H. Zipfel. *Modeling and simulation of aerospace vehicle dynamics*. American Institute of Aeronautics and Astronautics, Blacksburg , Virginia, 2007.

Appendix A

Aero Model Coefficients

Table A.1: Normal and Side force aerodynamic coefficients for equation 2.19

Normal Force Coefficient	Value	Side Force Coefficient	Value
C_{N_α}	0.2020	C_{S_β}	0.2020
$C_{N_{\alpha\|\alpha\|}}$	0.0111	$C_{S_{\beta\|\beta\|}}$	0.0111
$C_{N_{\alpha^3}}$	$-1.131 \cdot 10^{-5}$	$C_{S_{\beta^3}}$	$-1.131 \cdot 10^{-5}$
$C_{N_{\alpha\beta^2}}$	$2.73782 \cdot 10^{-4}$	$C_{S_{\alpha^2\|\beta\|}}$	$2.73782 \cdot 10^{-4}$
$C_{N_{\delta_q^c}}$	$6.554 \cdot 10^{-2}$	$C_{S_{\delta_q^c}}$	$-6.554 \cdot 10^{-2}$
$C_{N_{\alpha\delta_q^c}}$	$-8.846 \cdot 10^{-4}$	$C_{S_{\beta\delta_q^c}}$	$8.846 \cdot 10^{-4}$
$C_{N_{\beta^2\delta_q^c}}$	$2.74617 \cdot 10^{-4}$	$C_{S_{\alpha^2\delta_q^c}}$	$-2.74617 \cdot 10^{-4}$
$C_{N_{\delta_q^t}}$	$6.961 \cdot 10^{-2}$	$C_{S_{\delta_q^t}}$	$-6.961 \cdot 10^{-2}$
$C_{N_{\beta^2\delta_q^t}}$	$2.746 \cdot 10^{-4}$	$C_{S_{\beta\delta_q^t}}$	$-4.066 \cdot 10^{-4}$
$C_{N_{\delta_q^t\delta_q^c}}$	$-4.040 \cdot 10^{-4}$	$C_{S_{\delta_q^t\delta_q^c}}$	$4.040 \cdot 10^{-4}$
C_{N_q}	$5.734 \cdot 10^{-1}$	C_{S_r}	$5.734 \cdot 10^{-1}$
$C_{N_{\dot\alpha}}$	$-2.781 \cdot 10^{-2}$	$C_{S_{\dot\beta}}$	$-2.781 \cdot 10^{-2}$

The pitching moment due to canard effect $C_{m_{\delta_q^t}}$ is given as follows:

$$C_{m_{\delta_q^c}}(\alpha) = \begin{cases} \displaystyle\sum_{k=1}^{n_1} C^k_{m_{\alpha\delta_q^c}} e^{-\left(\frac{\alpha-\alpha^k_{\delta_q^c}}{\Delta\alpha^k_{\delta_q^c}}\right)^2} & \alpha \geq 0 \\ \displaystyle\sum_{k=1}^{n_1} 2C^k_{m_{\alpha\delta_q^c}} e^{-\left(\frac{\alpha-\alpha^k_{\delta_q^c}}{\Delta\alpha^k_{\delta_q^c}}\right)^2} - C^k_{m_{\alpha\delta_q^c}} e^{-\left(\frac{|\alpha|-\alpha^k_{\delta_q^c}}{\Delta\alpha^k_{\delta_q^c}}\right)^2} & \alpha < 0 \end{cases} \tag{A.1}$$

The pitching moment due to tail effect $C_{m_{\delta_q^t}}$ is given as follow:

$$C_{m_{\delta_q^t}(\alpha)} = \begin{cases} C^0_{m_{\alpha\delta_q^t}} + \sum_{k=1}^{n_2} C^k_{m_{\alpha\delta_q^t}} (\alpha)^k & \alpha \geq 0 \\ 2C^0_{m_{\alpha\delta_q^t}} - \sum_{k=1}^{n_2} C^k_{m_{\alpha\delta_q^t}} (|\alpha|)^k & \alpha < 0 \end{cases} \tag{A.2}$$

The yawing moment due to canard effect $C_{n_{\delta_r^c}(\beta)}$ is given as follow:

$$C_{n_{\delta_r^c}(\beta)} = \begin{cases} \sum_{k=1}^{n_1} C^k_{n_{\beta\delta_r^c}} e^{-\left(\frac{\beta-\beta^k_{\delta_r^c}}{\Delta\beta^k_{\delta_r^c}}\right)^2} & \beta \geq 0 \\ \sum_{k=1}^{n_1} 2C^k_{n_{\beta\delta_r^c}} e^{-\left(\frac{\beta-\beta^k_{\delta_r^c}}{\Delta\beta^k_{\delta_r^c}}\right)^2} - C^k_{n_{\beta\delta_r^c}} e^{-\left(\frac{|\beta|-\beta^k_{\delta_r^c}}{\Delta\beta^k_{\delta_r^c}}\right)^2} & \beta < 0 \end{cases} \tag{A.3}$$

The yawing moment due to yaw effect $C_{n_{\delta_r^t}(\beta)}$ is given as follow:

$$C_{n_{\delta_r^t}(\beta)} = \begin{cases} C^0_{n_{\beta\delta_r^t}} + \sum_{k=1}^{n_2} C^k_{n_{\beta\delta_r^t}} (\beta)^k & \beta \geq 0 \\ 2C^0_{n_{\beta\delta_r^t}} - \sum_{k=1}^{n_2} C^k_{n_{\beta\delta_r^t}} (|\beta|)^k & \beta < 0 \end{cases} \tag{A.4}$$

Table A.2: Pitching and yawing moment aerodynamic coefficients for equations 2.20.

Pitch Moment Coefficients	Value	Yaw Moment Coefficients	Value
C_{m_α}	0.1373	C_{n_β}	-0.1373
$C_{m_{\alpha\|\alpha\|}}$	$-1.020 \cdot 10^{-2}$	$C_{n_{\beta\|\beta\|}}$	$1.020 \cdot 10^{-2}$
$C_{m_{\alpha^3}}$	$-6.864 \cdot 10^{-5}$	$C_{n_{\beta^3}}$	$6.864 \cdot 10^{-5}$
$C_{m_{\alpha\beta^2}}$	$-4.676 \cdot 10^{-4}$	$C_{n_{\alpha^2\beta}}$	$4.676 \cdot 10^{-4}$
$C_{m_{\beta^2\delta_q^c}}$	$-1.148 \cdot 10^{-3}$		$-1.148 \cdot 10^{-3}$
$C_{m_{\beta^2\delta_q^t}}$	$-1.148 \cdot 10^{-3}$		$-1.148 \cdot 10^{-3}$
$C^1_{m_{\alpha\delta_q^c}}$	$1.112 \cdot 10^{-1}$	$C^1_{n_{\beta\delta_q^c}}$	$1.112 \cdot 10^{-1}$
$C^2_{m_{\alpha\delta_q^c}}$	$1.067 \cdot 10^{-1}$	$C^2_{n_{\beta\delta_q^c}}$	$1.067 \cdot 10^{-1}$
$C^3_{m_{\alpha\delta_q^c}}$	$7.037 \cdot 10^{-1}$	$C^3_{n_{\beta\delta_q^c}}$	$7.037 \cdot 10^{-1}$
$\alpha^1_{\delta_q^c}$	1.852	$\beta^1_{\delta_q^c}$	1.852
$\alpha^2_{\delta_q^c}$	-2.463	$\beta^2_{\delta_q^c}$	-2.463
$\alpha^3_{\delta_q^c}$	321.2	$\beta^3_{\delta_q^c}$	321.2
$C_{m_{\delta_q^c\delta_q^t}}$	$2.800 \cdot 10^{-3}$	$C_{n_{\delta_q^t\delta_q^c}}$	$2.800 \cdot 10^{-3}$
$\Delta\alpha^1_{\delta_q^c}$	2.754	$\Delta\beta^1_{\delta_q^c}$	2.754
$\Delta\alpha^2_{\delta_q^c}$	10.740	$\Delta\beta^2_{\delta_q^c}$	10.740
$\Delta\alpha^3_{\delta_q^c}$	330.7	$\Delta\beta^3_{\delta_q^c}$	330.7
$C^0_{m_{\alpha\delta_q^t}}$	$-5.014 \cdot 10^{-1}$	$C^0_{n_{\beta\delta_q^t}}$	$-5.014 \cdot 10^{-1}$
$C^1_{m_{\alpha\delta_q^t}}$	$3.520 \cdot 10^{-3}$	$C^1_{n_{\beta\delta_q^t}}$	$3.520 \cdot 10^{-3}$
$C^2_{m_{\alpha\delta_q^t}}$	$1.384 \cdot 10^{-4}$	$C^2_{n_{\beta\delta_q^t}}$	$1.384 \cdot 10^{-4}$
$C^3_{m_{\alpha\delta_q^t}}$	$-1.705 \cdot 10^{-5}$	$C^3_{n_{\beta\delta_q^t}}$	$-1.705 \cdot 10^{-5}$
$C^3_{m_{\alpha\delta_q^t}}$	$1.916 \cdot 10^{-7}$	$C^4_{n_{\beta\delta_q^t}}$	$1.916 \cdot 10^{-7}$
$C_{m_{\beta^2\delta_q^c}}$	$-1.148 \cdot 10^{-3}$	$C_{n_{\alpha^2\delta_q^c}}$	$-1.148 \cdot 10^{-3}$
$C_{m_{\beta^2\delta_q^t}}$	$-1.148 \cdot 10^{-3}$	$C_{n_{\alpha^2\delta_q^t}}$	$-1.148 \cdot 10^{-3}$
C_{m_q}	-18.560	C_{m_r}	-18.560
$C_{m_{\dot\alpha}}$	-1.405	$C_{m_{\dot\beta}}$	1.405

Induced rolling moment due to wind angles C_{l_i} is given as follow:

$$\begin{aligned} C_{l_i}(\alpha,\beta) &= \sin(4\phi_a)(C_{l_{i01}}\beta^2 + C_{l_{i21}}\alpha^2 + C_{l_{i41}}\alpha^4 + C_{l_{i61}}\alpha^6) \\ &+ \sin(8\phi_a)(C_{l_{i02}}\beta^2 + C_{l_{i22}}\alpha^2 + C_{l_{i42}}\alpha^4 + C_{l_{i62}}\alpha^6) \end{aligned} \tag{A.5}$$

Induced rolling moment to canard yaw $C_{l_{\alpha\delta_r^c}}$ is given as follows:

$$C_{l_{\alpha\delta_r^c}}(\alpha) = \sum_{k=1}^{n_4} C_{l_{\alpha\delta_r^c}} \sin(\omega^k_{\alpha\delta_r^c}\alpha + \phi^k_{\alpha\delta_r^c}) \tag{A.6}$$

Induced rolling moment to canard yaw $C_{l_{\alpha\delta_q^c}}$ is given as follows:

$$C_{l_{\beta\delta_q^c}}(\beta) = \sum_{k=1}^{n_4} C_{l_{\beta\delta_q^c}} \sin(\omega^k_{\beta\delta_q^c}\beta + \phi^k_{\beta\delta_q^c}) \tag{A.7}$$

Rolling moment due to roll deflection $C_{l_{\beta\delta_p}}$ is given as follows:

$$C_{l_{\alpha\delta_p}}(\alpha_T) = \sum_{k=1}^{n_6} C_{l_{\alpha_T\delta_p}} e^{\frac{\alpha_T - \Delta\alpha_{\alpha_T\delta_p}}{\Delta\alpha_{\alpha_T\delta_p}}} \tag{A.8}$$

Table A.3: Rolling moment aerodynamic coefficients for equations 2.22.

Roll Moment Coefficients	Value	Roll Moment Coefficients	Value
$C_{l_{i01}}$	$4.074 \cdot 10^{-4}$	$C_{l_{i21}}$	$1.934 \cdot 10^{-4}$
$C_{l_{i41}}$	$-4.948 \cdot 10^{-7}$	$C_{l_{i61}}$	$3.305 \cdot 10^{-10}$
$C_{l_{i02}}$	$1.697 \cdot 10^{-4}$	$C_{l_{i22}}$	$6.984 \cdot 10^{-5}$
$C_{l_{i42}}$	$-3.296 \cdot 10^{-7}$	$C_{l_{i62}}$	$4.303 \cdot 10^{-10}$
$C^1_{l_{\alpha\delta_r^c}}$	$4.868 \cdot 10^{-2}$	$C^2_{l_{\alpha\delta_r^c}}$	$1.933 \cdot 10^{-2}$
$C^3_{l_{\alpha\delta_r^c}}$	$9.041 \cdot 10^{-3}$	$C^4_{l_{\alpha\delta_r^c}}$	$4.599 \cdot 10^{-3}$
$C^5_{l_{\alpha\delta_r^c}}$	$2.854 \cdot 10^{-3}$	$C^6_{l_{\alpha\delta_r^c}}$	$2.799 \cdot 10^{-3}$
$C^7_{l_{\alpha\delta_r^c}}$	$1.895 \cdot 10^{-3}$	$\omega^1_{l_{\alpha\delta_r^c}}$	$7.826 \cdot 10^{-2}$
$\omega^2_{l_{\alpha\delta_r^c}}$	$1.587 \cdot 10^{-1}$	$\omega^3_{l_{\alpha\delta_r^c}}$	$3.141 \cdot 10^{-1}$
$\omega^4_{l_{\alpha\delta_r^c}}$	$4.712 \cdot 10^{-1}$	$\omega^5_{l_{\alpha\delta_r^c}}$	$7.855 \cdot 10^{-1}$
$\omega^6_{l_{\alpha\delta_r^c}}$	$6.283 \cdot 10^{-1}$	$\omega^7_{l_{\alpha\delta_r^c}}$	$9.425 \cdot 10^{-1}$
$\phi^1_{l_{\alpha\delta_r^c}}$	2.647	$\phi^2_{l_{\alpha\delta_r^c}}$	-1.970
$\phi^3_{l_{\alpha\delta_r^c}}$	-2.654	$\phi^4_{l_{\alpha\delta_r^c}}$	$2.436 \cdot 10^{-1}$
$\phi^5_{l_{\alpha\delta_r^c}}$	-2.433	$\phi^6_{l_{\alpha\delta_r^c}}$	2.315
$\phi^7_{l_{\alpha\delta_r^c}}$	-1.071	$C^1_{l_{\beta\delta_q^c}}$	$4.868 \cdot 10^{-2}$
$C^2_{l_{\beta\delta_q^c}}$	$1.933 \cdot 10^{-2}$	$C^3_{l_{\beta\delta_q^c}}$	$9.041 \cdot 10^{-3}$
$C^4_{l_{\beta\delta_q^c}}$	$4.599 \cdot 10^{-3}$	$C^5_{l_{\beta\delta_q^c}}$	$2.854 \cdot 10^{-3}$
$C^6_{l_{\beta\delta_q^c}}$	$2.799 \cdot 10^{-3}$	$C^7_{l_{\beta\delta_q^c}}$	$1.895 \cdot 10^{-3}$
$\omega^1_{l_{\beta\delta_q^c}}$	$7.826 \cdot 10^{-2}$	$\omega^2_{l_{\beta\delta_q^c}}$	$1.587 \cdot 10^{-1}$
$\omega^3_{l_{\beta\delta_q^c}}$	$3.141 \cdot 10^{-1}$	$\omega^4_{l_{\beta\delta_q^c}}$	$4.712 \cdot 10^{-1}$
$\omega^5_{l_{\beta\delta_q^c}}$	$7.855 \cdot 10^{-1}$	$\omega^6_{l_{\beta\delta_q^c}}$	$6.283 \cdot 10^{-1}$
$\omega^7_{l_{\beta\delta_q^c}}$	$9.425 \cdot 10^{-1}$	$\phi^1_{l_{\beta\delta_q^c}}$	2.647
$\phi^2_{l_{\beta\delta_q^c}}$	-1.970	$\phi^3_{l_{\beta\delta_q^c}}$	-2.654
$\phi^4_{l_{\beta\delta_q^c}}$	$2.436 \cdot 10^{-1}$	$\phi^5_{l_{\beta\delta_q^c}}$	-2.433
$\phi^6_{l_{\beta\delta_q^c}}$	2.315	$\phi^7_{l_{\beta\delta_q^c}}$	-1.071
$C^1_{l_{\alpha T\delta_p}}$	$5.441 \cdot 10^{-2}$	$C^2_{l_{\alpha T\delta_p}}$	$1.215 \cdot 10^{-1}$
$C^3_{l_{\alpha T\delta_p}}$	-56.8	$\alpha^2_{l_{T\delta_p}}$	2.317
$\alpha^3_{l_{T\delta_p}}$	20.18	$\Delta\alpha^1_{T\delta_p}$	29.08
$\Delta\alpha^2_{T\delta_p}$	77.93	$\Delta\alpha^3_{T\delta_p}$	5.328
C_{l_p}	-1.935		

Table A.4: Drag force aerodynamic coefficients for equations 2.21.

Drag Force Coefficient	Value	Drag Force Coefficient	Value
C_{A_0}	$4.362 \cdot 10^{-1}$	C_{A_α}	$3.886 \cdot 10^{-3}$
C_{A_β}	$3.886 \cdot 10^{-3}$	$C_{A_{\alpha^2}}$	$-7.642 \cdot 10^{-4}$
$C_{A_{\alpha^3}}$	$2.111 \cdot 10^{-6}$	ΔC_{A_b}	$1.0612 \cdot 10^{-1}$
$C_{A_{\delta_q^c}}$	$2.266 \cdot 10^{-2}$	$C_{A_{\alpha\delta_q^c}}$	$1.348 \cdot 10^{-3}$
$C_{A_{\beta\delta_q^c}}$	$1.001 \cdot 10^{-5}$	$C_{A_{\delta_r^c}}$	$2.266 \cdot 10^{-2}$
$C_{A_{\alpha\delta_q^c}}$	$1.001 \cdot 10^{-5}$	$C_{A_{\beta\delta_r^c}}$	$1.348 \cdot 10^{-3}$
$C_{A_{\delta_p}}$	$2.720 \cdot 10^{-2}$	$C_{A_{\delta_q^t}}$	$-2.282 \cdot 10^{-2}$
$C_{A_{\alpha\delta_q^t}}$	$1.904 \cdot 10^{-3}$	$C_{A_{\alpha^2\delta_q^t}}$	$-2.708 \cdot 10^{-5}$
$C_{A_{\beta\delta_q^t}}$	$1.011 \cdot 10^{-5}$	$C_{A_{\delta_r^t}}$	$-2.282 \cdot 10^{-2}$
$C_{A_{\alpha\delta_r^t}}$	$1.011 \cdot 10^{-5}$	$C_{A_{\alpha^2\delta_r^t}}$	$-1.001 \cdot 10^{-6}$
$C_{A_{\beta\delta_r^t}}$	$1.904 \cdot 10^{-3}$	$C_{A_{\delta_q^c\delta_q^t}}$	$1.600 \cdot 10^{-3}$
$C_{A_{\alpha\delta_q^c\delta_q^t}}$	$2.227 \cdot 10^{-5}$	$C_{A_{\delta_q^{c2}\delta_q^t}}$	$5.000 \cdot 10^{-5}$
$C_{A_{\delta_q^c\delta_q^{t2}}}$	$-5.000 \cdot 10^{-5}$	$C_{A_{\delta_r^c\delta_r^t}}$	$1.600 \cdot 10^{-3}$
$C_{A_{\beta\delta_r^c\delta_r^t}}$	$2.227 \cdot 10^{-5}$	$C_{A_{\delta_r^{c2}\delta_r^t}}$	$5.000 \cdot 10^{-5}$
$C_{A_{\delta_r^c\delta_r^{t2}}}$	$-5.000 \cdot 10^{-5}$		